
X-ray emission from accreting white dwarfs and X-ray binaries

Ilkham Galiullin



München 2022

X-ray emission from accreting white dwarfs and X-ray binaries

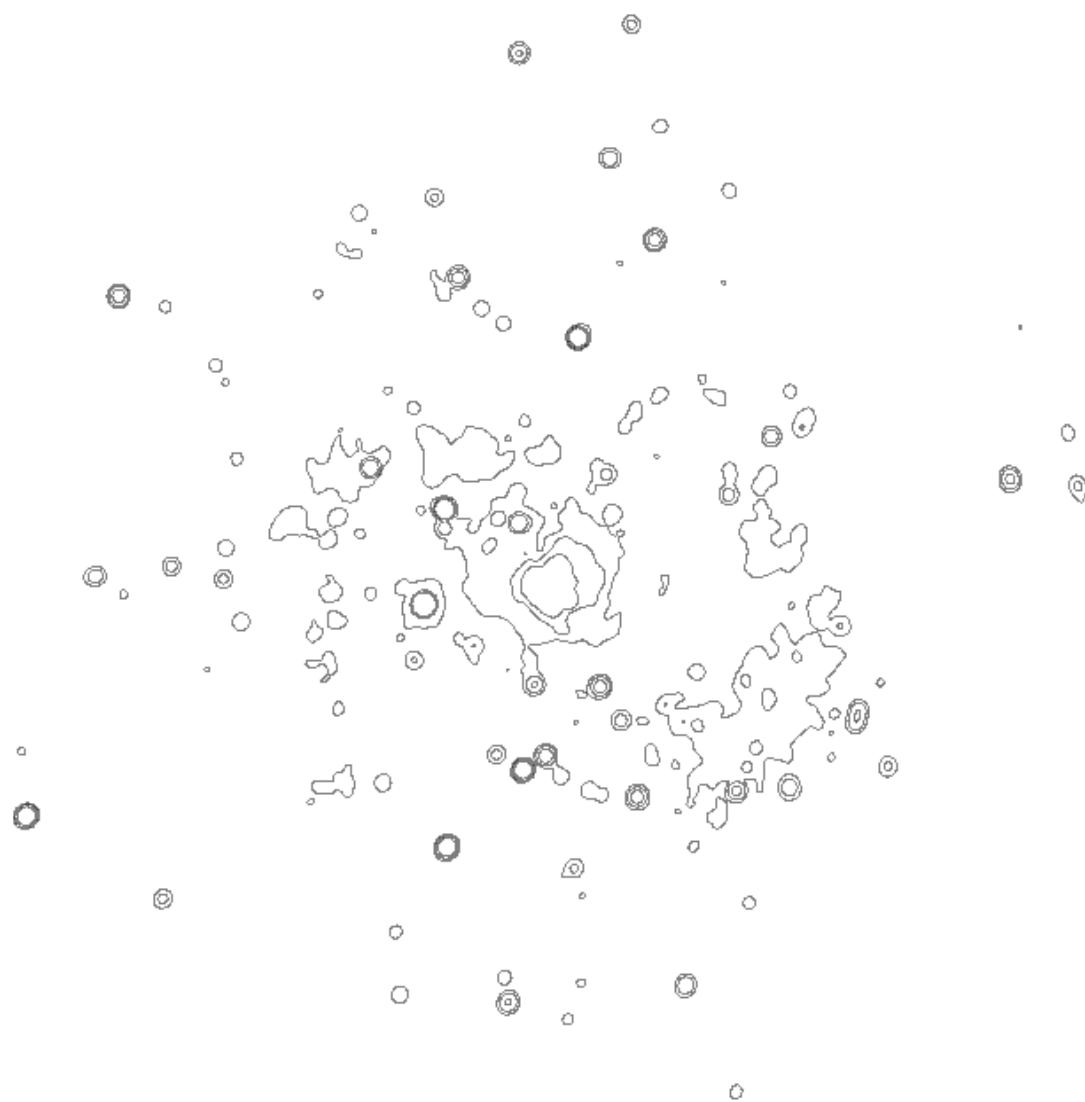
Ilkham Galiullin

Dissertation
der Fakultät für Physik
der Ludwig-Maximilians-Universität
München

vorgelegt von
Ilkham Galiullin
aus Kazan, Russland

München, den 02/06/2022

Erstgutachter: Prof. Dr. Rashid Sunyaev
Zweitgutachter: Prof. Dr. Achim Weiss
Tag der mündlichen Prüfung: 18/07/2022



List of Abbreviations

2MASS	Two Micron All Sky Survey
ACIS	Advanced CCD Imaging Spectrometer
AD	Anderson–Darling
AGN	Active Galactic Nucleus
AIC	Akaike information criterion
BCD	Blue Compact Dwarf Galaxies
BH	Black Hole
CALDB	Chandra Calibration Database
CCD	Charge-Coupled Device
CIAO	Chandra Interactive Analysis of Observations
CN	Classical Nova
CV	Cataclysmic Variable
ECF	Energy Conversion Factor
eROSITA	extended ROentgen Survey with an Imaging Telescope Array
eSASS	eROSITA Science Analysis Software
GAIA	Global Astrometric Interferometer for Astrophysics
H-R	Hertzsprung-Russell
HERACLES	The HERA CO-Line Extragalactic Survey
HMXB	High-Mass X-ray Binaries
HR	Hardness Ratio
IMF	Initial Mass Function
IR	Infrared
IRAS	The Infrared Astronomical Satellite
ISM	Interstellar Medium
LBA	Lyman break analogue

LMXB	Low-Mass X-ray Binaries
NS	Neutron Star
PA	Positional Angle
PSF	Point Spread Function
RC3	Third Reference Catalog of Bright Galaxies
ROSAT	Röntgen Satellite
SED	Spectral Energy Distribution
SFH	Star Formation History
SFR	Star Formation Rate
SN	Supernova
SN Ia	type Ia Supernova
SNR	Supernova Remnant
SRG	Spectrum-Roentgen-Gamma
sSFR	specific Star Formation Rate
SSS	Super-Soft X-ray Source
THINGS	The HI Nearby Galaxy Survey
UV	Ultraviolet
WD	White Dwarf
XMM	The X-ray Multi-Mirror Mission
XSPEC	An X-Ray Spectral Fitting Package

Contents

List of Abbreviations	iv
Zusammenfassung	xv
Summary	xviii
1 Introduction	1
1.1 A synopsis of stellar evolution	1
1.2 X-ray emission from binary system	3
1.2.1 Accretion	3
1.2.2 Nuclear burning on the surface of accreting WDs	6
1.3 Accreting white dwarfs	7
1.3.1 Super-soft X-ray sources	7
1.3.2 Classical Novae phenomena	10
1.3.3 Possible progenitors of type Ia supernovae	12
1.4 X-ray binaries and their connections with properties of host-galaxies	13
1.5 Outline of the thesis	16
2 Populations of super-soft X-ray sources in galaxies of different morphological types	18
2.1 Sample of nearby galaxies	18
2.1.1 Selection criteria	21
2.2 Observations and data reduction	22
2.2.1 Source detection	24
2.2.2 Stellar masses of the final sample of galaxies	25
2.3 Source classification	25
2.3.1 Method	25
2.3.2 Distribution of sources in $HR - \tilde{E}$ plane	27
2.4 Observed properties of soft sources	30
2.4.1 Equivalent hydrogen column density	30
2.4.2 X-ray spectral analysis and $kT_{bb} - L_X$ diagram	32
2.4.3 Foreground stars	35
2.5 Nature of soft and super-soft X-ray sources	35

2.5.1	Super-soft X-ray sources and accreting WDs	35
2.5.2	Specific frequency of super-soft X-ray sources across morphological types	36
2.5.3	Comparison with previous work and discussion	37
2.5.4	Other soft X-ray sources	38
3	X-ray observations of historical classical nova counterparts with eROSITA telescope aboard SRG orbital observatory during the all-sky survey	42
3.1	Sample of Historical Classical Novae in the Galaxy	42
3.2	SRG/eROSITA Telescope Data	43
3.3	X-ray Emission from the Counterparts of CNe in Quiescence	47
3.3.1	Spectral Analysis of Bright Sources	47
3.3.2	Average Spectrum of Faint Sources	48
3.3.3	X-ray Luminosities	49
3.4	Outburst of the Dwarf Nova VY Aqr	50
3.5	Candidates for SSSs among the CN Counterparts	50
3.6	Discussion	53
3.6.1	Nature of the X-ray Emission from CN Counterparts	53
3.6.2	Post-Nova super-soft X-ray Emission	54
3.6.3	Super-soft X-ray Emission from Polars and Their Candidates	55
4	Observed Accretion Rate Distribution of Sources	57
4.0.1	Steady super-soft X-ray Sources	57
4.0.2	CN Counterparts in Quiescence	57
4.0.3	Accretion Rate Distribution of WDs	59
4.0.4	Steady and Non-steady Thermonuclear Hydrogen Burning on the Surface of an Accreting WD	60
5	SRG/eROSITA – IRAS sample of star-forming galaxies: I. Sample construction and L_X – SFR scaling relation	61
5.1	The SRG/eROSITA – IRAS catalog of star-forming galaxies	61
5.1.1	SRG/eROSITA data	61
5.1.2	IRAS source catalogs	62
5.1.3	Cross-matching of SRG/eROSITA and RIFSCz catalogs	62
5.1.4	AGN filtering	62
5.1.5	Physical parameters of galaxies	65
5.2	X-ray emission from star-forming galaxies	68
5.2.1	F_X – F_{FIR} relation: star-formation and nuclear activity	68
5.2.2	Dependence of the X-ray spectrum on F_X/F_{FIR}	69
5.2.3	The scaling relations	71
5.3	Discussion	73
5.3.1	Scaling relations for individual spectral components	73
5.3.2	Comparison with previous studies	74

5.3.3	Metallicity dependence of L_X – SFR scaling relations	74
6	Summary and Conclusion	76
A	Populations of super-soft X-ray sources in galaxies of different morpho- logical types	79
A.1	Galaxy images	79
A.2	Catalog of super-soft X-ray sources	81
B	X-ray observations of historical classical nova counterparts with eROSITA telescope aboard SRG orbital observatory during the all-sky survey	85
	Acknowledgments	100

List of Figures

1.1	An illustration of the H–R diagram and evolutionary track of solar mass star	2
1.2	An artist’s view of a X-ray binary	3
1.3	Roche potential for binary stars	4
1.4	Accretion rate versus WD mass plane	6
1.5	Location of a dozen known SSSs in our and nearby galaxies on H–R diagram	8
1.6	Evolution of the number of SSSs over lookback time	9
1.7	A schematic view of the path of one nova cycle on the H–R diagram	10
1.8	Theoretical light curves for post-nova super-soft X-ray phase for different WD mass	11
1.9	A view of Andromeda Galaxy (M31) at different multi-wavelengths	13
1.10	An example of scaling relation between the total X-ray luminosity of HMXB populations and SFR of host galaxies.	14
1.11	An example of scaling relation between L_X /SFR and gas-phase metallicities of star-forming galaxies.	15
2.1	X-ray sensitivity–distance diagram of nearby galaxies observed by <i>Chandra</i> up to cycle 20.	19
2.2	Relation of the median energy to the temperature of a black-body model and to the photon index of a power-law model	26
2.3	Hardness ratio vs. median energy diagram for compact X-ray sources in the galaxies of our sample.	28
2.3	– <i>continued</i>	29
2.4	Relations between black-body temperature and absorbed X-ray luminosity values computed with different N_H	31
2.5	$kT_{bb} - L_X$ diagram for soft X-ray sources in the galaxies of our sample.	33
2.6	$kT_{bb} - L_X$ for soft X-ray sources in M83 with confirmed supernova remnants	39
2.7	Combined spectra of soft and SSSs in late- and early-type galaxies	40
3.1	Distribution of Galactic CNe by detection years	43
3.2	Distribution of CN counterparts in observed X-ray 0.3–2.3 keV luminosity from the data of the three SRG/eROSITA sky surveys	45
3.3	X-ray spectra of bright sources, where SRG/eROSITA detected more than 50 counts	46

3.4	Combined X-ray spectrum of the sources with fewer than 50 counts.	49
3.5	Black-body temperature distribution of the CN counterparts.	51
3.6	Spectra of potential candidates for super-soft X-ray sources among the CNe sample obtained with SRG/eROSITA.	52
4.1	Observed distribution of CNe in quiescence on the $M_{\text{WD}} - \dot{M}_{\text{acc}}$ plane.	58
5.1	BPT diagram for 149 SRG/eROSITA – IRAS galaxies from the SDSS footprint.	64
5.2	SFR – M_* plane for star-forming galaxies from SRG/eROSITA – IRAS catalog	65
5.3	$F_X - F_{\text{FIR}}$ plot for galaxies with FIR flux available	68
5.4	Combined spectra of galaxies with high and low F_X/F_{IR} ratio.	70
5.5	$L_X - L_{\text{TIR}}$ and L_X –SFR relations	71
5.6	Comparison of the scaling relations for HMXBs and hot gas with other studies.	75
A.1	The 0.3–2 keV band false-color images (smoothed) of galaxies in our sample.	80

List of Tables

2.1	List of nearby galaxies used to study populations of soft and SSSs.	20
2.2	Properties of galaxies and statistics of their X-ray source populations. . .	23
2.3	Absorption column densities for late-type galaxies.	30
5.1	Construction of the SRG/eROSITA – IRAS catalog of normal star-forming galaxies and their candidates.	63
5.2	The different scaling relations for local, star-forming galaxies, observed by SRG/eROSITA.	72
5.3	Model fit results of combined spectrum of 434 galaxies in our sample. . . .	73
A.1	List of <i>Chandra</i> observations used for the analysis.	81
A.2	List of super-soft X-ray sources.	83
B.1	Best fits results of the X-ray spectra of the bright CN counterparts	86
B.2	List of X-ray sources from the SRG/eROSITA catalog having identifications with CNe in our Galaxy.	88

Zusammenfassung

Der Weiße Zwerg in einem Doppelsternsystem akkretiert Material von einem nicht entarteten Spenderstern. Je nach Akkretionsrate und Masse des Weißen Zwerges kann das Kernbrennen der Materie auf der Oberfläche des Weißen Zwerges in stabilen oder instabilen Zuständen ablaufen. In einem stabilen Regime werden klassische stetige superweiche Röntgenquellen beobachtet, die extreme ultraviolette und weiche Röntgenstrahlung ausstrahlen. Instabiles Wasserstoffbrennen auf der Oberfläche von Weißen Zwergen führt zu den Explosionen klassischer und wiederkehrender Novae. Die Nova-Explosion wird hauptsächlich im optischen Bereich beobachtet. Das Kernbrennen des restlichen Wasserstoffs auf der Oberfläche des Weißen Zwerges erzeugt jedoch weiche Röntgenemission, und das System wird als superweiche Röntgenphase nach der Nova beobachtet. In dieser Arbeit untersuchen wir die Röntgenemission von akkretierenden Weißen Zwergen, die ein stabiles oder instabiles thermonukleares Brennen auf ihrer Oberfläche erfahren. Anhand der Stichprobe von akkretierenden Weißen Zwergen schätzen wir die Akkretionsrate dieser Systeme und untersuchen die Grenze zwischen zwei Regimen des thermonuklearen Brennens.

Insbesondere untersuchen wir Populationen weicher und superweicher Röntgenquellen in nahen Galaxien verschiedener morphologischer Typen mit besonderem Schwerpunkt auf der Charakterisierung von Populationen stabiler nuklear brennender, akkretierender Weißer Zwerge. Mit Hilfe des Chandra-Archivs haben wir eine Stichprobe naher Galaxien zusammengestellt, die sich für die Untersuchung von Populationen superweicher Röntgenquellen eignet. Wir verwenden eine Kombination aus Härteverhältnis und mittlerer Energie, um eine Vorauswahl von Röntgenquellen mit weichen Spektren zu treffen, und nutzen das Temperatur und Röntgen-Leuchtkraft Diagramm, um kernbrennende, akkretierende Weiße Zwerge zu identifizieren. Für Spiralgalaxien finden wir eine ausgeprägte und seltene Population superweicher Röntgenquellen, die auf der Röntgen-Leuchtkraft und Temperatur Ebene weitgehend vom Rest der weichen Quellen abgesetzt sind. Die Grenze zwischen diesen Quellen und der viel zahlreicheren Population härterer (aber immer noch weicher) Quellen stimmt mit der Grenze des stabilen Wasserstoffbrennens auf der Oberfläche von Weißen Zwergen überein. Das kombinierte Spektrum der weichen Quellen, die sich außerhalb dieser Grenze befinden, zeigt klare Emissionslinien von Mg und S, die typisch für Supernova-Überreste sind. Die Quellen innerhalb der Grenze des stabilen Kernbrennens haben superweiche Kontinua ohne signifikante Linienemission und sind klare Kandidaten für die akkretierenden kernbrennenden Weißen Zwerge. Die Population der superweichen Röntgenquellen in Spiralgalaxien ist achtmal größer als in linsenförmigen und elliptischen

Galaxien, was weitgehend mit den Berechnungen zur Populationssynthese übereinstimmt. Die geringe spezifische Häufigkeit von superweichen Röntgenquellen, insbesondere in Galaxien des frühen Typs, stützt die frühere Schlussfolgerung, dass sie nicht die Hauptklasse der Supernova-Erzeuger vom Typ Ia sind.

Um akkretierende Weiße Zwerge zu untersuchen, die auf ihrer Oberfläche instabilen Wasserstoff verbrennen, haben wir die Röntgenemission von Wirten historischer klassischer Novae in unserer Galaxie untersucht. Zu diesem Zweck nutzten wir die Daten des eROSITA-Teleskops an Bord des SRG-Orbitalobservatoriums, die wir im Rahmen seiner Durchmusterung des gesamten Himmels erhalten haben. Beim Abgleich der Liste historischer klassischer Novae mit dem SRG/eROSITA-Quellenkatalog haben wir festgestellt, dass die meisten von ihnen kataklysmische Veränderliche in einem ruhigen Zustand sind. Ihre Röntgenemission steht im Zusammenhang mit der Akkretion von Material im Doppelsternsystem und wird hauptsächlich in der Grenzschicht nahe der Oberfläche des Weißen Zwerges und der heißen Korona der Akkretionsscheibe erzeugt. Unter den kataklysmischen Variablen entdecken wir zwei neue weiche Röntgenquellen, die mit der Post-Novae-Phase in Verbindung stehen. Ein überraschend großer Anteil der Quellen zeigt harte Röntgenspektren, was darauf hindeutet, dass diese kataklysmischen Veränderlichen magnetisierte Weiße Zwerge beherbergen könnten. Die Gegenstücke der klassischen Nova stellen eine unverzerrte Stichprobe von akkretierenden Weißen Zwergen mit instabilem Wasserstoffbrennen auf ihrer Oberfläche dar. Um die Grenze zwischen stabilem und instabilem Kernbrennen auf der Oberfläche akkretierender Weißer Zwerge zu erforschen, haben wir Stichprobe stabiler superweicher Röntgenquellen und klassischer Novae in der Ruhephase verwendet. Wir haben die Verteilung der Akkretionsrate von Weißen Zwergen mit instabilem Wasserstoffbrennen anhand der Röntgen-Leuchtkraft von klassischen Novae im Ruhezustand ermittelt. Wir vergleichen sie mit der Akkretionsratenverteilung bekannter stabiler superweicher Röntgenquellen in unserer und in benachbarten Galaxien. Wir finden eine klare Dichotomie zwischen diesen beiden Verteilungen, wobei die klassischen Nova-Quellen ($\dot{M}_{\text{acc}} \approx 10^{-12} - 10^{-8} M_{\odot}/\text{yr}$) und stabile superweiche Röntgenquellen ($\dot{M}_{\text{acc}} \approx 10^{-7.5} - 10^{-6} M_{\odot}/\text{yr}$) besetzen unterschiedliche Bereiche in \dot{M}_{acc} , wie von der Theorie des thermonuklearen Wasserstoffbrennens auf der Oberfläche des Weißen Zwerges vorhergesagt.

In dieser Arbeit untersuchen wir auch die Röntgenemission von akkretierenden Schwarzen Löchern und Neutronensternen in sternbildenden Galaxien. In massereichen Röntgendoppelsternen akkretiert ein kompaktes Objekt, ein Neutronenstern oder ein Schwarzes Loch, Material von einem massereichen Spenderstern durch stellaren Wind oder den sogenannten Roche-lobe-overflow. Der Spenderstern mit einer Masse von $M_{\text{donor}} \gtrsim 5M_{\odot}$ hat eine Lebensdauer von etwa 10–100 Myr, was mit der Zeitskala der jüngsten Sternentstehungsaktivität von Galaxien vergleichbar ist. Daher wird erwartet, dass die kombinierte Emission von massereichen Röntgendoppelsternen in einer Galaxie mit der Sternentstehungsrate korreliert. Wir erstellen den SRG/eROSITA-IRAS-Katalog mit 1360 sternbildenden Galaxien, der etwa fünfmal größer ist als die in früheren Studien verwendeten Stichproben. Basierend auf der Analyse der Röntgenspektren der Galaxien schätzen wir den Beitrag der Kernaktivität und bereinigen die Stichprobe von Galaxien, die aktive galaktische

Kerne mit geringer Leuchtkraft enthalten. Anhand der SRG/eROSITA–IRAS–Stichprobe von sternbildenden Galaxien untersuchen wir die Skalierungsbeziehung zwischen Röntgenleuchtkraft und Sternentstehungsrate für massereiche Röntgendoppelsterne und das heiße interstellare Medium. Wir verwenden unsere Messung zusammen mit anderen Messungen von L_X/SFR für massereiche Röntgendoppelsterne, um die Metallizitätsabhängigkeit von L_X/SFR für massereiche Röntgendoppelsterne zu untersuchen.

Summary

The white dwarf (WD) in a binary system accretes material from a non-degenerate donor star. Depending on the accretion rate and WD mass, the nuclear burning of the matter on the surface of the WD can proceed in stable or unstable regimes. In a stable regime, classical steady super-soft X-ray sources (SSSs) are observed, emitting extreme ultraviolet and soft X-ray emission. Unstable hydrogen burning on the surface of WDs gives rise to the explosions of classical and recurrent novae. The nova explosion is primarily observed in the optical band. However, nuclear burning of the residual hydrogen on the surface of the WD generates soft X-ray emission, and the system is observed as a post-nova SSS. In this thesis, we study X-ray emission from accreting WDs experiencing stable or unstable thermonuclear burning on their surface. Using the sample of accreting WDs, we estimate the accretion rate on these systems and probe the boundary between two regimes of thermonuclear burning.

In particular, we investigate populations of soft and super-soft X-ray sources in nearby galaxies of various morphological types with particular emphasis on characterizing populations of stable nuclear burning, accreting WDs. Using the Chandra archive, we assembled a sample of nearby galaxies suitable for studying populations of SSSs. We used a combination of hardness ratio and median energy to pre-select X-ray sources with soft spectra and used the temperature–X-ray luminosity diagram to identify nuclear-burning, accreting WDs. For spiral galaxies we found, that there is a distinct and rare population of SSSs that are largely detached from the rest of the soft sources on the X-ray luminosity-temperature plane. The boundary between these sources and the much more numerous population of harder (but still soft) sources is consistent with the boundary of stable hydrogen burning on the surface of WDs. The combined spectrum of soft sources located outside this boundary shows clear emission lines of magnesium (Mg) and sulphur (S) typical for supernova remnants. The sources inside the boundary of stable nuclear burning have super-soft continua without significant line emission and are clear candidates to the accreting nuclear burning WDs. The population of SSSs in spiral galaxies is eight times larger than in lenticular and elliptical galaxies, in broad agreement with the population synthesis calculations. The low specific frequency of SSSs, especially in early-type galaxies, supports the earlier conclusion that they are not the major class of type Ia supernova progenitors.

To investigate accreting WDs with unstable hydrogen burning on their surface, we studied the X-ray emission from hosts of historical Classical Novae (CNe) in our Galaxy. To this end, we used the data of the eROSITA telescope aboard the SRG orbital

observatory obtained in its all-sky survey. Cross-matching the list of historical CNe with SRG/eROSITA sources catalogue, we found that the majority of them are cataclysmic variables (CVs) in a quiescent state. Their X-ray emission is associated with the accretion of material in the binary system and is produced predominantly in the boundary layer near the WD surface and the hot corona of the accretion disk. Among CVs, we discovered two new soft X-ray sources associated with the post-novae phase. A surprisingly large fraction of sources shows hard X-ray spectra, suggesting that these CVs may harbour magnetised WDs.

The CN counterparts represent a bona fide sample of accreting WDs with unstable hydrogen burning on their surface. To probe the boundary between stable and unstable nuclear burning on the surface of accreting WD, we used samples of stable SSSs and CNe in quiescence. We obtained the accretion rate distribution of WDs with unstable hydrogen burning using the X-ray luminosity of CN counterparts in quiescence. We compared it to the accretion rate distribution of known stable SSSs in our and nearby galaxies. We found clear dichotomy between these two distributions, where the CN sources ($\dot{M}_{\text{acc}} \approx 10^{-12} - 10^{-8} M_{\odot}/\text{yr}$) and stable SSSs ($\dot{M}_{\text{acc}} \approx 10^{-7.5} - 10^{-6} M_{\odot}/\text{yr}$) occupy different domains in \dot{M}_{acc} , as predicted by the theory of thermonuclear hydrogen burning on the surface of the WD.

In this thesis, we also study the X-ray emission of accreting black holes (BH) and neutron stars (NS) in star-forming galaxies. In high-mass X-ray binaries (HMXBs), a compact object, a NS or a BH, accretes material from a massive donor star via stellar wind or Roche-lobe overflow. The donor star with the mass of $M_{\text{donor}} \gtrsim 5M_{\odot}$ has a lifetime of about 10–100 Myr, which is comparable to the time-scale of galaxies' recent star formation activity. Therefore, the combined emission of HMXBs in a galaxy is expected to correlate with the star-formation rate (SFR). We construct the SRG/eROSITA–IRAS catalog of 1360 star-forming galaxies which is about five times bigger than samples used in previous studies. Based on the analysis of X-ray spectra of galaxies, we estimate the contribution of the nuclear activity and clean the sample galaxies containing a low luminosity AGN. Using the SRG/eROSITA – IRAS sample of star-forming galaxies, we investigate the scaling relation between X-ray luminosity and SFR for HMXBs and hot ISM. We use our measurement, along with other L_X/SFR measurements for HMXBs, to investigate the metallicity dependence of L_X/SFR for HMXBs.

Chapter 1

Introduction

This chapter considers the main mechanisms generating X-ray emission in a binary system, where a secondary star has evolved into a compact object. Our focus is *white dwarfs* (WDs), accreting mass from the donor stars, and their observed properties as *super-soft X-ray sources* (SSSs); *post-nova SSS* and *quiescent* phases of Classical Novae (CNe) phenomena. Also, we briefly consider the properties of the *high-mass* (HMXBs) and *low-mass* X-ray binaries (LMXBs), mainly accentuating their populations, total X-ray emissions, and connection with properties of host galaxies.

1.1 A synopsis of stellar evolution

Stars are one of the common objects in the Universe. Our understanding of their formation and evolution provides key to the processes of the chemical evolution of the Universe. The evolution of stars is determined by the composition of chemical elements and initial masses. Luminosity and temperature are two parameters used to represent evolutionary tracks of stars on the temperature versus luminosity plane, the so-called Hertzsprung-Russell diagram (H-R diagram). Fig. 1.1 shows the evolutionary track of a solar mass star on the H-R diagram. The main stages of the evolution of a solar mass star ($1 M_{\odot} \approx 2 \times 10^{33}$ g) are following. Everything begins with the gravitational collapse of the molecular cloud and the birth of a young star. For a main-sequence star, its luminosity scales with mass as $L_s \propto M_s^4$ and the lifetime scales with mass as (Mo et al. 2010)

$$t_{\text{H} \rightarrow \text{He}} \propto M_s / L_s \propto M_s^{-3}. \quad (1.1)$$

The lifetime is about $\sim 10^{10}$ yr, which is comparable to the age of the Universe. After the end of hydrogen burning, the star leaves the main sequence branch toward the red giant branch. The effective temperature of the photosphere begins to decrease, but its radius increases. The primary energy source is hydrogen burning which occurs in the layer that surrounds the red giant's helium core. The burning of helium and turning it into carbon, nitrogen and oxygen (the so-called CNO cycle) occurs in the later stages of the star's evolution. In more massive stars ($M_* \gtrsim 8M_{\odot}$), the burning of heavier elements to

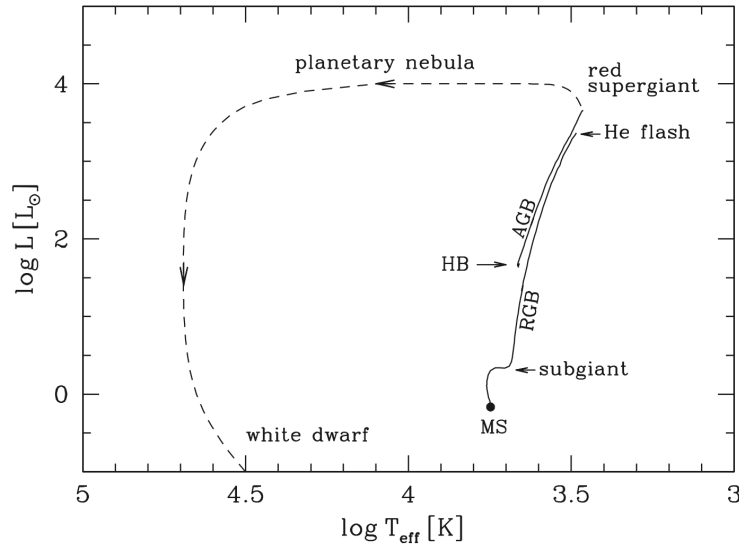


Figure 1.1: An illustration of the H–R diagram and evolutionary track of solar mass star. [Adopted from [Mo et al. \(2010\)](#)]

elements of the iron group takes place. The evolution of stars with various initial masses leads to the formation of different compact objects. For low-mass stars ($0.7 \lesssim M_* \lesssim 1M_\odot$), the final stage of evolution is a WD. A WD is a compact object with a mass on the order of solar M_\odot , but with a size of $\approx 10^9$ cm. The average density is $\approx 10^5$ g cm $^{-3}$. The matter inside the WD is degenerate, so it is described by the equations of state of a degenerate gas, where for the relativistic case pressure (P_e) and density (ρ) are related as

$$P_e \propto \rho^{4/3}. \quad (1.2)$$

For WD, there is a limiting mass (Chandrasekhar mass) above which the object cannot exist because the gravitational force begins to exceed the pressure force of degenerate gas and gravitational collapse leads to the formation of a *neutron star* (NS) or *black hole* (BH). Using the equation of hydrostatic equilibrium, the pressure at the centre of WD is equal to

$$P_{gr} \propto \frac{GM}{R_*} \rho \propto GM^{2/3} \rho^{4/3}, \quad (1.3)$$

where M and R_* are the mass and the radius of the star, respectively. Assuming $P_e \approx P_{gr}$ we obtain the limiting mass of WD ([Prialnik 2009](#))

$$M_{Ch} = 5.83\mu_e^{-2} M_\odot, \quad (1.4)$$

where μ_e^{-1} is the average number of free electrons per nucleon, and for $\mu_e = 2$ a Chandrasekhar's mass limit is $M_{Ch} \approx 1.46 M_\odot$.

For massive stars ($M_* \gtrsim 8 - 10 M_\odot$), the final stage of evolution is the formation of a NS (the mass of the NS is $M_{NS} \lesssim 3 M_\odot$), or a BH (the mass of the BH is $M_{BH} \gtrsim 3 M_\odot$).

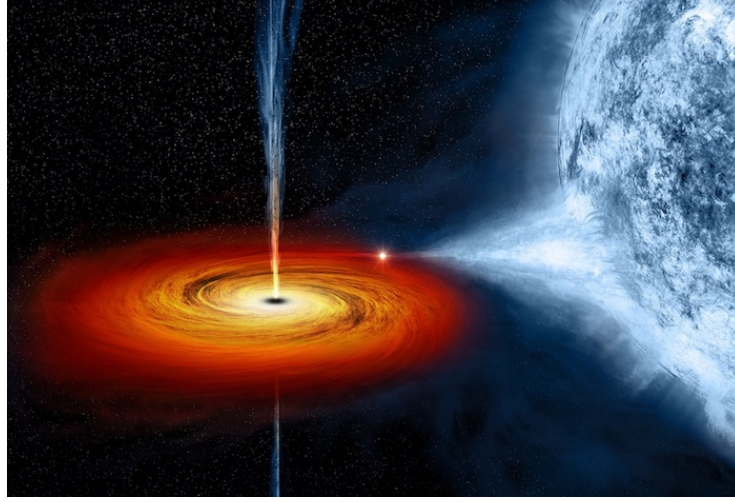


Figure 1.2: An artist's view of an X-ray binary with accretion disk and donor star. [Adopted from NASA/CXC/M.Weiss]

The limiting radius for a BH, the so-called Schwarzschild radius, is defined as

$$R_S = \frac{2GM}{c^2}, \quad (1.5)$$

where for a solar mass BH the radius is about $R_S \approx 3$ km.

1.2 X-ray emission from binary system

1.2.1 Accretion

In binary systems (see Fig. 1.2), the gravitational and centrifugal forces determine the equipotential surface, where (Frank et al. 2002)

$$\nabla\Phi(\vec{r}) = 0, \quad (1.6)$$

and Roche potential Φ is defined as (Frank et al. 2002)

$$\Phi(\vec{r}) = -\frac{GM_1}{|\vec{r} - \vec{r}_1|} - \frac{GM_2}{|\vec{r} - \vec{r}_2|} - \frac{1}{2}(\vec{\omega} \times \vec{r})^2, \quad (1.7)$$

where $M_{1,2}$ are masses of stars, the ω angular velocity of binary system, and $\vec{r}_{1,2}$ are the position vectors of the two stars. Fig.1.3 shows an example of the surface of the Roche potential for binary stars. The two cavities bounding the stars with masses M_1 and M_2 are internal Roche lobes. The approximate analytical solution of Eq.1.6 and 1.7 gives the radius of the Roche lobes as (Frank et al. 2002)

$$\frac{R_2}{a} = \frac{0.49q^{2/3}}{0.6q^{2/3} + \ln(1 + q^{1/3})}, \quad (1.8)$$

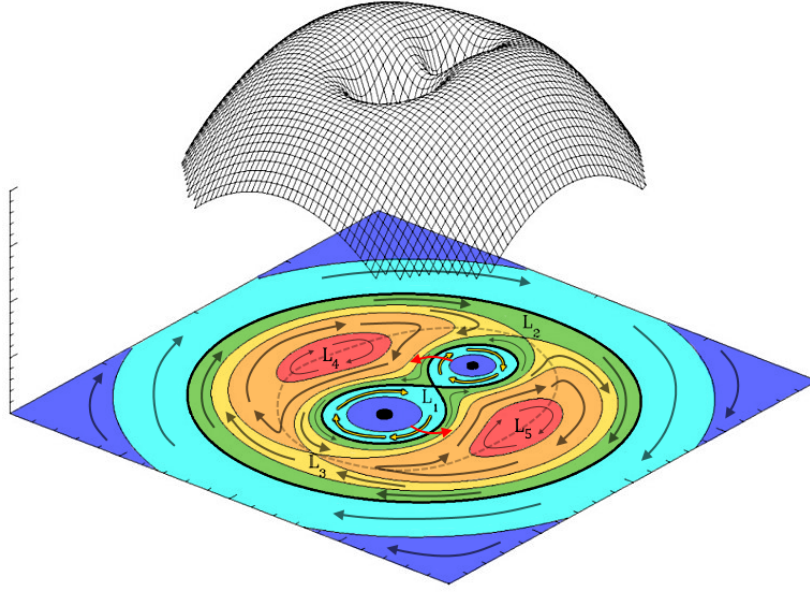


Figure 1.3: Roche potential for binary stars. [Image from Samuel Hon, taken from Wikipedia]

where $q = M_2/M_1$ is a mass ratio. The approximate analytic solution for radius R_1 is given by replacing q by q^{-1} .

After filling the Roche lobe, the donor star loses mass via the inner Lagrange point L_1 , which connects the equipotential surfaces of the two objects. This process is called accretion. During the accretion, the matter within the disk spirals inward and moves toward to compact object by losing angular momentum and energy due to viscosity and turbulence. The layers of the accretion disk rotate close to Keplerian velocities, where the angular velocity is given by

$$\Omega_K(R) = \left(\frac{GM}{R^3} \right)^{1/2}, \quad (1.9)$$

where R is the radial distance to the star. The accretion luminosity is given by (Shakura & Sunyaev 1988; Frank et al. 2002)

$$L_{acc} = \frac{G M \dot{M}_{acc}}{R_*}, \quad (1.10)$$

where \dot{M}_{acc} is an accretion rate, and R_* is radius of the compact object. About half of this luminosity is radiated by an accretion disk. The temperature of the optically thick accretion disk is given by (Shakura & Sunyaev 1988; Frank et al. 2002)

$$T(R) = \left\{ \frac{3GM\dot{M}_{acc}}{8\pi R^3 \sigma_{SB}} \left[1 - \left(\frac{R_*}{R} \right)^{1/2} \right] \right\}^{1/4}, \quad (1.11)$$

where σ_{SB} is Stefan-Boltzmann constant. Each disk element has thermal radiation, and the total spectrum approximates the multi-temperature black-body model. The disk temperature reaches a maximum at $R = (49/36)R_*$, where $T(R) = 0.488 T_*$ and

$$T_* = \left(\frac{3GM\dot{M}_{acc}}{8\pi R_*^3 \sigma_{SB}} \right)^{1/4}. \quad (1.12)$$

The temperature of the accretion disc around NS (or BH) is about $\sim 10^7 K$, and near WD is about $\sim 10^5 K$. NS and BH in the accretion regime are the most powerful stellar mass X-ray sources having luminosities of about $\sim 10^{38}$ erg/s. We can see how efficiently the rest mass energy of the accreted material is converted into radiation, using accretion efficiency η and $L_{acc} = \eta \times \dot{M}_{acc}c^2$. For example, the efficiency of accretion on the surface of solar mass NS is about $\eta \approx 0.2$. For a solar mass WD, the efficiency is about $\eta \approx 10^{-4}$. The hydrogen-to-helium burning gives $\eta \approx 0.007$, which is more efficient for WDs (see below). The accretion of matter onto a compact object, usually NS or BH, also occurs via the stellar wind (e.g., [Hoyle & Lyttleton 1939](#); [Bondi & Hoyle 1944](#)). In HMXBs, a massive donor ($M_{donor} \gtrsim 5M_\odot$) star of spectral class O (or B) loses mass via stellar wind with a rate of $\approx 10^{-6} M_\odot$ /yr.

The accretion leads to the formation of the boundary layer (BL) on the surface of the compact object (NS or WD), where the luminosity of BL is given by

$$L_{BL} = \frac{GM\dot{M}_{acc}}{2R_*} \left[1 - \frac{\Omega_*}{\Omega_K} \right]^2, \quad (1.13)$$

where if the Keplerian velocity exceeds the rotation velocity of the WD surface, i.e. $\Omega_* \ll \Omega_K$, the luminosity is equal to $L_{BL} = 1/2 \times L_{acc}$. In the spherically symmetric accretion, the falling velocity of the matter is equal to free-fall velocity,

$$v_{ff} = \sqrt{\frac{2GM}{R_*}}, \quad (1.14)$$

and the post-shock temperature of the accretion flow hitted to the surface is

$$kT_{s,ff} = \frac{3}{16} \frac{GM\mu m_H}{R_*}. \quad (1.15)$$

In the case of a low-accretion rate $\dot{M}_{acc} \lesssim 10^{-10} M_\odot$ /yr typical of non-magnetic cataclysmic variables (CVs), dwarf novae (DN) in a quiescent state, the BL is optically thin, and hard X-ray emission is observed. As a first approximation, their X-ray spectra have a bremsstrahlung continuum with the temperature equal to Eq. 1.15. At a high-accretion rate $\dot{M}_{acc} \gtrsim 10^{-10} M_\odot$ /yr, the BL becomes optically thick, and soft X-ray emission is observed. An outburst of the DN is one of the examples where the BL becomes optically thick.

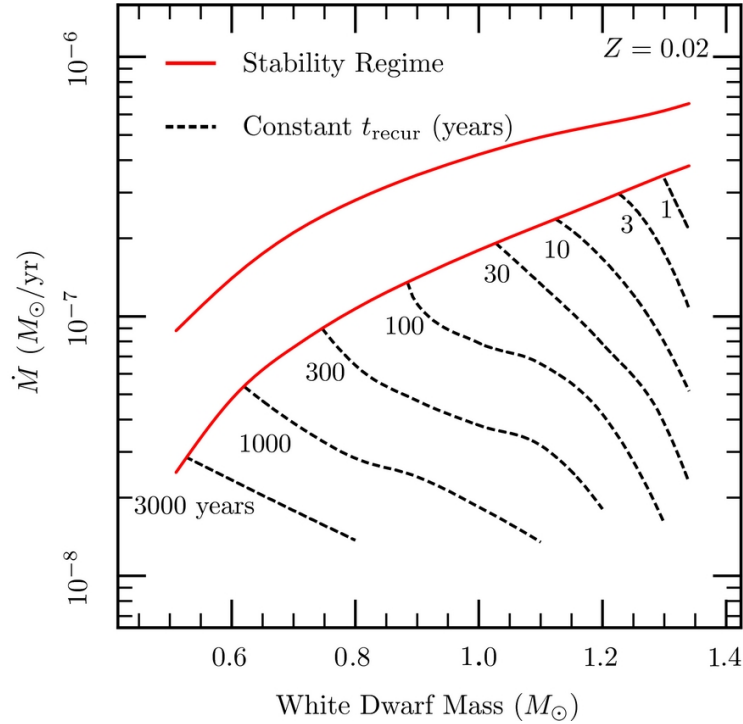


Figure 1.4: Accretion rate versus WD mass plane. *Red lines*: the *stability strip*, where steady hydrogen shell burning occurs on the surface of accreting WD. Above the stability strip: Optically thick winds blow from mass-accreting WDs or pile-up of accreted matter forming a red-giant-like structure; below: Unstable hydrogen burning. *Dotted lines*: Time between classical two nova explosions, i.e. recurrence time for recurrent novae. [Adopted from [Wolf et al. \(2013\)](#)]

1.2.2 Nuclear burning on the surface of accreting WDs

The accumulation of accreting material on the surface of a WD in a close binary system leads to thermonuclear hydrogen burning on its surface. In hydrogen to helium burning,



the energy release is

$$\Delta E_{nuc} = \Delta mc^2, \quad (1.17)$$

where difference in mass is

$$\Delta m = 4m_H - m_{\text{He}} \approx 4.4 \times 10^{-26} \text{ g}, \quad (1.18)$$

and the mass of one hydrogen nucleus is $m_H \approx 1.67 \times 10^{-24} \text{ g}$ and the mass of a helium nucleus is $m_{\text{He}} \approx 6.65 \times 10^{-24} \text{ g}$. The difference between the masses is about $\approx 0.7\%$ of initial mass, i.e.

$$\eta = \frac{\Delta m}{4m_H} \approx 0.007. \quad (1.19)$$

Only $\approx 0.7\%$ of the mass is converted to electromagnetic radiation. As we noted above, for accreting WDs, nuclear burning is a more efficient process to release energy than accretion. Therefore it becomes the primary source of the X-ray emission. The bolometric luminosity of the source is defined as

$$L_{\text{bol}} = \epsilon X_H \dot{M}_{\text{acc}}, \quad (1.20)$$

where $\epsilon \approx 6 \times 10^{18}$ erg/g, and $X_H \approx 0.72$ is the hydrogen mass fraction of accreting material. The effective temperature of an accreting WD powered by nuclear burning of hydrogen on its surface is given by:

$$T_{\text{eff}} = \left(\frac{\epsilon_H X_H \dot{M}_{\text{acc}}}{4\pi R_{\text{phot}}^2 \sigma_{SB}} \right)^{1/4} \approx 67 \left(\frac{\dot{M}_{\text{acc}}}{5 \times 10^{-7} M_{\odot}/\text{yr}} \right)^{1/4} \left(\frac{R_{\text{phot}}}{10^{-2} R_{\odot}} \right)^{-1/2} \text{ eV}, \quad (1.21)$$

where R_{phot} is the photospheric radius of the hydrogen burning layer.

Fig. 1.4 shows accretion rate versus WD mass plane. Steady hydrogen burning on the WD surface occurs when the mass accretion rate from the companion star is close to $\dot{M}_{\text{acc}} \sim 10^{-7} M_{\odot}/\text{yr}$ (the exact values depend on the WD mass), so-called *stability strip*. Numerical calculations show that at the bottom of the stability strip, $R_{\text{phot}} \approx R_{\text{WD}}$ and the photospheric radius increases with increasing \dot{M}_{acc} (Wolf et al. 2013). In this regime, classical steady SSSs are observed (see chapter 1.3.1). At lower mass-accretion rates, $\dot{M}_{\text{acc}} \lesssim 10^{-8} M_{\odot}/\text{yr}$, hydrogen fusion on the surface of WDs is unstable, giving rise to the explosions of classical and recurrent novae (see chapter 1.3.2). At higher accretion rates $\dot{M}_{\text{acc}} \gtrsim 10^{-6} M_{\odot}/\text{yr}$, the rate of matter accumulation on the surface of WD exceeds the burning rate of hydrogen, causing the accreting matter to pile up on the WD. The photosphere of WD will expand by forming a red-giant-like structure, or strong, optically thick winds begin to blow from the WD.

We note, that the details of thermonuclear burning on the surface of WDs are still a matter of debate. Calculations by Nomoto et al. (2007), Wolf et al. (2013) (and references therein) find that hydrogen fusion may proceed steadily above some value of the mass accretion rate in the so-called stability strip. Calculations by Prialnik & Kovetz (1995), Yaron et al. (2005), Starrfield et al. (2013), suggest that nuclear burning is unstable at any mass accretion rate. Although the nova explosion itself is primarily observed in the optical band, nuclear burning of the residual hydrogen on the surface of a WD after the explosion generates soft X-ray emission and the system is observed as a post-nova SSS (Truran & Glasner 1995; Wolf et al. 2013; Soraisam et al. 2016). Thus, the existence of SSSs, steady or not, is envisaged in either scenario.

1.3 Accreting white dwarfs

1.3.1 Super-soft X-ray sources

CAL 83 and CAL 87, the two prototypical SSSs were discovered by Einstein observatory in the course of a survey of the Large Magellanic Clouds (Long et al. 1981). About a decade

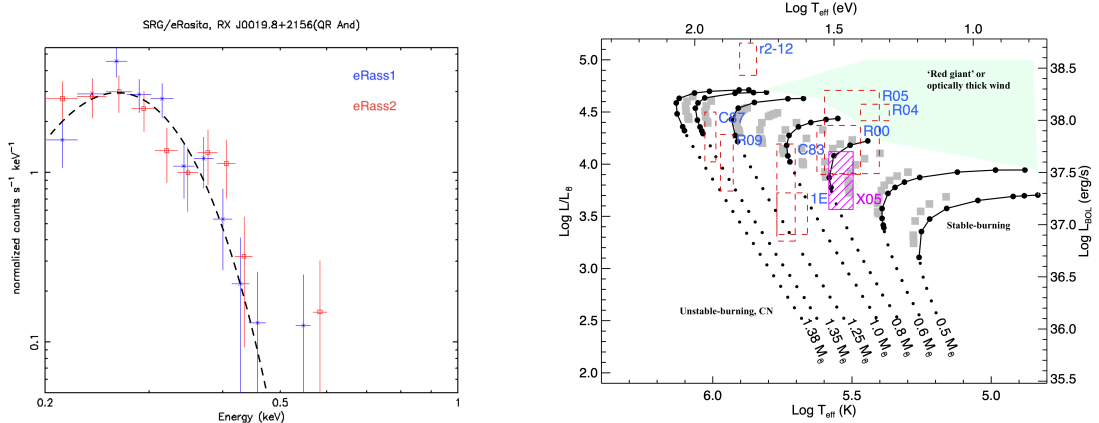


Figure 1.5: *Left:* Example of X-ray spectrum of known SSS in our Galaxy observed by SRG/eROSITA during two all-sky surveys (RU Consortium’s data). *Black, dotted line:* Best-fit with black-body model with temperature $kT \approx 22$ eV and hydrogen column density $N_{\text{H}} \approx 10^{21} \text{ cm}^{-2}$. *Right:* Location of a dozen known SSSs in our and nearby galaxies on H–R diagram. A stable-burning and nova models (*black and grey lines*) from [Nomoto et al. \(2007\)](#) and [Wolf et al. \(2013\)](#). [Adapted from [Vasilopoulos et al. \(2020\)](#)]

later, first light observations of the central region of the LMC with ROSAT observatory led to the discovery of a similar source with a very soft spectrum, RX J0527.8-6954 ([Trümper et al. 1991](#)). With the advent of Chandra and XMM-Newton, similar sources were found in other, more distant galaxies. The spectra of these sources are very soft and do not extend beyond $\sim 1 - 2$ keV, and approximation with the black-body model gives temperatures of the order of $\sim 10 - 100$ eV and bolometric luminosities in the $\sim 10^{36} - 10^{38}$ erg/s range ([Greiner et al. 1991](#); [Kahabka et al. 1994](#)). It is this extreme softness of their spectra that gave rise to their name.

The binary nature of some of these sources (CAL 83 and CAL 87 in the first place) was determined soon after their discovery ([Pakull et al. 1988](#); [Smale et al. 1988](#); [Cowley et al. 1990](#)). Initially, they were thought to be LMXBs but it was soon realised, that the compact object in these binaries is a WD rather than a NS or a BH ([van den Heuvel et al. 1992](#)). The proposition that the main source of energy in SSSs is thermonuclear burning of the accreted hydrogen naturally explained the unusual softness of their X-ray spectra. Since the energy release occurs deep in an optically thick layer of material, it leads to the generation of soft X-ray emission with a nearly black-body spectrum and a temperature $\approx 10 - 100$ eV. The combination of the energy output expected in hydrogen fusion and the surface area of a typical WD giving effective temperatures in the correct range, close to the observed values.

The left panel of Fig. 1.5 shows X-ray spectrum QR Andromeda, one of the known SSS in our Galaxy, obtained by SRG/eROSITA observatory during two all-sky surveys (data of RU

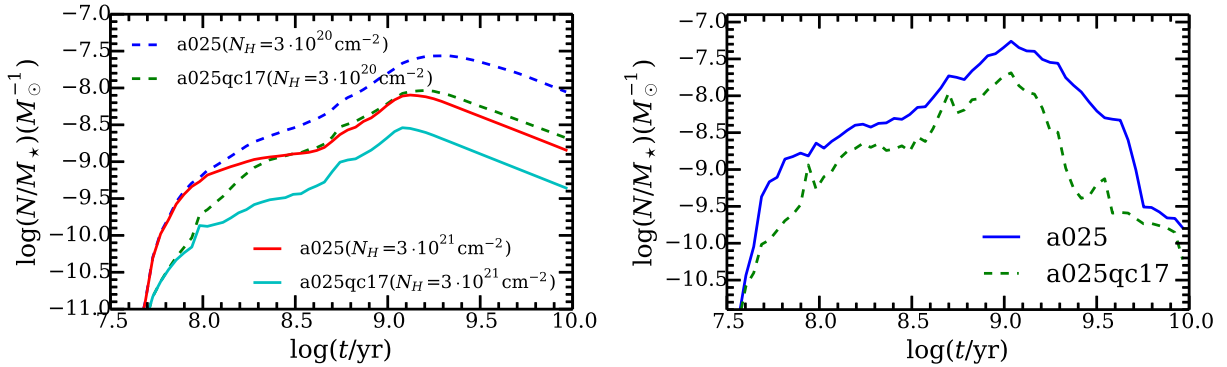


Figure 1.6: Evolution of the population of SSSs over lookback time. The y-axis shows the specific frequencies of SSSs, i.e. number of objects divided by the total stellar mass of galaxies. Two types of galaxies were assumed on the simulations by [Chen et al. \(2015\)](#) using the MESA code ([Paxton et al. 2011, 2013](#)). The galaxy has active star-formation with the constant SFR of $1 M_{\odot}/\text{yr}$ during 10 Gyr (left). The galaxy is like an elliptical, where all stellar mass $M_* = 10^{11} M_{\odot}$ was formed at the $t=0$, and the population of SSSs evolve up to 10 Gyr (right). [Adopted from [Chen et al. \(2015\)](#)]

Consortium). Source does not have X-ray emission above $\gtrsim 0.5$ keV and its spectrum is well approximate with the black-body model with temperature $kT \approx 22$ eV. The right panel of [Fig.1.5](#) shows an H–R diagram for a dozen known SSSs in our and nearby galaxies. Their temperature and bolometric luminosities are consistent with the stable-burning model on the surface of accreting WDs. Observational studies of SSS populations are often impeded by the extreme softness of their spectra, making searches for and characterization of these objects difficult. Owing to the observations of the ROSAT, Chandra, XMM-Newton X-ray observatories, more than a hundred SSSs have been discovered in our and nearby galaxies (e.g., [Swartz et al. 2002](#); [Di Stefano & Kong 2003, 2004](#); [Pietsch et al. 2005](#); [Galiullin & Gilfanov 2021a](#)).

There is still no complete understanding of how the population of nuclear burning, accreting WDs is related to the fundamental properties of their host galaxies, such as their stellar mass, star-formation rate, star-formation history, and metallicity. On the theoretical side, there have been several attempts to address this problem by means of population synthesis calculations (e.g., [Yungelson & Livio 1998](#); [Yungelson 2010](#)). Recently, [Chen et al. \(2014, 2015, 2016\)](#) implemented hybrid population synthesis calculations using the MESA code ([Paxton et al. 2011, 2013](#)) to compute the mass-transfer phase of binary evolution. [Chen et al.](#) produced a model that is in reasonable agreement with a number of existing constraints on the soft X-ray luminosities and average intensity of the ionizing radiation field, as well as with statistics of classical novae in nearby galaxies (see [Fig. 1.6](#)).

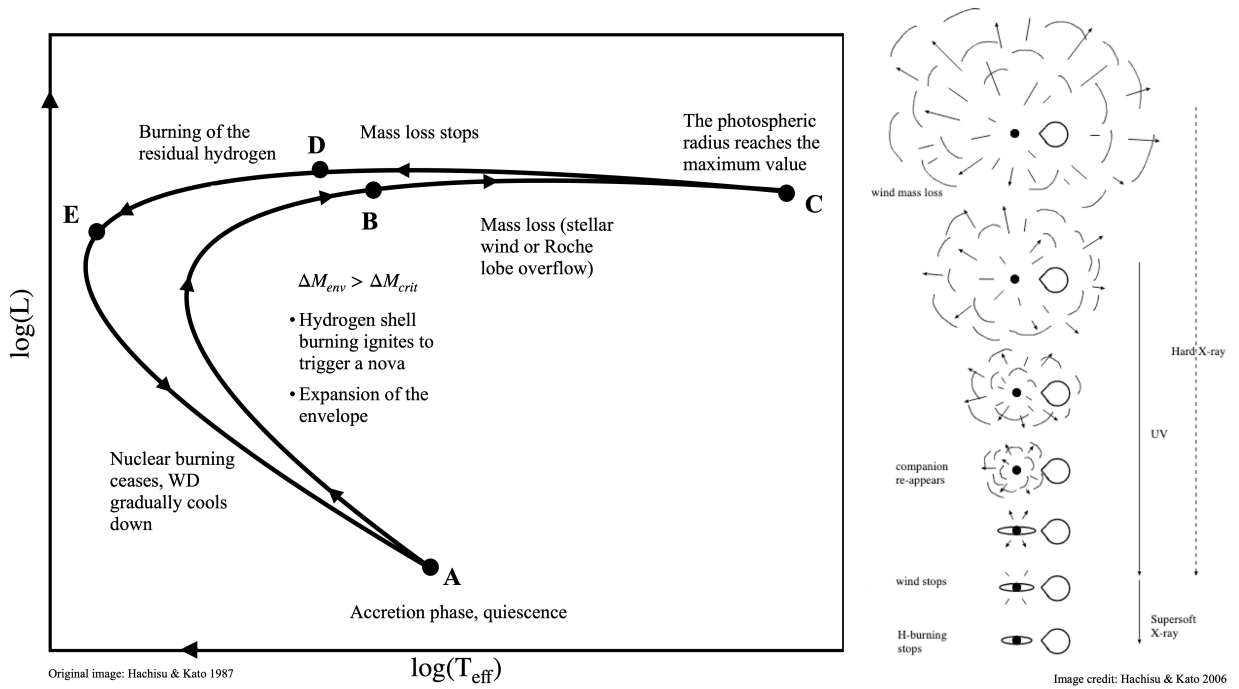


Figure 1.7: A schematic view of the path of one nova cycle on the H–R diagram (left). Illustrative images of the mass-loss process via stellar wind after the nova explosion (right). For more detail see section 1.3.2. [Adapted from Kato & Hachisu (1989); Kato (2010)]

1.3.2 Classical Novae phenomena

At lower accretion rates $\dot{M}_{\text{acc}} \lesssim 10^{-8} M_{\odot}/\text{yr}$, thermonuclear hydrogen burning becomes non-steady, leading to the phenomenon of CNe (for a review, see, e.g., Chomiuk et al. 2020). The envelope mass ΔM_{ign} required to ignite hydrogen burning is given by hydrostatic equilibrium (Prialnik 2009)

$$\Delta M_{\text{ign}} \approx \frac{4\pi P_{\text{ign}} R_*^4}{G M}, \quad (1.22)$$

where critical pressure to run thermonuclear runaway is $P_{\text{ign}} \approx 10^{18} \text{ dyn cm}^{-2}$. For the WD, mass-radius relation is $R \propto M_{\text{WD}}^{-1/3}$, and ignition mass becomes

$$\Delta M_{\text{ign}} \propto M_{\text{WD}}^{-7/3}. \quad (1.23)$$

Thus in the case of massive WD, a less accreted envelope mass is required to ignite a nova explosion. A total energy $\approx 10^{45} \text{ erg}$ is released during a CN outburst. A nova outburst leads to the ejecta of the envelope into the interstellar medium. (see, e.g., Kato & Hachisu 1994; Hachisu & Kato 2006). An X-ray emitting shock can be formed when the expanding ejecta interact with the interstellar medium or the wind from the donor star (see, e.g., Brecher et al. 1977). The X-ray shock emission has a thermal spectrum with a temperature $kT \gtrsim 1 \text{ keV}$ and a luminosity $L_X \approx 10^{33} - 10^{35} \text{ erg/s}$ (see, e.g., Balman et al. 1998; Orio et al. 2001).

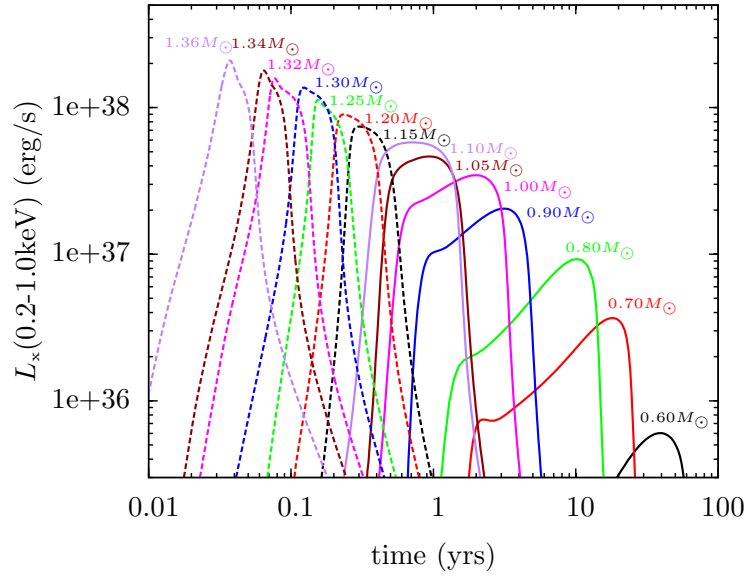


Figure 1.8: Theoretical light curves for post-nova super-soft X-ray phase for different WD mass. Luminosity is given for the 0.2–1 keV energy band. [Adopted from Soraisam et al. (2016)]

Fig. 1.7 shows a schematic view of the path of one nova cycle in the H–R diagram. Before hydrogen shell flash, accreting WD stays in the accretion phase, so-called “quiescence” (point A). When the mass of the accreted material exceeds critical mass, hydrogen shell burning ignites to trigger a nova. WD’s envelope expands and wind mass-loss begins (point B). The energy generated by nuclear burning balances with the energy lost from the photosphere, and the photospheric radius reaches a maximum value (point C). The radius of the photosphere decreases and its temperature increases, and the wind mass loss stops at point D. Photospheric radius becomes optically thin, and the burning of residual hydrogen after the nova explosion generates soft X-ray emission which is seen by observers. Nuclear burning ceases and WD gradually cools down, returning to the accretion phase (point E).

Post-nova X-ray phase

Thermonuclear burning of the material left after the CN outburst on the WD surface leads to the generation of a decaying supersoft X-ray emission, and a post-nova SSS phase is observed once the ejecta have cleared (see, e.g., Ness et al. 2007; Schwarz et al. 2011; Henze et al. 2010, 2011, 2014). The source spectrum during the post-nova SSS phase is characterized by the absence of emission above $\gtrsim 1$ keV. As a rule, the spectrum is described by a black-body model with a temperature $\lesssim 70$ eV, that decreases with time (see, e.g., Oegelman et al. 1993; Krautter et al. 1996; Ness et al. 2011). The duration of the post-nova supersoft X-ray phase depends on the accretion rate before the CN outburst and the WD mass (see, e.g., Hernanz & Sala 2010; Soraisam et al. 2016). The theoretical calculations

describing the relation between the duration and maximum effective temperature of the post-nova SSS phase (Wolf et al. 2013) are consistent with the observations of CNe in the galaxy M31 (Henze et al. 2010, 2011, 2014).

Quiescent phase

Once the post-nova SSS emission has ended, the source returns to the “quiescent phase” in which the main energy source is the accretion of material from the companion star. The X-ray emission from cataclysmic variables in the quiescent phase is generated in the accretion disk, the boundary layer, and the optically thin, comparatively hot corona above the accretion disk (see, e.g., Pringle 1977; Tytenda 1981; Patterson & Raymond 1985a,b; Shakura & Sunyaev 1988). In this regime, the CN counterparts manifest themselves as dwarf novae whose outbursts are associated with thermal instability in the accretion disk (see, e.g., Meyer & Meyer-Hofmeister 1984, 1994). The luminosity of CVs outside dwarf nova outbursts characterizes the true accretion rate in such systems.

1.3.3 Possible progenitors of type Ia supernovae

SN Ia are important sources to measure distances in the Universe (e.g., Riess et al. 1998). They are observed to explode in early- and late-type galaxies. From observations, it becomes clear that the thermonuclear runaway triggers an explosion of SN Ia. The likely candidate is carbon-oxygen WD. However, before exploding as an SN Ia, a WD needs to increase its mass from the initial value, typically in the $\sim 0.5 - 1.0 M_{\odot}$ range, to near the Chandrasekhar mass limit of about $\sim 1.4 M_{\odot}$. Two main scenarios are considered: single-degenerate (SD) and double-degenerate (DD). In the DD scenario, the two WDs orbit each other. The more-massive WD tidally disrupts and accretes the lower-mass WD, and finally merges. The loss of energy and angular momentum happens due to gravitational wave radiation (Tutukov & Yungelson 1981; Iben & Tutukov 1984). For review, see Maoz et al. (2014).

In the SD scenario, WD accretes mass from the nondegenerate donor stars via the Roche-lobe overflow (Whelan & Iben 1973; Nomoto 1982). The way to increase mass for an accreting WD is steady state burning of hydrogen and/or helium on its surface. The mass growth is most efficient when nuclear burning is stable; as in all other regimes, it is counteracted by various mass-loss processes. However, growth of the WD mass is also possible in specific domains of the parameter space when the burning is unstable (Starrfield et al. 2013; Hillman et al. 2015).

Overall, despite the SD scenario being a favoured model, the properties of the possible progenitor populations of SNe Ia do not match the theory, and the problem is still under debate. For example, the SSSs are examples of binary systems, where WDs accrete matter from nondegenerate donor stars. Nevertheless, it was demonstrated that the number of SSSs (Di Stefano 2010) and their total luminosity in the X-ray (Gilfanov & Bogdán 2010; Bogdán & Gilfanov 2011) and UV (Woods & Gilfanov 2013; Johansson et al. 2014; Woods

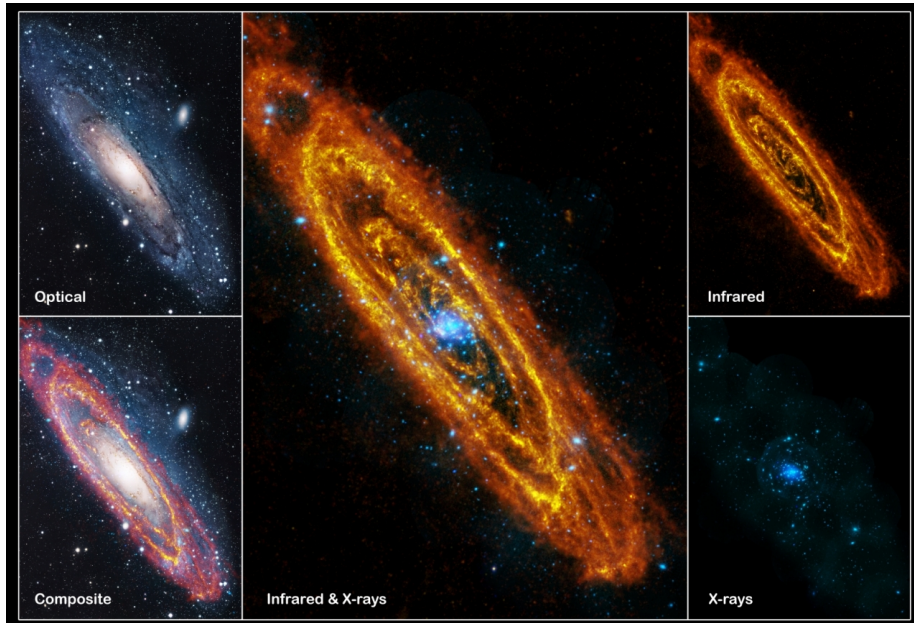


Figure 1.9: A view of Andromeda Galaxy (M31) at different multi-wavelengths. The infrared wavelength shows the galaxy’s spiral structure and dust heated by young massive stars. The X-ray image shows point sources, primarily associated with HMXBs and LMXBs, and background AGNs. On the combined infrared and X-ray image, the sources concentrating in the centre of M31 are mostly LMXBs. The sources located in the spirals of M31 are HMXBs. [Adopted from NASA; infrared: ESA/Herschel/PACS/SPIRE/J. Fritz, U. Gent; X-ray: ESA/XMM-Newton/EPIC/W. Pietsch, MPE; optical: R. Gendler]

& Gilfanov 2014) bands in nearby galaxies is far too insufficient to explain the observed SN Ia rates.

1.4 X-ray binaries and their connections with properties of host-galaxies

One of the main processes driving galaxy formation and evolution across the Universe is star formation. The star formation history (SFH) shows when galaxies formed their stars and assembled their mass over evolutionary time scales. The current star-formation rate (SFR) shows how galaxies formed their stars during the past $\approx 10 - 100$ Myr. Calibration of SFR tracers is based on direct observations of galaxies across the entire electromagnetic spectrum, from X-ray to radio wavelengths. The conversion factors of luminosities at different wavelengths to SFR are usually derived from population-synthesis models under some assumptions regarding stellar spectral energy distribution (SED) and initial mass function (IMF). For example, ultraviolet (UV) emission is produced by young massive stars of O and early-B spectral types and therefore it is a direct indicator of the current

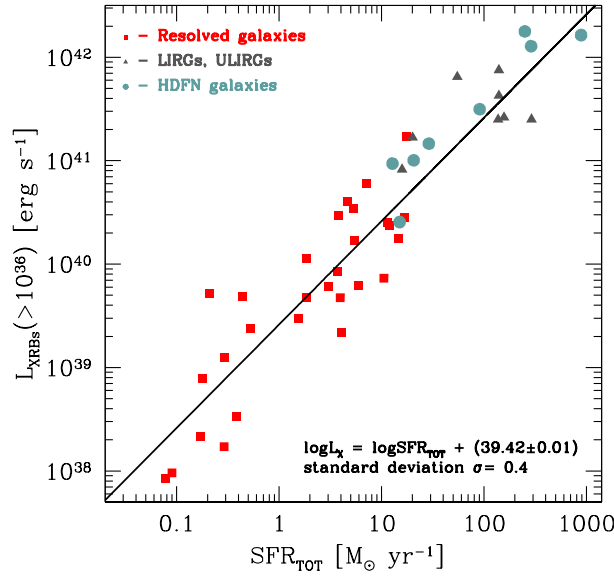


Figure 1.10: An example of scaling relation between the total X-ray luminosity of HMXB populations and SFR of host galaxies. The total luminosities were estimated by integrating the observed luminosity function of the HMXB populations above 10^{36} erg/s. [Adopted from Mineo et al. (2012a)]

SFR of a galaxy. Interstellar dust absorbs (some fraction) UV emission from young massive stars and re-emits it in infrared (IR) band. Therefore IR emission is also a good tracer of the recent star formation activity in a galaxy. SFR tracers are not limited only to UV or IR wavelengths. Various SFR proxies are based on line emission (most common $H\alpha$, OIII), as well as composite multi-wavelength estimators are also in use (see reviews by Kennicutt 1998; Kennicutt & Evans 2012; Calzetti 2013). The integrated X-ray emission of star-forming galaxies has been proposed as a possible tracer of recent SFR (e.g., Sunyaev et al. 1978; Bauer et al. 2002; Grimm et al. 2003; Ranalli et al. 2003; Lehmer et al. 2008, 2010; Mineo et al. 2014; Symeonidis et al. 2014). The correlation is mainly caused by the population of HMXBs, where a compact object, a NS or a BH, accretes material from a donor star via stellar wind or Roche-lobe overflow. In an HMXB, the massive donor star with the mass of $M_{\text{donor}} \gtrsim 5M_{\odot}$ has a lifetime of about 10–100 Myr, which is comparable to the time-scale of galaxies' recent star formation activity. For this reason, the combined emission of HMXBs in a galaxy should be expected to correlate with the SFR. Thanks to Chandra and XMM-Newton observatories, it was shown that this is indeed the case – the total X-ray luminosity of HMXBs and their total number correlate with the SFR of the host galaxy (e.g., Grimm et al. 2002, 2003; Gilfanov et al. 2004; Shtykovskiy & Gilfanov 2005, 2007; Mineo et al. 2012a; Lehmer et al. 2019) (see Fig.1.10).

Another component of X-ray emission from star-forming galaxies is the hot, diffuse gas in supernova remnants and in the interstellar medium (ISM). The ISM in star-forming galaxies is heated and enriched with metals via supernova explosions and stellar winds.

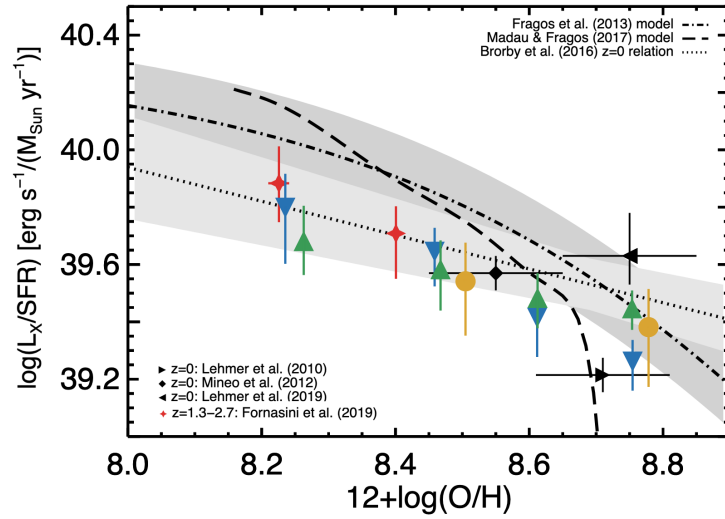


Figure 1.11: An example of scaling relation between L_X/SFR and gas-phase metallicities of star-forming galaxies. Galaxies at different redshifts are marked with different colors. Enhancement of L_X/SFR happens for low metallicity galaxies. For more detail see section 1.4. [Adopted from Fornasini et al. (2020)]

It has been shown that the total luminosity of this gas also correlates with SFR (e.g., Grimes et al. 2005; Owen & Warwick 2009; Mineo et al. 2012b). The hot gas is the main contributor to the soft X-ray emission of star-forming galaxies. X-ray spectra of hot ISM can be described with optically thin thermal emission of plasma with the mean temperature of $kT \sim 0.2 - 0.3$ keV. In some galaxies a second higher temperature component with $kT \sim 0.7$ keV is also required (e.g., Mineo et al. 2012b; Lehmer et al. 2022a). The populations of X-ray sources in star-forming galaxies is not only limited to HMXBs. Some population of LMXBs is present, where the low-mass donor star with $M_{\text{donor}} \lesssim 1M_{\odot}$ has a lifetime in the $\approx 1 - 10$ Gyr range. The long lifetime of the donor star defines the dependence of the LMXB populations on the SFH of the galaxy. The total number and X-ray luminosity of LMXBs correlate with the total stellar masses of their host galaxies (e.g., Gilfanov 2004; Zhang et al. 2012; Lehmer et al. 2014, 2020). There are also faint X-ray sources with X-ray luminosities in the $10^{31} - 10^{35}$ erg/s range, such as cataclysmic variables, active binaries, and young stellar, as well as faint HMXBs and LMXBs. They contribute to the unresolved emission, contaminating studies of hot gas in star-forming galaxies (Mineo et al. 2012b).

The populations of HMXBs in galaxies are also interesting in the cosmological context. They might have played some role in the re-ionization of the intergalactic medium at redshifts of $z \gtrsim 6 - 8$ (e.g., Fragos et al. 2013b). In a low metallicity environment, the primary star, usually a young massive O/B star, will lose less mass from line-driven wind over its lifetime. This leads to the formation of a more massive compact object, often producing BH instead of NS. The accretion rate of X-ray binaries (XRBs) with BH is typically higher than XRBs with NS, and hence, the X-ray luminosity of XRBs with BH accretor is higher. Overall, the prediction is that increase in the total X-ray luminosity of

HMXBs per unit SFR over redshift results from the metallicity evolution of the Universe.

Using stacking analyses, the X-ray emission of star-forming galaxies has been measured up to redshift $z \approx 7$ in the Chandra Deep fields (e.g., [Lehmer et al. 2016](#)). The scaling relations of high-redshift star-forming galaxies were estimated by taking into account the redshift and the contribution of LMXBs (the stellar mass dependence). The observed scaling relations evolve with redshift, as $L_X/\text{SFR} \propto (1+z)^\alpha$ and $\alpha \sim 1$ (e.g., [Basu-Zych et al. 2013a](#); [Lehmer et al. 2016](#); [Aird et al. 2017](#); [Saxena et al. 2021](#)), which follows the trend of [Fragos et al. \(2013a\)](#). The metallicity evolution of the L_X/SFR was indirectly probed by studying the population of HMXBs in galaxies with low metallicities, such as blue compact dwarf galaxies (BCD) and Lyman break analogues (LBA) (e.g., [Mapelli et al. 2010](#); [Kaaret et al. 2011](#); [Basu-Zych et al. 2013b](#); [Prestwich et al. 2013](#); [Brorby et al. 2014](#); [Douna et al. 2015](#); [Brorby et al. 2016](#); [Basu-Zych et al. 2016](#); [Bayliss et al. 2020](#); [Fornasini et al. 2020](#); [Lehmer et al. 2021, 2022a](#)) (see [Fig.1.11](#)). These studies suggest that the L_X/SFR correlates with the gas-phase metallicity; however, quantitatively, some variations still exist.

1.5 Outline of the thesis

The main results of this thesis are reported in two published papers ([Galiullin & Gilfanov 2021a,b](#)) and one *in preparation* work (Galiullin et al.). The thesis is structured as follows:

In [Chapter 2](#) we continue the observational line of investigation of populations of accreting WDs. To this end, we attempted to construct a suitable sample of galaxies from the *Chandra* archive to search for SSSs and implemented efficient source classification algorithms. Our goal is to identify steady nuclear burning, accreting WDs and to estimate their specific frequencies in early- and late-type galaxies.

In [Chapter 3](#) we study X-ray emission from sources associated with historical CNe in our Galaxy using *SRG/eROSITA* data. We call these objects “CN X-ray counterparts” for short, and use the term “X-ray emission from CN counterparts” to denote the X-ray emission detected from historical CNe in quiescence or the post-nova SSS phase. The CN X-ray counterparts are confirmed cases of accreting WDs with unstable hydrogen burning on their surface. Our goal is (i) to study the X-ray properties of a large sample of CN counterparts, (ii) to search for counterparts in the post-nova SSS phase.

Next, in [Chapter 4](#) we construct the accretion rate distribution of CN counterparts, where unstable hydrogen burning is expected. We compare it with the accretion rate distribution of known steady SSSs in our Galaxy and nearby external galaxies from [Chapter 2](#), and with theoretical predictions.

In [Chapter 5](#) we make the first attempt in utilizing the sample of eROSITA normal galaxies. We study X-ray emission of star-forming galaxies identified with the help of IRAS faint source catalog. Using the sample of X-ray detected star-forming galaxies, we investigate the relation between X-ray and IR luminosities, and SFR. Thanks to the depth and all-sky coverage of eROSITA and IRAS catalogs, we construct SRG/eROSITA–IRAS catalog of star-forming galaxies which is about five times bigger than used in previous

studies. This work will be submitted for publication soon.

Finally, Chapter 6 summarizes the main findings of this thesis.

Chapter 2

Populations of super-soft X-ray sources in galaxies of different morphological types

The contents of this chapter is based on the work originally published as Galiullin & Gilfanov (2021a), Astronomy & Astrophysics 646, A85

2.1 Sample of nearby galaxies

We selected galaxies for our analysis from the Chandra observatory archive for cycles 1–20. To this end, we selected observations from the following categories: normal galaxies, active galaxies and quasars, clusters of galaxies, galactic diffuse emission, and surveys. Only archival observations with the Advanced CCD Imaging Spectrometer (ACIS) detector without grating were selected. For each galaxy, we grouped observations made within the same Chandra cycle and selected the group with the largest total exposure time. We then cross-matched aim-point positions of selected *Chandra* observations with positions of galaxies in the RC3 catalog (de Vaucouleurs et al. 1991) to select potentially interesting observations. For each galaxy, we used a match radius of $0.5 \times D_{25}$. The parameters of galaxies for further selection were computed as follows. Stellar masses were computed from K_s band luminosities using mass-to-light ratios computed following the prescription of Bell & de Jong (2001). Classifications of galaxies, distances, and K_s -band magnitudes were taken from the HyperLeda¹ catalog (Makarov et al. 2014) and the Updated Nearby Galaxy Catalog (Karachentsev et al. 2013). Absorption-corrected $(B-V)_0$ colors were taken from the RC3 catalog.

¹<http://leda.univ-lyon1.fr/>

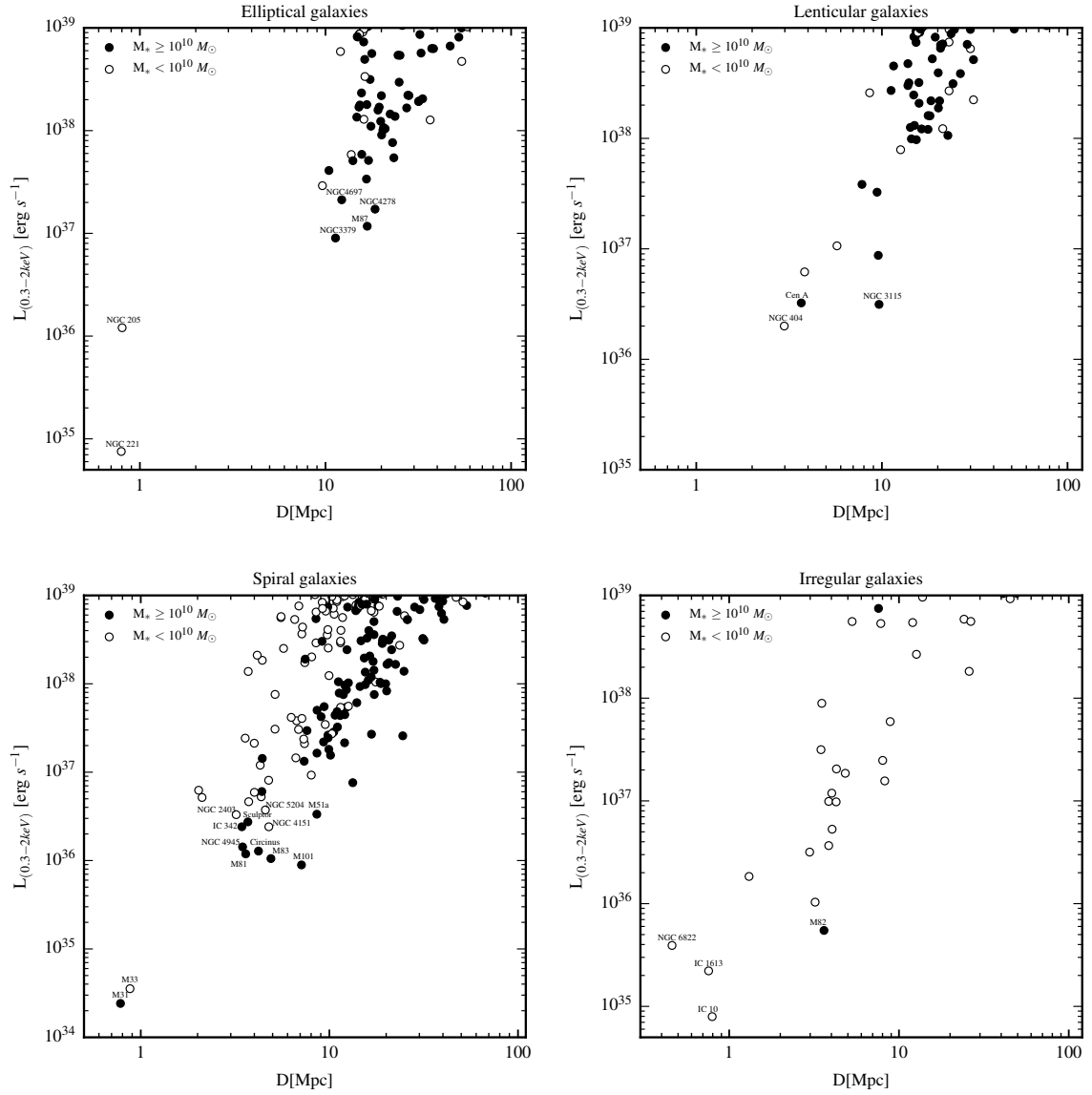


Figure 2.1: X-ray sensitivity–distance diagram of nearby galaxies observed by *Chandra* up to cycle 20. Each panel corresponds to a certain morphological type of galaxy. Filled (open) symbols correspond to galaxies with stellar mass $M_* \geq 10^{10} M_{\odot}$ ($M_* < 10^{10} M_{\odot}$). See Section 2.1 for details.

Table 2.1: List of nearby galaxies used to study populations of soft and SSSs.

Name	Type	D	Angular size	(B–V) ₀	M _*	N _{H,Gal}	SFR
		(Mpc)	(D ₂₅ × d ₂₅ ; PA)	RC3	(10 ¹⁰ M _⊙)	(10 ²⁰ cm ^{−2})	(M _⊙ /yr)
(1)	(2)	(3)	(4)	(5)	(6)	(7)	(8)
NGC 5236 (M83)	Sc	4.6	12.9′ × 11.5′; 54°	0.61	3.0	4.12	3.1
NGC 5194 (M51)	SABb	7.6	11.2′ × 6.9′; 173°	0.53	4.5	3.33	2.9
NGC 5457 (M101)	SABc	6.7	28.8′ × 26.9′; 36°	0.44	2.3	8.58	2.9
NGC 3031 (M81)	Sab	3.6	26.9′ × 14.1′; 157°	0.82	5.4	10.2	0.5
NGC 5128 (Cen A)	S0	3.4	25.7′ × 20.0′; 35°	0.88	4.9	2.35	0.8
NGC 3115	E-S0	9.7	7.2′ × 2.5′; 40°	0.94	6.9	3.88	–
NGC 3379	E	10.6	5.4′ × 4.8′; 71°	0.94	5.8	2.65	–
NGC 4278	E	16.1	4.1′ × 3.8′; 22.7°	0.90	6.0	2.04	–
NGC 4697	E	11.7	7.2′ × 4.7′; 70°	0.89	6.0	2.08	–

Notes: (1) – Galaxy name. (2) – Morphological type from the HyperLeda catalog (Makarov et al. 2014). (3) – Distances to galaxies obtained by the following methods: Cepheids: M83 (Saha et al. 2006), M81 and M101 (Freedman et al. 2001), Cen A (Ferrarese et al. 2007); planetary nebulae luminosity function: M51 (Ciardullo et al. 2002); surface brightness fluctuations: NGC 3379, NGC 3115, NGC 4278, NGC 4697 (Tonry et al. 2001). (4) – Major D₂₅, minor d₂₅ diameters and PAs from RC3 catalog (de Vaucouleurs et al. 1991). For several galaxies, PAs were adopted from elsewhere: M83 (Ho et al. 2011); M51 (Colombo et al. 2014); M101 (Hu et al. 2018); NGC 3379 and NGC 4278 (Peletier et al. 1990). (5) – The total color indexes corrected for galactic and internal extinction from RC3 catalog. (6) – Stellar mass within D₂₅ of the galaxy obtained by mass-to-light ratio for K_s band with color index (B–V)₀ from RC3 using calibration from Bell & de Jong (2001). Total K_s magnitudes were calculated using data from 2MASS Large Galaxy Atlas (Jarrett et al. 2003). The absolute K_s magnitude of the Sun was assumed to be K_{s,⊙}=3.27 (Willmer 2018). (7) – Galactic absorption column densities (HI4PI Collaboration et al. 2016). (8) – Star formation rates of spiral galaxies were adopted from Jarrett et al. (2013), for Centaurus A from Espada et al. (2019). Values were corrected to the distance given in column (3).

2.1.1 Selection criteria

We built our selection procedure based on the following considerations.

i) Stellar mass of the host galaxy. Population synthesis calculations of [Chen et al. \(2014, 2015\)](#) predict specific frequencies of observable (apparent luminosity $L_X > 10^{36}$ erg/s) stable nuclear burning, accreting WDs in spiral galaxies after 10 Gyr of evolution at the level of $\sim 4 \times 10^{-10}$ ($\sim 2 \times 10^{-9}$) sources per M_\odot , assuming an absorbing column density of 3×10^{21} (3×10^{20}) cm^{-2} . For elliptical galaxies, the prediction of these latter authors is $\sim 10^{-10}$ sources per M_\odot for a hydrogen column density of 3×10^{20} cm^{-2} . Based on these predictions we only consider sufficiently massive galaxies with stellar masses $M_* \gtrsim 10^{10} M_\odot$, in which we can expect to find $\gtrsim 1$ nuclear burning, accreting WDs.

ii) Distance. We excluded a few large nearby galaxies from our analysis that do not fit, by a large margin, in the Chandra field of view and require the analysis of mosaics of a large number of observations. These are the Magellanic Clouds, M31 and M33. We would have also excluded too distant galaxies that suffer from confusion, but they are automatically excluded based on the sensitivity arguments (item (iv) below)

iii) Inclination angle. Source populations in spiral galaxies which are viewed close to edge-on will be obscured by large intrinsic absorption by gas and dust in the disk, essentially reducing the number of expected super-soft sources to zero. Therefore, in selecting late-type galaxies we applied a criterion $i < 70$ degrees. For this reason, Sculptor and NGC 4945 for example, were not included from our final sample. No inclination cut was applied to early-type galaxies.

iv) Sensitivity limit of available archival data. The sensitivity limit of archival data can be estimated as follows:

$$L_X \approx 4\pi D^2 \times ECF \times \frac{S}{t}, \quad (2.1)$$

where D is distance to the galaxy, ECF is the counts-to-ergs conversion factor, S is the limiting number of source counts required to detect and characterize a source, t is the total exposure time of archival data. We assumed a black body model with temperature 60 eV and require $S = 20$ counts to detect and classify a source. For each galaxy we obtained ECF from the black-body model ($kT = 60$ eV) modified by the Galactic absorption column density in the direction of the galaxy. For the latter, we used the HI4PI data ([HI4PI Collaboration et al. 2016](#)). For cycles 7–20, in computing the ECF, we used the ACIS detector aim-point response files from the *Chandra* Calibration Database². For cycles 1–6 we generated aim-point response files ourselves. Circinus (5.3×10^{21} cm^{-2}) and IC 342 (3.6×10^{21} cm^{-2}) galaxies with high Galactic absorption column densities were excluded from our sample. We also excluded M87 and M82 due to the presence of bright and complex diffuse emission in these galaxies.

We plot the distribution of galaxies of various morphological types on the distance–sensitivity limit plane in [Fig.2.1](#). Based on these data we selected spiral galaxies M51, M81, M83, M101, lenticular galaxies Cen A and NGC 3115, and elliptical galaxies NGC

²<ftp://cxc.cfa.harvard.edu/pub/caldb/>

3379, 4278, and 4697. For elliptical galaxies, sensitivity limits of the archival Chandra data exceed 10^{37} erg/s, but this is compensated by zero intrinsic absorption in these galaxies; see Section 2.4.2.

We experimented with the selection criteria in order to check whether or not our sample can be improved by adding a few galaxies lying on the boundary of our luminosity and stellar mass selection. Nevertheless, we found that when relaxing the sensitivity threshold, we need to raise the luminosity cut on the $kT_{bb} - L_X$ plane (Section 2.4.2) which actually leads to the loss of super-soft sources of lower luminosity and degradation of the statistical accuracy of our analysis. Adding less-massive galaxies below the assumed cut of $10^{10} M_\odot$, on the other hand, does not lead to a quick improvement of the sensitivity of our selection to the populations of SSSs as the total mass already included in the analysis exceeds $\approx 4 \times 10^{11} M_\odot$. We therefore conclude that the list of galaxies assembled here is reasonably optimal for the current analysis. The basic parameters of these galaxies are summarized in Table 5.1.

2.2 Observations and data reduction

The observations were processed by following a standard CIAO (Fruscione et al. 2006) threads³ (CIAO version 4.8 and CALDB version 4.7.1). We used tool *chandra_repro* to reprocess data and create level 2 event files. To improve absolute astrometry we used *wcs_match* and *wcs_update*. Astrometry correction was done relative to the observation with the longest exposure time using positions of bright X-ray sources to match frames. Event files were merged by *reproject_obs* with the aim-point position of the observation with the longest exposure taken as the reference. Combined images and exposure maps were obtained running *flux_obs*. In Table 2.2 we present brief information on the observations used in the analysis. Detail information is available in Appendix 2.2.

³<http://cxc.harvard.edu/ciao/index.html>

Table 2.2: Properties of galaxies and statistics of their X-ray source populations.

Name	Date	Cycle	#	Exposure (ksec)	$L_{0.3-2}^{\text{faint}}$ (10^{35} erg/s)	N_{src}	$N_{\text{src}}^{\text{soft}}$	$N_{\text{src}}^{\text{SSS}}$	M_* ($10^{10} M_{\odot}$)
(1)	(2)	(3)	(4)	(5)	(6)	(7)	(8)	(9)	(10)
NGC 5236 (M83)	23/12/2010 - 28/12/2011	12	10	729.63	3.0	276	116	14	2.5
NGC 5194 (M51)	09/09/2012 - 10/10/2012	13	7	745.33	5.8	245	105	5	4.1
NGC 5457 (M101)	19/01/2004 - 01/01/2005	5	24	952.01	6.3	221	89	11	2.0
NGC 3031 (M81)	26/05/2005 - 06/07/2005	6	15	175.92	3.5	161	50	2	5.3
NGC 5128 (Cen A)	22/03/2007 - 30/05/2007	8	6	561.72	11.7	286	88	2	3.6
NGC 3115	18/01/2012 - 06/04/2012	13	8	985.40	7.7	136	32	0	6.9
NGC 3379	23/01/2006 - 10/01/2007	7	4	305.53	20.1	87	30	1	5.8
NGC 4278	16/03/2006 - 20/04/2007	7	5	433.30	36.0	244	92	2	6.0
NGC 4697	26/12/2003 - 18/08/2004	5	4	153.70	34.7	102	38	2	6.0

Notes: (1) – Galaxy name. (2) – Time interval of observations. (3) – *Chandra* cycle during which most of observations were made. (4) and (5) – Total number of observations and their exposure time. Full information about archival data used in this work are available in Appendix 2.2. (6) – X-ray luminosity of faintest source detected in combined data. For computing this luminosity, an absorbed black-body model was used with temperature $kT = 60$ eV and absorption column density computed as described in Section 2.4.1. (7) – Total number of detected sources (see Section 2.2.1). (8) – Total number of sources classified as soft according to the method described in Section 4, and having ≥ 20 net counts. (9) – Number of SSSs located to the left of the stable hydrogen burning boundary in Fig.2.5 (see Section 2.5.1 and Appendix A.2). (10) – Stellar mass within the spatial region used for source detection.

2.2.1 Source detection

Source detection was performed with the *wavdetect* tool. We chose to use small $\sqrt{2}$ scale series with a power of 0–3 of the wavelet functions to minimize the spurious detections associated with soft diffuse emission in galaxies. Scales of wavelets correspond to variation of the point spread function (PSF) within an aim point of a single ACIS chip. We setup the following parameters of *wavdetect* to create a background map from the merged image: *bkgthresh*=0.01, *maxiter* = 10, *iterstop* = 10^{-6} . The false-positive source detection probability threshold was chosen at 10^{-7} . Mask filtering was applied to all images of galaxies using exposure maps. Pixels were included in the source-detection region where exposure map values were greater than 20% of the maximum (*expthresh* = 0.2). False-color X-ray images of all galaxies with their D_{25} and source-detection regions are presented in Appendix A.1.

To maximise sensitivity of source detection, we used a combination of the following energy bands: 0.3–1 keV; 1–2 keV; 0.3–2 keV; 0.5–8 keV; 2–8 keV bands. We ran *wavdetect* in each of these bands and merged their results into a single source list, excluding duplications. To this end we used the STILTS package (Taylor 2006), with the match radius equal to the sum of their PSF radii defined at the 80% encircled fraction. In the final merged list, we chose the coordinates of sources in the band where the significance of detection was maximal. In the very inner regions of some galaxies, *wavdetect* found multiple overlapping sources. Visual inspection of the images showed that many of these sources are likely false detections caused by the presence of substructures in the bright and complex diffuse emission of the nucleus. In many cases it appears impossible to separate true compact sources from such false detections. We therefore decided to exclude the central circular region of 15" radius of the M51, M83, and Centaurus A galaxies from our analysis. In the case of Centaurus A we also excluded regions around bright X-ray jets similar to Voss & Gilfanov (2006).

To define source and background count extraction regions, we produced PSF maps. In order to account for PSF variations across the combined image, we created a PSF map for each observation with the *mkpsfmap* tool using encircled energy of 80%, and combined individual maps weighting them with respective exposure maps. Combined source spectra used in the further analysis were extracted using the CIAO tool *specextract*. For source regions we used circles with a radius equal to that of the 80% PSFs fraction from the exposure-weighted PSF map. The background regions were defined as annuli with inner and outer radii equal to two and four times the radius of the PSFs, respectively. The source count rates were corrected for source count leakage to the background region. When source or background regions of different sources overlapped, we excluded the overlapping parts from the counts summation, correcting the PSF fractions accordingly.

The lists of detected sources were analyzed to identify spurious detection due to fluctuations in local background. For each source, we tested the null hypothesis that observed counts in source and background regions are Poissonian realizations of local background with the same mean (Weisskopf et al. 2007, see Appendix A). We estimated probabilities using source and background counts from merged images in the 0.3–2 keV band. All de-

tections with a statistical confidence of less than 3σ were excluded from the final source list. Additionally, inspection of X-ray images by eye did not reveal any potentially spurious detections. In Table 2.2 we summarize the numbers of X-ray sources detected in the galaxies of our sample.

2.2.2 Stellar masses of the final sample of galaxies

Stellar masses of galaxies within D_{25} and within the source-detection regions listed in Tables 5.1 and 2.2 were determined following the prescription of Zhang et al. (2012) as summarized below. We used background-subtracted images from 2MASS Large Galaxy Atlas (Jarrett et al. 2003). Bright sources were visually removed from the images. Net counts of the images S were converted into magnitudes using the zero-point magnitude K_{MAGZP} from the headers of fits files.

$$m_K = K_{MAGZP} - 2.5 \log(S). \quad (2.2)$$

We obtained K_s band absolute magnitudes using the distances listed in Table 5.1. When computing luminosities, solar absolute magnitude in K_s band was assumed to be $K_{s,\odot}=3.27$ (Willmer 2018). The final stellar masses of the galaxies were obtained using the K_s band mass-to-light ratio (Bell & de Jong 2001),

$$\log(M_*/L_K) = -0.692 + 0.652(B - V)_0, \quad (2.3)$$

where L_K is K_s band luminosity and $(B-V)_0$ is the color index corrected for galactic and internal extinction (see Table 5.1).

2.3 Source classification

2.3.1 Method

To classify and separate soft and super-soft sources from sources with more usual spectra we used a combination of hardness ratio HR and median energy \tilde{E} . The hardness ratio was defined as the ratio of the hard band count rate to the total broad band count rate:

$$HR = \frac{R(2 - 8 \text{ keV})}{R(0.3 - 8 \text{ keV})}, \quad (2.4)$$

where R is the background subtracted count rate in the respective energy band. The statistical error of the hardness ratio was calculated using standard error propagation.

The median energy \tilde{E} for each source was calculated from its observed counts spectrum considering the 0.3–8.0 keV energy band. The statistical error was computed using the standard formula for the variance of the sample median (Rider 1960) where the probability density at the median energy was approximately determined from the distribution of observed counts. When computing the median energy, we chose not to subtract background from the source spectrum; the simulations demonstrate that, for the typical source

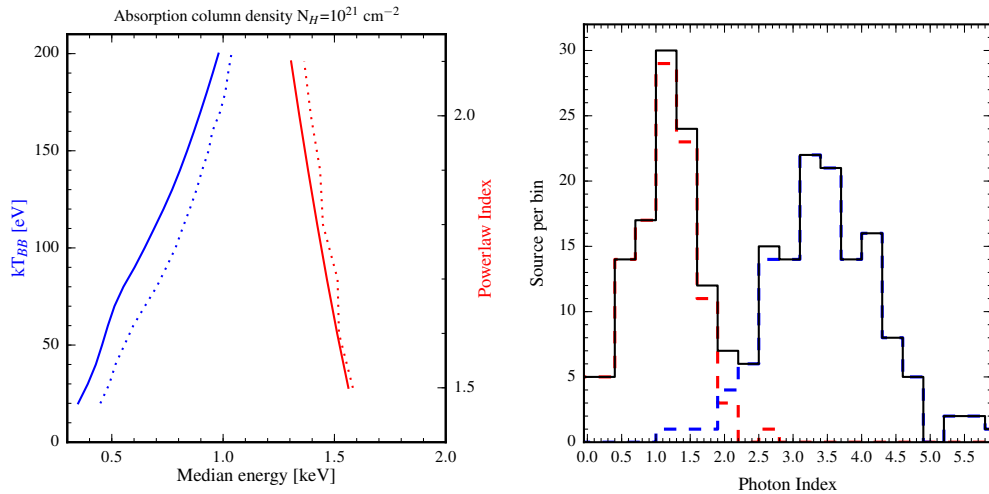


Figure 2.2: *Left*: Relation of the median energy to the temperature of a black-body model (left-hand curves and y-axis, blue in the color version of this plot) and to the photon index of a power-law model (right curves and y-axis, red). Simulations for the Chandra ACIS-S detector with Cycle 13 (2012) response. An absorption column density of 10^{21} cm^{-2} was assumed. *Solid lines* show models without background, *dotted lines* show models with 50% contribution of background counts. Parameter ranges are relevant to super-soft sources and X-ray binaries, and the two types of spectra are clearly separated at about $\tilde{E} \approx 1.0 - 1.3$ keV. *Right*: Verification of the source classification procedure in M51. Distribution of sources with median energy $\tilde{E} \leq 2$ keV over the photon index of the power-law model. *The blue and red dashed histograms* show the distributions of sources classified as soft and hard, respectively, and the *black solid line* indicates the total distribution.

and background spectra we are dealing with, this does not affect our source classification procedure (see Fig. 2.2 and its discussion below).

The motivation behind our choice of the parameters used for source classification is as follows. The median energy characterizes the overall softness of the spectrum. Figure 2.2 (left panel) shows the median energies of the absorbed black-body and power-law models. As one can see from the plot, in the parameter range relevant to nuclear burning, accreting WDs ($kT \lesssim 200$ eV) and X-ray binaries/AGNs/stars ($\Gamma \lesssim 2$), the two types of sources occupy different domains along the \tilde{E} axis with some gap in between⁴. Therefore one may expect a bi-modal distribution of sources over \tilde{E} (which may however be smeared by statistical uncertainties).

We use M51 to illustrate and verify our classification of sources using their median energy (see corresponding panels in Fig. 2.3). To this end we fit the background-subtracted

⁴We note that the particular location of the boundary between super-soft sources and X-ray binaries in Fig. 2.2 depends on the hydrogen column density N_H and details of the instrument response. The curves plotted in Fig. 2.2 (left panel) have been computed for the 2012 (Cycle 13) Chandra ACIS-S response. For other Chandra calibration epochs their shape and location along the x-axis will be (slightly) different.

spectra of all sources with $\tilde{E} \leq 2 \text{ keV}$ ⁵ with an absorbed power-law model. The absorption column density for each source was fixed as described in Section 2.4.1 below. The distributions of soft and hard X-ray sources over photon index are shown in the right panel of Fig. 2.2. From these distributions it is clear that indeed the sources classified as soft and hard occupy different domains along the photon index axis. The small overlap of the two distributions is caused by statistical uncertainties in measuring the median energy and photon index.

This comparison shows that a classification scheme based on the median energy is efficient in identifying sources with soft spectra. The hardness ratio on the other hand characterizes the presence of source emission above 2 keV and helps to identify sources with low \tilde{E} but also featuring hard emission components extending to higher energies. Such hard spectral components are not typical for nuclear burning WDs and may be encountered, for example, in accreting black holes in the soft state and in some supernova remnants.

Finally, we note that the median energy is not efficient in separating the bulk of supernova remnants (SNRs) from WDs. This can be achieved with more detailed spectral fitting, which nevertheless produces meaningful results only for the brightest sources.

Use of the median energy and hardness ratio for characterization of the spectral shape is not entirely new in X-ray astronomy; Hong et al. (2004) for example proposed the use of various quantiles and Prestwich et al. (2003) used a color–color diagram for this purposes. Di Stefano & Kong (2003) used hardness ratio to classify SSSs in external galaxies. Color–color diagrams and hardness ratio techniques were used in numerous other studies not mentioned here. However, to our knowledge, the present study is the first to use the combination of the median energy and hardness ratio for separating super-soft sources from the bulk of the population.

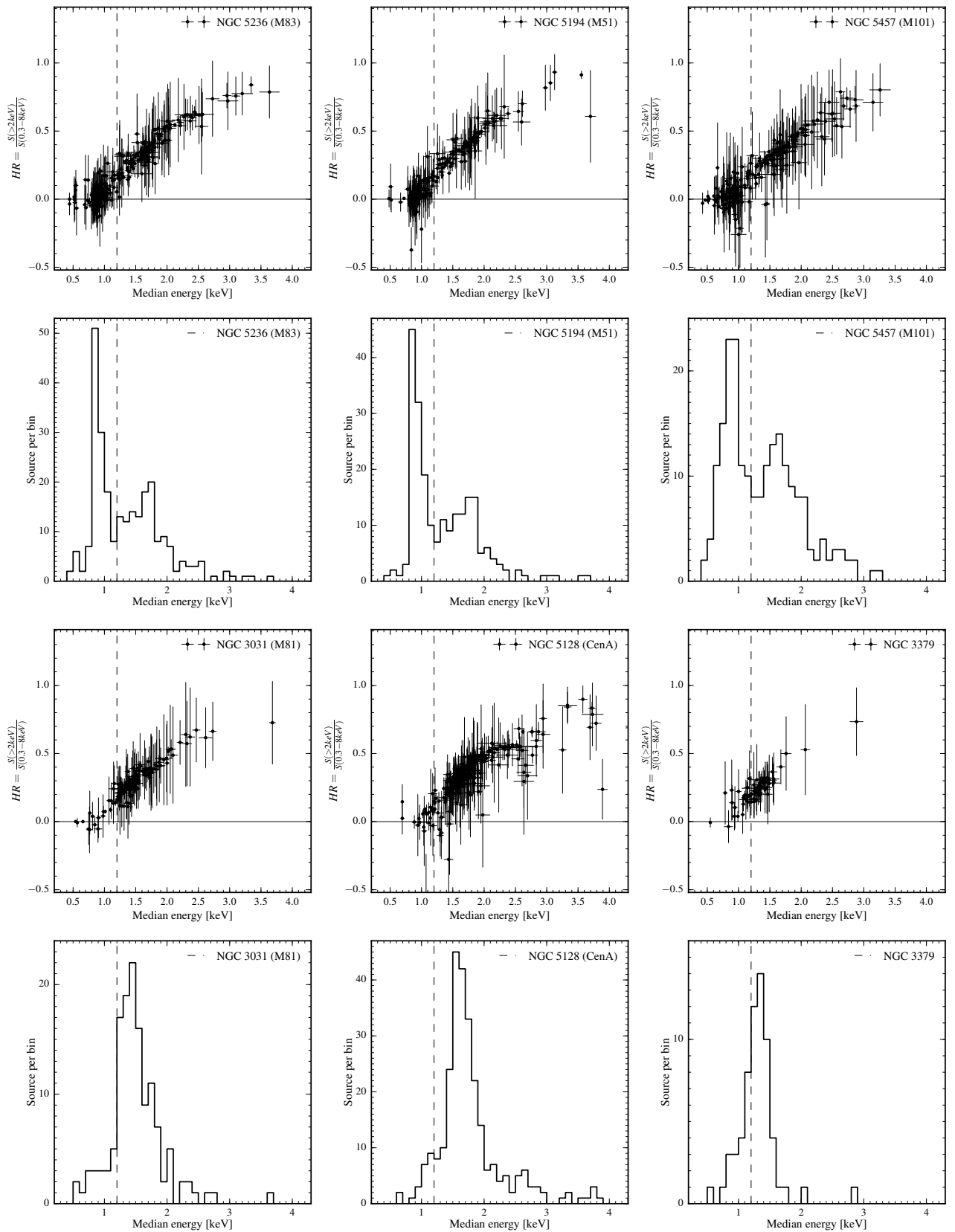
2.3.2 Distribution of sources in $HR - \tilde{E}$ plane

The distribution of sources on the hardness ratio–median energy plane is shown in Fig. 2.3. In producing these plots we applied cuts of 20 net counts to all data sets in order to exclude sources with overly large uncertainties. For each galaxy we also plot distribution of sources over the median energy.

Late-type galaxies

Distributions of the sources over median energy in M51, M83, and M101 are clearly bimodal. Their $HR-\tilde{E}$ diagrams have distinct and relatively compact populations of soft sources at $\tilde{E} \lesssim 1 \text{ keV}$ and $HR \sim 0$ along with the more extended tail of sources with more usual harder spectra. Based on their distributions over the median energy, we chose

⁵Some of the hard sources are located at $\tilde{E} \gtrsim 2 \text{ keV}$, too large for a power-law spectrum with a slope of $\Gamma \lesssim 2$ (Fig. 2.2, left panel). These are either sources with genuinely large \tilde{E} , e.g., absorbed AGNs, or faint sources where the contribution of the instrumental background becomes important and shifts the median energy to unphysically large values.

Figure 2.3: – *continued*

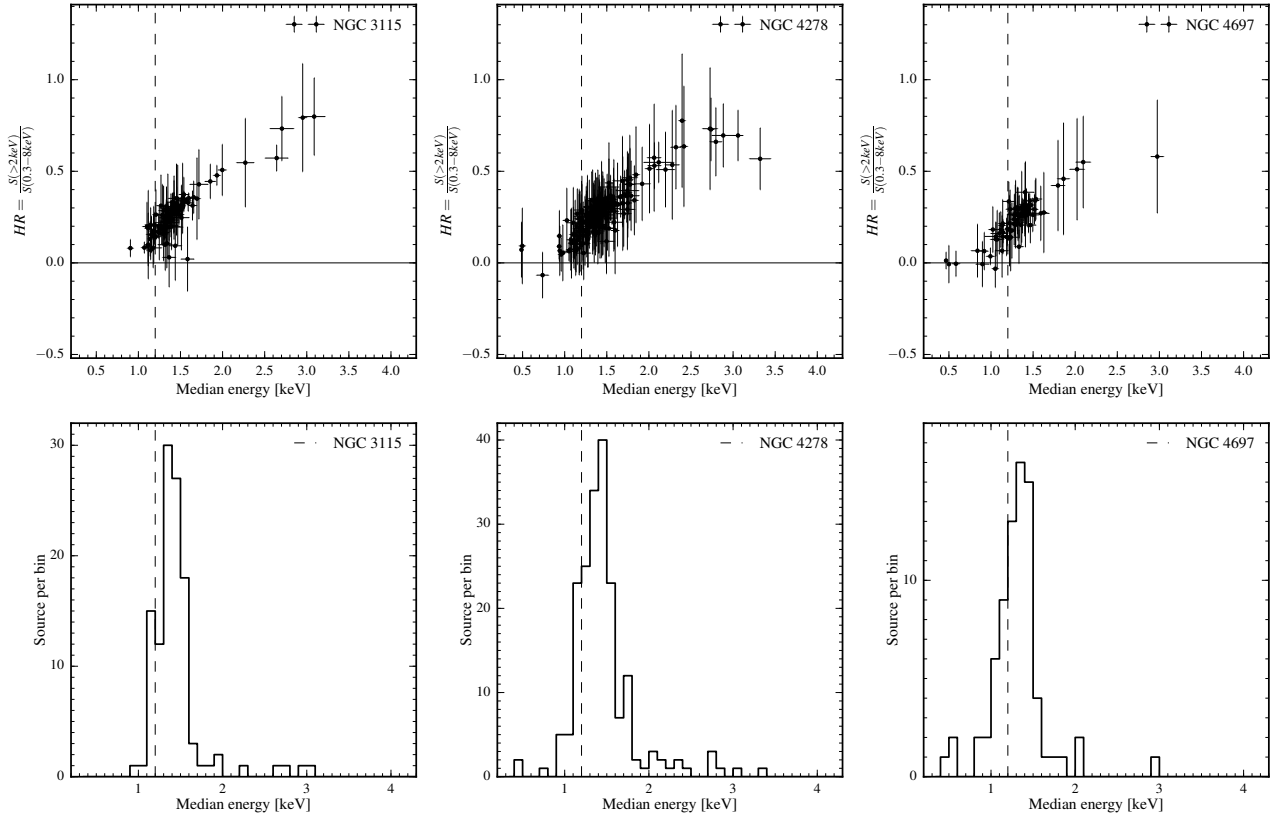


Figure 2.3: Hardness ratio vs. median energy diagram for compact X-ray sources in the galaxies of our sample. Only sources with ≥ 20 net counts are plotted. Dashed lines show the median energy boundary of $\tilde{E}_0 = 1.2$ keV (see Section 2.3.2). The distributions of sources over median energy are plotted below their corresponding median energy–hardness ratio diagram.

the boundary of $\tilde{E}_0 = 1.2$ keV to select soft sources in these galaxies. Hard sources were excluded from further consideration. We also excluded sources with statistically significant flux ($\geq 3\sigma$) detected above 2 keV. The total numbers of thus-selected soft sources are presented in Table 2.2.

The median energy distribution of sources in M81 shows a single peak at $\tilde{E}_0 \approx 1.5$ keV with a possible shoulder towards lower values of \tilde{E} . Lack of bi-modality may be a consequence of the star-formation history of this galaxy as discussed in section 2.5.4. Due to the absence of obvious bi-modality in the source distribution we applied a selection criterion based on the absence of hard flux. In particular, we excluded sources with statistically significant flux ($\geq 3\sigma$) detected above 2 keV from further analysis. Their numbers are listed in Table 2.2 .

Table 2.3: Absorption column densities for late-type galaxies.

Name	$N_{\text{H},f=0.5}$ (10^{21} cm^{-2})	$N_{\text{H},f=1}$ (10^{21} cm^{-2})	Metallicity (Z_{\odot})	References for metallicity
(1)	(2)	(3)	(4)	(5)
NGC 5236 (M83)	3.35	6.35	$\sim 0.5^*$	Bresolin et al. (2009)
NGC 5194 (M51)	1.84	3.51	$\sim 0.7^*$	Moustakas et al. (2010)
NGC 3031 (M81)	1.30	1.53	$\sim 0.7^*$	Stanghellini et al. (2014)
NGC 5457 (M101)	1.67	2.46	1	Assumed for spectral fit

(1) – Galaxy name. (2) and (3) – Median value of N_{H} of soft sources calculated assuming $f = 0.5$ and $f = 1$ (eq.2.5) respectively. (4) – Metallicities of galaxies used in spectral fit and (5) – references for these values. Metallicities marked with an asterisk were recalculated relative to solar abundance $[\text{O}/\text{H}]_{\odot} = 4.9 \times 10^{-4}$ of [Wilms et al. \(2000\)](#).

Early-type galaxies

The distribution of sources over median energy for elliptical and lenticular galaxies is also unimodal with the low-energy shoulder present for some galaxies. As for M81, we only kept sources without statistically significant flux above 2 keV.

2.4 Observed properties of soft sources

2.4.1 Equivalent hydrogen column density

Because of the softness of sources under consideration, the value of equivalent hydrogen column density N_{H} is important for accurate spectral analysis. This problem is of relevance for late-type galaxies.

Because of the degeneracy with other parameters N_{H} is difficult to determine from fitting X-ray spectra, especially for fainter sources with a smaller number of counts, which constitute the majority of our sample. Therefore, we chose to fix N_{H} at values determined in the radio band. To this end, we combined CO 2-1 and 21 cm maps from the HI Nearby Galaxy Survey (THINGS, [Walter et al. 2008](#)) and the HERA CO-Line Extragalactic Survey (HERACLES, [Leroy et al. 2009](#)). For each source we computed absorption column density as

$$N_{\text{H}} = N_{\text{H,Gal}} + f \times (N_{\text{HI}} + 2 \times N_{\text{H}_2}), \quad (2.5)$$

where $N_{\text{H,Gal}}$ is the Galactic hydrogen column density in the direction of galaxy ([HI4PI Collaboration et al. 2016](#)), and N_{HI} and N_{H_2} are column densities of neutral and molecular gas from THINGS and HERACLES surveys respectively, computed as follows:

$$N_{\text{HI}}[\text{cm}^{-2}] = \frac{1.11 \times 10^{24} \times I_{\text{HI}}}{\text{FWHM}_{\text{maj}}[\text{''}] \times \text{FWHM}_{\text{min}}[\text{''}]}, \quad (2.6)$$

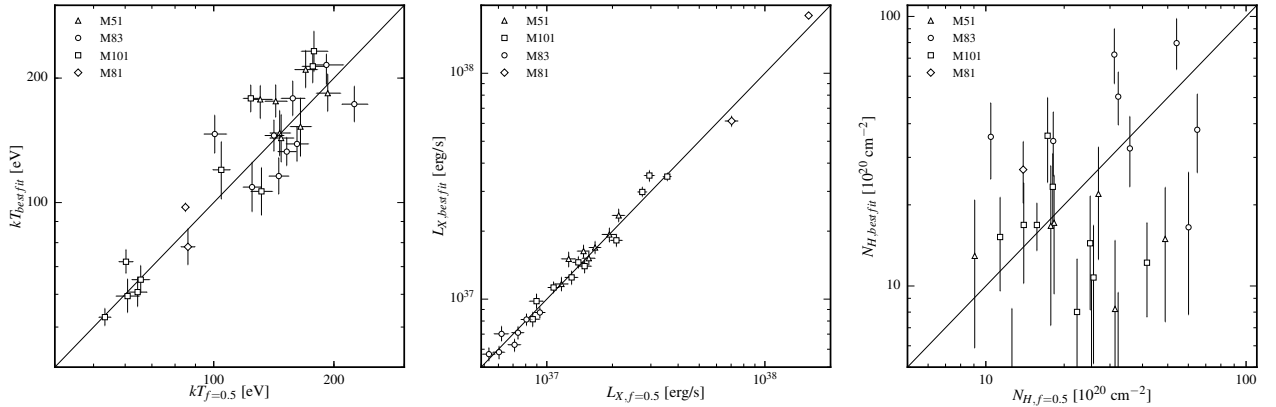


Figure 2.4: Relations between black-body temperature (left) and absorbed X-ray luminosity (center) values computed with N_{H} being a free parameter of X-ray spectral fit (y-axes) and for N_{H} computed from Eq.2.5 with $f = 0.5$ (x-axes). The right-hand panel shows the relation between best-fit N_{H} and N_{H} computed from Eq.2.5. Only sources with net counts ≥ 200 are shown. Errors are 1σ . See Section 2.4.1 for more details.

where I_{HI} is the velocity-integrated intensities of THINGS maps in units of $\text{Jy beam}^{-1} \text{ km s}^{-1}$, and FWHM_{maj} and FWHM_{min} are the major and minor axes of the beam in arcsec (Walter et al. 2008, see Eq. 5). For N_{H_2} we used:

$$N_{\text{H}_2}[\text{cm}^{-2}] = \frac{R_{21}}{0.8} \times X_{\text{CO}} \times W_{\text{CO}}, \quad (2.7)$$

where W_{CO} is the HERACLES velocity-integrated CO $J = 2 \rightarrow 1$ map intensity in units of K km s^{-1} , X_{CO} is the CO $J = 1 \rightarrow 0$ to H_2 conversion factor, and R_{21} is the ratio of CO $J = 2 \rightarrow 1$ to CO $J = 1 \rightarrow 0$. We assumed the Galactic value of $X_{\text{CO}} = 2 \times 10^{20} \text{ cm}^{-2} (\text{K km s}^{-1})^{-1}$ (Strong & Mattox 1996; Dame et al. 2001) for the majority of galaxies and $R_{21}=0.8$ (see Leroy et al. 2009, Eq.3 and references therein).

The X_{CO} factor is known to vary between galaxies. In particular, for M51 it is ~ 4 times smaller than the Galactic value (Garcia-Burillo et al. 1993; Guelin et al. 1995). For M81, no CO maps of sufficient quality are available and we accounted only for absorption by neutral hydrogen. For M83 we used the CO 1–0 intensity map from NED⁶ where the galaxy was observed by Crosthwaite et al. (2002) with NRAO 12m telescope.

Table 2.3 shows the median values of absorption column density N_{H} of soft sources in late-type galaxies for two cases: $f = 0.5$ and $f = 1$. We adopted $f = 0.5$, which means that sources are subjected to half of the absorption intrinsic to the galaxy. Naively, this corresponds to the assumption that all sources are located close to the midplane of the host galaxy.

⁶NASA/IPAC Extragalactic Database: <https://ned.ipac.caltech.edu>

We analyzed the spectra of bright sources with ≥ 200 net counts and compared the results of X-ray spectral fits with fixed N_H with those where N_H was a free parameter of the fit. The results are shown in Fig. 2.4. As one can see, although there is considerable scatter in N_H , values of temperature and especially X-ray luminosity are in reasonable overall agreement. Unfortunately, such an analysis is only possible for a small fraction of the sources. We therefore chose to use fixed absorption column density, computed for each source from Eq. 2.5.

Elliptical and lenticular galaxies in our sample have much lower intrinsic neutral hydrogen column density, below $\sim \text{few} \times 10^{19} \text{ cm}^{-2}$ (Serra et al. 2012). We can therefore safely assume $N_H = N_{H,\text{Gal}}$ for early-type galaxies in our sample, with a caveat regarding Centaurus A. In the dust lanes of this galaxy, absorption column density is at the nearly constant level of $\approx 5 \times 10^{21} \text{ cm}^{-2}$ and drops rather sharply outside the dust lanes (Struve et al. 2010). Therefore, we accounted for the intrinsic absorption for the sources located in the dust lanes (about one-third of all soft sources in Centaurus A) in the same way as for spiral galaxies, but assuming a constant value of intrinsic absorption of $5 \times 10^{21} \text{ cm}^{-2}$, while we used the Galactic value for the sources outside dust lanes. We find that the particular details of this calculation are unimportant. It should also be noted that Centaurus A also stands out in the early-type galaxy sample because of its ongoing star formation at a level of $\sim 0.8 M_\odot/\text{yr}$ (Espada et al. 2019). It will be further discussed in Section 2.5.2.

2.4.2 X-ray spectral analysis and $kT_{bb} - L_X$ diagram

The spectra of X-ray sources classified as soft were approximated with an absorbed black body model, with the absorption column density fixed at the values computed as described in Section 2.4.1. For spectra with a small number of counts, the absorption correction of X-ray luminosity often bears a large uncertainty and may lead to physically meaningless values. We therefore chose to use the absorbed X-ray luminosities of sources for further analysis and apply absorption to models when comparing them to the data. We used the Tuebingen-Boulder ISM absorption model (Wilms et al. 2000) (*tbvarabs* model in XSPEC). Abundances of late-type galaxies were fixed at values listed in Table 2.3. For early-type galaxies Wilms et al. (2000) solar elemental abundance was assumed. The spectral fit was performed with XSPEC (Arnaud 1996) in the 0.3–8 keV energy band using C – statistics (Cash 1979). The background spectrum was included in the spectral fitting. Spectra were binned to have at least one count per bin, following the recommendations of the XSPEC manual⁷. Confidence intervals for the parameters were obtained using the *error* command in XSPEC.

The distribution of sources on the X-ray luminosity–temperature (hereafter $kT_{bb} - L_X$) plane is shown in Fig. 2.5. When plotting the $kT_{bb} - L_X$ diagram, we applied a cut of 20 net counts in order to exclude faint sources with overly large error bars. X-ray luminosities were computed for the 0.3–2 keV energy band. The thin solid line near the bottom of each panel shows X-ray luminosity corresponding to 20 net counts, as a function

⁷<https://heasarc.gsfc.nasa.gov/xanadu/xspec/manual/XSappendixStatistics.html>

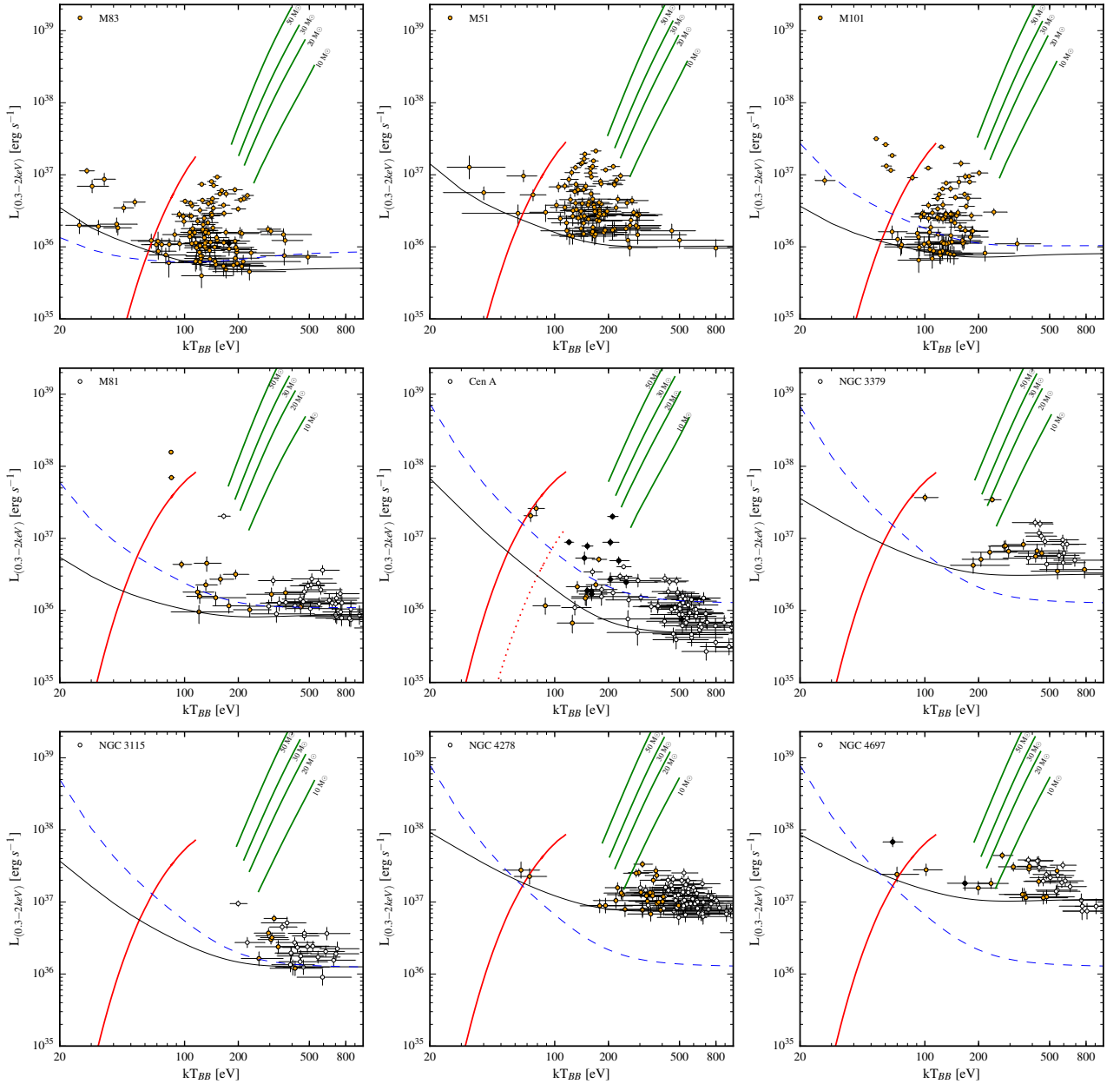


Figure 2.5: $kT_{\text{bb}} - L_X$ diagram for soft X-ray sources in the galaxies of our sample. A cut of 20 net counts was applied. The luminosities are in the 0.3 – 2.0 keV band and are not corrected for absorption. All plotted sources have no statistically significant flux above 2 keV (*open circles*). Sources with median energy $\tilde{E} \leq 1.2$ keV are shown with *solid orange circles*. Sources with Gaia matches of measured parallax or proper motion are marked by *black diamonds*. *Solid red curves* show $kT_{\text{bb}} - L_X$ relations at the lower boundary of stable nuclear burning. Along these curves, the WD mass increases from $0.51M_{\odot}$ at the lower left end to $1.34M_{\odot}$ at the upper right end. The dotted red line for Centaurus A shows the location of this boundary in the dust lanes of this galaxy. *Green lines* correspond to the emission spectrum of the general relativistic accretion disk model around a Schwarzschild BH (Ebisawa et al. 1991) for BH masses of 10, 20, 30, and $50M_{\odot}$. The accretion rate changes along the curves from $0.02\dot{M}_{\text{Edd}}$ to $1\dot{M}_{\text{Edd}}$. Horizontally oriented *solid black* curves show the luminosity corresponding to 20 net counts. The *dashed blue line* on each plot shows the 20 counts luminosity limit for M51 corrected for the difference in absorption column density between M51 and the galaxy under consideration. All model curves show absorbed luminosities. Errors are at 1σ confidence. See Section 2.4.2 for details of calculations.

of black-body temperature. In plotting these curves we converted counts to rate using the maximal exposure time of the observation. The absorbed X-ray luminosity was computed using a count rate–flux conversion for the black-body spectrum with the given temperature and absorption column density. The luminosity corresponding to 20 counts exceeds the luminosities of faintest sources by a factor of about three, and therefore samples of sources above these curves should not be subject to significant incompleteness effects.⁸

On each panel, the blue dashed line shows the luminosity limit for M51 data corrected for the difference between absorption column densities in M51 and the galaxy under consideration. The correction factor is close to unity at temperatures exceeding a few hundred eV, but may be considerable at low temperatures for soft spectra. These lines allow us to compare sensitivities of different datasets independently of absorption. In particular, this comparison demonstrates that despite the rather significant scatter in Chandra exposure and distances to galaxies, the selected galaxies have comparable detection sensitivity to sources with soft spectra.

In Fig. 2.5, solid red curves show the lower bound of the stability strip for the nuclear burning of hydrogen on the WD surface (Wolf et al. 2013). In plotting these curves, we used the Stefan-Boltzmann law to compute the effective temperature and the mass–radius relation for zero-temperature WDs from Panei et al. (2000). The WD mass changes along the curve from $0.51M_{\odot}$ to $1.34M_{\odot}$. We then used the black-body model in XSPEC, applied ISM absorption, and computed the 0.3–2 keV band luminosity corresponding to the given WD mass and effective temperature. For late-type galaxies, absorption column densities were fixed at corresponding median values from Table 2.3 while for early-type galaxies we used the Galactic value $N_{\text{H,Gal}}$, as explained above. For Centaurus A we also show the location of this boundary for sources located in the dust lanes. Green lines in Fig. 2.5 show the tracks of the spectral model of the relativistic accretion disk around a Schwarzschild black hole (BH) (Ebisawa et al. 1991). Along these lines, the mass accretion rate changes from $0.02\dot{M}_{\text{Edd}}$ to $1\dot{M}_{\text{Edd}}$, and different lines correspond to the different black hole mass as marked by the number near the curves. To compute these tracks, we approximated the accretion disk emission spectrum using an absorbed black-body model. The absorption was applied similar to other models plotted in the figure.

All sources plotted in Fig. 2.5 have no significant ($\geq 3\sigma$) flux above 2 keV. For three late-type galaxies with bi-modal median energy distributions (M83, M51 and M101) we plot only sources with median energy $\tilde{E} \lesssim 1.2$ keV. These sources show rather compact distributions in the $kT_{\text{bb}} - L_{\text{X}}$ plane with temperatures of 20~300 eV and X-ray luminosities in the range of $10^{36} \sim 10^{38}$ ergs/s. For other galaxies, we only used the criterion of lack of statistically significant ($\geq 3\sigma$) emission above 2 keV. For these galaxies, distributions of sources extend significantly towards higher temperatures (cross-hair symbols in Fig. 2.5), which is not surprising as such a selection includes many sources with regular spectra. These sources are dominated by X-ray binaries and background AGNs and their discussion

⁸See, e.g., incompleteness function of Chandra data for Centaurus A in Voss & Gilfanov (2006). From their Fig A1, incompleteness effects become relatively small at luminosities of about two to three times the detection limit of the data.

is beyond the scope of this paper. Sources with low median energy $\tilde{E} \lesssim 1.2$ keV (solid orange symbols) tend to have lower temperatures than the majority of the sources in these galaxies and are discussed in the following section, along with soft sources in M83, M51, and M101.

2.4.3 Foreground stars

To identify foreground stars we cross-correlated the lists of soft X-ray sources with the GAIA (Gaia Collaboration et al. 2016) catalog, Data Release 2 (Gaia Collaboration et al. 2018). With the search radii of $2''$ we typically found two matches per galaxy except for Centaurus A where we found 12 matches. The large number of matches for Centaurus A is caused by its relative proximity to the Galactic plane. Some of the GAIA matches have statistically significant measurements of parallax or proper motion, with $S/N > 3$. These sources are classified as stars in the Galaxy and are excluded from further analysis; we mark them with open diamonds in Fig. 2.5.

2.5 Nature of soft and super-soft X-ray sources

Based on the first Chandra studies of nearby galaxies, Di Stefano & Kong (2003, 2004) proposed that soft sources in external galaxies could be divided into super-soft and quasi-soft. The former are characterized by color temperatures of $kT \lesssim 100$ eV and are believed to be mostly associated with accreting WDs with nuclear burning of hydrogen on their surface, while the latter have temperatures in the range $kT \sim 100 - 300$ eV and are possibly unrelated to WDs.

2.5.1 Super-soft X-ray sources and accreting WDs

In the commonly used albeit (over)simplified picture, it is assumed that the spectral energy distribution of nuclear burning WDs can be roughly described by a black-body spectrum (cf. Woods & Gilfanov 2013) with a color temperature close to the effective temperature. Observations of well-known SSSs in the Milky Way, Magellanic Clouds (e.g., Greiner 1996; Kahabka & Trumper 1996) seem to broadly support this assumption. The effective temperature of an accreting WD powered by nuclear burning of hydrogen on its surface is calculated by Eq. 1.21. Numerical calculations show that at the bottom of the stability strip, $R_{\text{phot}} \sim R_{\text{WD}}$ and the photospheric radius increases with increasing \dot{M} (Wolf et al. 2013).

The red solid line in Fig. 2.5 shows the temperature–luminosity relation computed at the lower bound of the stability strip and assuming $R_{\text{phot}} = R_{\text{WD}}$. For the definition of the lower boundary of stable nuclear burning (dependent on WD mass) we used the results of Wolf et al. (2013), and for the WD radius we used zero temperature radius (also dependent on WD mass) from Panei et al. (2000). The region on the $kT_{bb} - L_X$ diagram above and to the left of this line is permitted for accreting WDs stably burning hydrogen on their surface,

while in the part of the diagram to the bottom-right, stable nuclear burning of hydrogen is not possible and this region should be populated with other types of soft X-ray sources. Indeed, Fig.2.5 shows that in late-type galaxies (M83, M51, M101 and M81), there is a distinct group of rare soft and luminous sources located above these line. These sources have temperatures of approximately several tens of eV and seem to clearly stand out in the populations of soft sources in these galaxies. When interpreting the results shown in Fig.2.5, one should bear in mind that it shows absorbed luminosities in the 0.3 – 2.0 keV band and that absorption and bolometric corrections increase roughly exponentially with decreasing color temperature, and therefore the softest sources are truly luminous.

For this reason, we classify sources to the left of the red line in Fig.2.5 as classical SSSs. We also include those sources that are located outside the stable nuclear burning boundary but whose error bars cross this boundary. In addition, we added to this list two sources in M101 that are located outside but close to the stable nuclear burning boundary (the two sources in the upper right panel of Fig.2.5 with $kT \gtrsim 100$ eV and $L_X \gtrsim 10^{37}$ erg/s.). The catalog of SSSs is presented in Table A.2, and their numbers in galaxies from our sample are listed in Table 2.2.

2.5.2 Specific frequency of super-soft X-ray sources across morphological types

From Fig.2.5, it is evident that SSSs are considerably more abundant in late-type galaxies than in early-type galaxies. However, for a statistically sound conclusion one needs to take into consideration the completeness limits of the various data sets. To this end we used the sensitivity limit for M51 corrected for the difference in the absorption column density as described in Section 2.4.2 to select SSSs. In each galaxy, we selected sources to the left of the thick red line and above the dashed blue line in Fig. 2.5. This selection is within the 20 counts flux limit (solid black line in Fig. 2.5.) in all galaxies, except for M83 where at the low temperature end the 20 counts limit for this galaxy is higher by a factor of about two. This may result in slight underestimation of the specific frequency of super-soft sources in late-type galaxies. In Centaurus A, we used different criteria for sources located in and outside the dust lanes (c.f. dotted line in Fig. 2.5), although this does not change the final result.

In order to estimate specific frequencies of SSSs, we group the data separately for early- and late-type galaxies. There are 29 super-soft sources in late-type galaxies (M83, M51, M81, M101), which, for the total stellar mass of $13.9 \times 10^{10} M_\odot$ yield the specific frequency of

$$f_{\text{SSS}}^{\text{S}} \approx (2.08 \pm 0.46) \times 10^{-10} M_\odot^{-1}. \quad (2.8)$$

In computing statistical errors we used Gehrels approximation (Gehrels 1986). Counting lenticular and elliptical galaxies together (Centaurus A, NGC3115, NGC3379, NGC4278, NGC4697), we find seven SSSs for the total stellar mass of $28.3 \times 10^{10} M_\odot$, yielding a specific frequency of

$$f_{\text{SSS}}^{\text{E+S0}} \approx (2.47 \pm 1.34) \times 10^{-11} M_\odot^{-1}. \quad (2.9)$$

Centaurus A galaxy, although classified as S0, shows some star-formation activity within its dust lanes, at the level of $\sim 0.8 M_{\odot}/\text{yr}$ (Espada et al. 2019). However, its SSS specific frequency is closer to early-type galaxies than to late-type galaxies. In order to check how its inclusion in our sample affects our results, we compute the SSS specific frequency for elliptical galaxies only:

$$f_{\text{SSS}}^{\text{E}} \approx (2.02 \pm 1.38) \times 10^{-11} M_{\odot}^{-1}. \quad (2.10)$$

This number is $\sim 20\%$ smaller but compatible with the value obtained including Centaurus A. The lower limit for the SSS specific frequency in early-type galaxies at the 3σ confidence level is $f_{\text{SSS}}^{\text{E}} > 8.2 \times 10^{-12} M_{\odot}^{-1}$. The ratio of specific frequencies of SSS in late-type to early-type galaxies is

$$f_{\text{SSS}}^{\text{E+S0}} / f_{\text{SSS}}^{\text{S}} = 0.12 \pm 0.05, \quad (2.11)$$

which means that late-type galaxies contain about eight times more SSSs than early-type galaxies. Using a Bayesian approach, we estimate that their specific frequencies are different at the confidence level corresponding to about $\approx 5.8\sigma$.

We searched for variations of the SSS specific frequency between galaxies of the same morphological type. To this end, we compared observed numbers of SSSs in each galaxy with their expected values computed from the corresponding SSS specific frequency and stellar mass of the galaxy. For early-type galaxies, we find no statistically significant deviations of observed numbers of SSSs from their expected values. This is not surprising, given the small numbers of SSSs in early-type galaxies. However, for the late-type galaxies, we observe statistically significant deviations in M83 and M81 where the observed numbers of super-soft sources differ from the expected values at the statistically significant levels exceeding $\sim 3\sigma$. This can be understood considering that populations of accreting nuclear burning WDs are determined by the long-term star-formation history of their host galaxy rather than by its mass, as discussed in the following section.

For late-type galaxies, we also compute the SSS specific frequency per unit of star formation rate. Using SFR values collected from the literature (Table 5.1 and references there) we obtain:

$$f_{\text{SSS}}^{\text{S}} \approx (3.13 \pm 0.70) (M_{\odot}/\text{yr})^{-1}. \quad (2.12)$$

Overall, the numbers of SSSs in late-type galaxies appear to somewhat better correlate with their star-formation rate than with stellar mass.

2.5.3 Comparison with previous work and discussion

The fact that SSSs tend to be predominantly associated with young stellar populations has been noted previously (e.g., Di Stefano & Kong 2004). Studying populations of soft sources in nearby galaxies, Di Stefano (2010) mentioned the difference in the numbers of soft sources in early- and late-type galaxies, but they did not quantify these trends. Using a sample of 12 nearby late-type galaxies, Bogdán & Gilfanov (2011) concluded that specific

frequencies (per unit K-band luminosity) of luminous ($L_X > 10^{36}$ erg/s) super-soft sources in disks of spiral galaxies exceed those of bulges by factor of approximately two. Taking into account the fact that the typical M_*/L_K ratio for bulges is approximately twice that found for disks, this translates to a factor four difference in specific frequency per unit mass, which is qualitatively the same trend as that seen in our comparison of late-type and early-type galaxies, although the particular numbers are different. The above difference is due to the fact that [Bogdán & Gilfanov \(2011\)](#) used a selection procedure to identify SSSs based on the hardness ratio with the threshold, corresponding to $kT=200$ eV.

Population synthesis calculations of nuclear burning, accreting WDs predict a difference in specific frequencies of SSSs in spiral and elliptical galaxies ([Chen et al. 2015](#)). Using their model `a025qc17`, we estimate specific frequencies of SSSs with X-ray luminosities exceeding 10^{36} erg/s. For spiral galaxies, these latter authors obtained specific frequencies ranging from 4×10^{-10} to 2×10^{-9} sources per M_\odot , corresponding to absorption column densities of 3×10^{21} cm $^{-2}$ and 3×10^{20} cm $^{-2}$. For elliptical galaxies, they obtained $\approx 6 \times 10^{-11}$ sources per M_\odot (for column density 3×10^{20} cm $^{-2}$), which is approximately seven times that found for late-type galaxies. The contrast between late- and early-type galaxies is highly consistent with our observations, especially taking into account the dependence of these numbers on the age of the host galaxy ([Chen et al. 2015](#)). However, the actual numbers of specific frequencies are larger in simulations than in our data by at least a factor of between about two and three. Among other possibilities, this could be understood as a result of the approximate account for absorption, as the numbers of observable SSSs are highly sensitive to the column density.

Another interesting result of this work is that within the morphological types, the number of SSSs does not seem to obey simple scaling relations with parameters of the host galaxy. In particular, there are large and statistically significant excursions in the specific frequency of SSSs in spiral galaxies normalised to their stellar mass. This could be expected in view of the results of the WD population modeling, which predict that the population of super-soft sources peaks at about 1 Gyr after the star formation event ([Chen et al. 2015](#)). For this reason, numbers of super-soft sources in galaxies should not be expected to scale with stellar mass or current star-formation rate. In a more general context, the low specific frequency of SSSs, especially in early-type galaxies, supports the earlier conclusion that they are not the major class of type Ia supernova progenitors ([Di Stefano 2010](#); [Gilfanov & Bogdán 2010](#); [Johansson et al. 2014](#); [Woods & Gilfanov 2014](#)).

2.5.4 Other soft X-ray sources

Along with rare SSSs, in all galaxies from our sample there are much more abundant populations of soft sources with somewhat harder —but still relatively soft— spectra located to the right of the stable nuclear burning boundary in [Fig. 2.5](#). These sources were previously classified as quasi-soft X-ray sources ([Di Stefano & Kong 2004](#); [Orio 2006](#)). Among other hypotheses, it was proposed that they are associated with SNRs or with accreting BHs in the soft spectral state (e.g., [Di Stefano & Kong 2004](#); [Patel et al. 2013](#); [Long et al. 2014](#); [Kuntz et al. 2016](#)), although the contribution of the latter should be minimal (Section

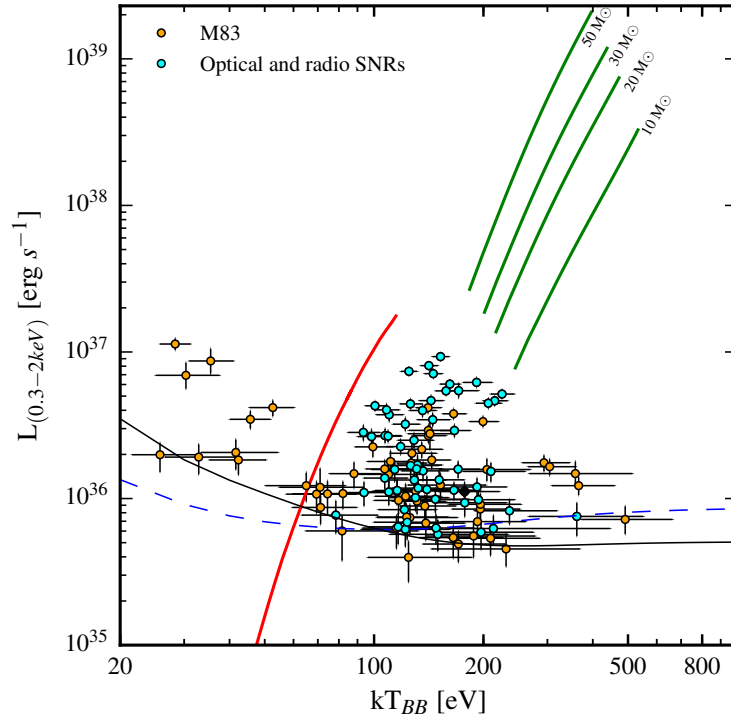


Figure 2.6: $kT_{\text{bb}} - L_X$ for soft X-ray sources in M83. Supernova remnants confirmed by optical and radio data are shown by cyan circles. See Fig. 2.5 for a detailed description of the $kT_{\text{bb}} - L_X$ diagram.

2.4.2)

The X-ray-emitting SNRs will be largely unresolved by Chandra and appear as point sources. Indeed, the SNR emission shifts outside the X-ray band when the shock slows down to about ~ 200 km/sec and the post-shock temperature drops below $\sim 10^6$ K (Vink 2017). This happens about $\sim 2 \times 10^4$ years after the explosion when the remnant size typically reaches $\sim 10 - 20$ pc (Blondin et al. 1998). At the distances of spiral galaxies of $3.6 \sim 7.6$ Mpc, the linear dimensions of $10 - 20$ pc correspond to the angular sizes of $\sim 0.4 - 0.9''$, which can barely be resolved with Chandra ACIS for the brightest sources. Furthermore, the majority of SNRs will be classified as soft sources according to their hardness ratio and median energy.

We used M83 as a test case to clarify the nature of soft sources located to the right of the stable nuclear burning boundary. This galaxy has one of the best studied X-ray SNR populations. Long et al. (2014) identified 87 X-ray detected SNR candidates based on their X-ray spectral properties and associations with optical emission nebulae and/or radio sources. From this sample, the SNR nature of 67 sources was confirmed with optical spectroscopy using the [SII]/ $H\alpha$ line ratio (Winkler et al. 2017). The list of 87 X-ray-detected SNRs from Long et al. (2014) was cross-correlated with our catalog of X-ray sources detected in M83. With $1''$ matching radius, we found 66 matches, of which 6

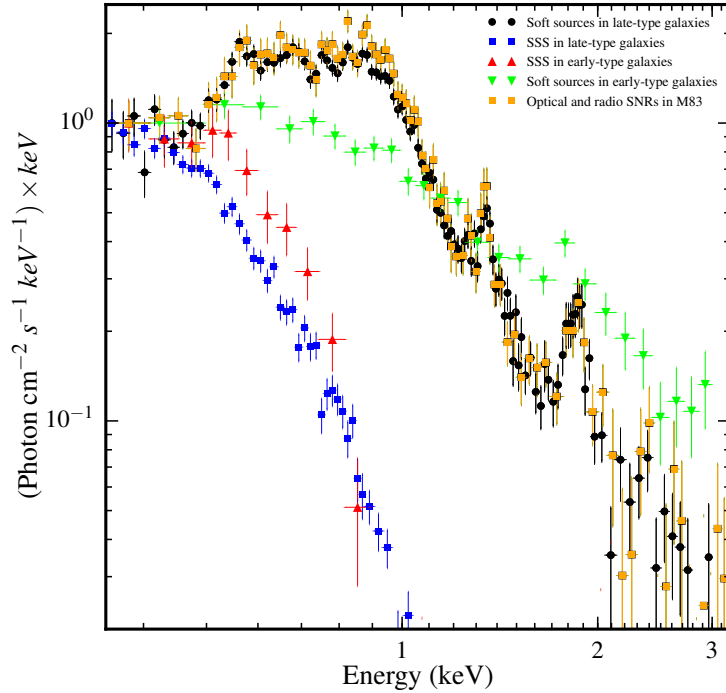


Figure 2.7: Combined spectra of soft and SSSs in late- and early-type galaxies. *Black and green symbols* show the integrated spectrum of all soft sources located outside the stable nuclear burning region for WDs (i.e., located to the right of the thick red line in Fig.2.5) in late- and early-type galaxies. *Yellow symbols* show integrated spectrum of sources matching confirmed SNRs in M83. *Blue and red symbols* show the integrated spectra of SSSs, i.e., sources located to the left of and above the stable nuclear burning boundary in late- and early-type galaxies, respectively. The spectra are normalized to the same flux at 0.35 keV. See Section 2.5.1 for more details.

sources have statistically significant emission beyond 2 keV and the remaining 60 sources were classified as soft sources in our analysis. We replot the $kT_{\text{bb}} - L_X$ diagram for M83 in Fig. 2.6 marking confirmed SNRs by cyan symbols. As one can see, all confirmed SNRs are located outside the stable hydrogen nuclear burning boundary on the $kT_{\text{bb}} - L_X$ diagram (i.e., to the right of the thick red line in Fig. 2.6) and their distribution on the $kT_{\text{bb}} - L_X$ plane is morphologically quite similar to the distribution of the majority of the quasi-soft sources. We therefore conclude that the majority of the quasi-soft sources must be SNRs.

For many of the brightest quasi-soft sources in spiral galaxies, the likelihood values obtained from spectral fitting suggest that the spectrum is more complicated than predicted by a featureless black-body model. A more detailed investigation of several such sources revealed that these deviations are mostly associated with the presence of emission lines in their spectra. In the majority of cases, the spectrum of thermal emission of optically thin plasma or a nonequilibrium ionization model significantly improved the quality of the

fit, suggesting that these sources may be SNRs. However, such a detailed analysis is only possible for a handful of brightest sources.

In order to compare spectral properties of soft and super-soft sources, we combined their spectra in late- and early-type galaxies. Combined spectra are shown in Fig. 2.7 separately for sources located inside and outside the stable hydrogen nuclear burning boundary on the $kT_{bb} - L_X$ diagram (see Section 2.4.2). For comparison, we also show the combined spectrum of confirmed SNRs in M83. As seen in Fig. 2.7, the combined spectrum of soft sources in spiral galaxies shows strong Mg and S lines and closely matches the combined spectrum of SNRs in M83. Similar values of the equivalent width of Mg and S lines support our conclusion that the vast majority of soft sources in these galaxies must be SNRs. In early-type galaxies on the other hand, the combined spectrum of soft sources is harder and does not show strong emission lines. As discussed in Section 2.4.2, because of the chosen method of selection, soft sources in early-type galaxies should include large numbers of X-ray binaries and background AGNs. On the other hand, SSSs in all galaxies have much softer spectra, as expected. Their spectra are broadly similar in late- and early-type galaxies, although the quality of the latter prevents a more quantitative conclusion.

We finally note that the numbers and specific frequencies of soft sources in galaxies from our sample seem to follow the same trend as that found for super-soft sources, decreasing from late- to early-type galaxies. However, a detailed investigation of the dependence of the specific frequency of SNRs on morphological type would require a more accurate selection of sources and is outside the scope of the present thesis.

Chapter 3

X-ray observations of historical classical nova counterparts with eROSITA telescope aboard SRG orbital observatory during the all-sky survey

The contents of this chapter is based on the work originally published as Galiullin & Gilfanov (2021b) Astronomy Letters 47, p. 587–606

3.1 Sample of Historical Classical Novae in the Galaxy

To study the X-ray emission from CN counterparts in quiescence, we collected a sample of known historical CNe in our Galaxy that were classified and confirmed based on their optical light curves and spectra. The list of known CNe compiled by the Central Bureau for Astronomical Telegrams¹ was taken as a basis. This list includes the CNe discovered from 1612 to 2010. We added the CNe detected from 2010 to 2021 from the publicly accessible lists of Koji Mukai² and Bill Gray³ to this list. We selected only those counterparts that are located in the half of the sky for the processing of which the Russian SRG/eROSITA consortium is responsible into the final CN sample.

The resulting sample of CNe in our Galaxy produced in this way includes 309 sources

¹http://www.cbat.eps.harvard.edu/nova_list.html

²<https://asd.gsfc.nasa.gov/Koji.Mukai/novae/novae.html>

³<https://projectpluto.com/galnovae/galnovae.htm>

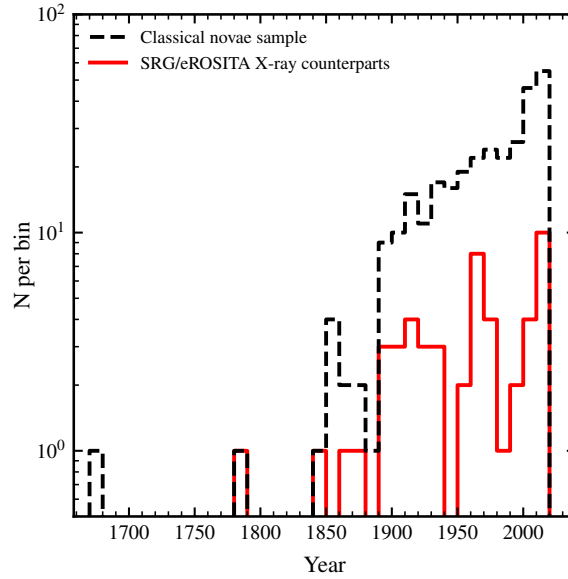


Figure 3.1: Distribution of Galactic CNe in the half of the sky being processed by the Russian SRG/eROSITA consortium in years of their detection: the dashed (black) line indicates the complete CN sample; the solid (red) line indicates the CHs having cross-matches with X-ray sources from the SRG/eROSITA catalog within $15''$.

with Galactic longitudes $0^\circ \leq l \leq 180^\circ$ discovered from 1670 to 2021. The distribution of CNe in years of their detection is presented in Fig. 3.1. As can be seen from the figure, most of the events were detected after 1850.

3.2 SRG/eROSITA Telescope Data

In this chapter, we use the data from three sky surveys obtained by the SRG/eROSITA telescope from December 2019 to June 2021. The eROSITA data were preprocessed and calibrated at the Space Research Institute of the Russian Academy of Sciences by the eROSITA data processing system developed and maintained by the X-ray catalog science working group of the Russian eROSITA consortium using some elements of the eSASS (eROSITA Science Analysis Software) package developed at the Max Planck Institute for Extraterrestrial physics. In the data processing, we used the results of ground-based preflight calibrations and flight calibration observations in October–November 2019 and during 2020–2021. The data from the three sky surveys were combined to increase the sensitivity.

The X-ray catalog of sources was cross-correlated with the list of known CNe in the Galaxy with a search radius of $15''$. At such a search radius we found 52 matches. At the same time, the expected number of chance matches is ~ 0.75 , i.e., fairly small. The final list of X-ray sources having identifications with CNe is presented in Table B.2. The CN

distances and color excesses were taken from various papers the references to which are given in the table. We determined the distances for some of the CNe using the measured parallaxes from the second data release of the Gaia catalog of sources (Gaia Collaboration et al. 2016, 2018). To cross-match the CN list and the Gaia catalog, we used a search radius of $1''$. The Gaia data were used only for three sources for which the proper motions and/or parallaxes were measured with a statistical significance $\gtrsim 3\sigma$.

When extracting the spectra and light curves, a circle with a radius of $60''$ was used as the source region, and an annulus with inner and outer radii of $120''$ and $240''$, respectively, was used as the background region. X-ray spectra were analyzed using XSPEC v.12 software (Arnaud 1996). The spectrum was approximated using the C -statistics (Cash 1979). In this case, the spectral channels were grouped in such a way as to include at least three counts per channel⁴.

To test the quality of the fit to the data by the spectral model, we used Monte Carlo simulations. In particular, we used the realization of such simulations provided in the XSPEC package by the *goodness* command with the Anderson–Darling (AD) statistical test⁵. The test using the *goodness* command allows the percentage of the simulations with the AD statistic greater than the actual value obtained when fitting the observed source spectrum by the chosen model to be calculated. For each source and each spectral model, we produced 10^5 realizations with the *nosim* and *fit* parameters. In each realization, the spectrum was drawn according to the Poisson statistic using the best-fit model parameters and then was fitted by the same model to determine the best value of the AD statistic. The distribution of the derived values of the AD statistic was used to estimate the probability to obtain a value of the statistic exceeding the observed one as a result of statistical fluctuations. To compare the fits to the same data by different spectral models, we used the Akaike information criterion (AIC) (Akaike 1974) calculated as $AIC = 2 \times k + C$, where k is the number of free parameters in the fit, and C is the value of C -statistics for the best-fit parameters. The preferred model for fitting the observed spectrum is the one with the minimum value of AIC .

⁴see note for work in XSPEC:
<https://heasarc.gsfc.nasa.gov/xanadu/xspec/manual/XSappendixStatistics.html>

⁵see Appendix B in XSPEC manual

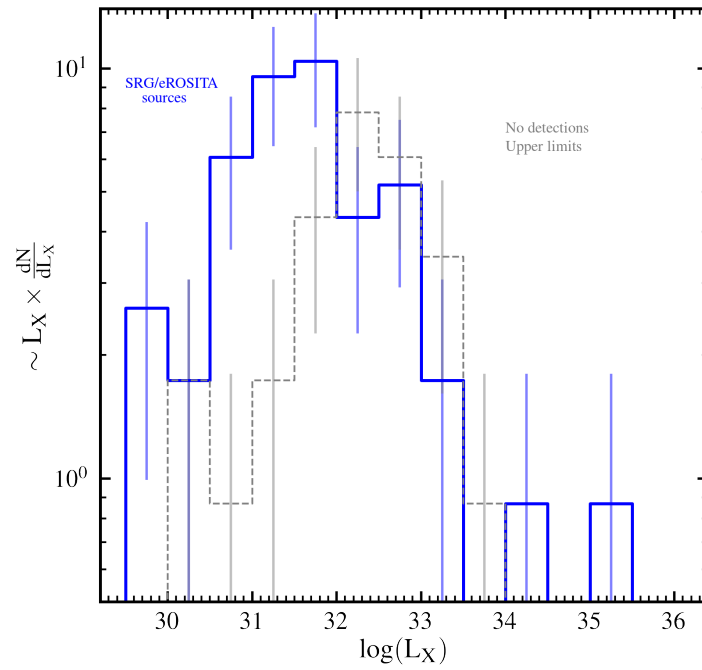


Figure 3.2: Distribution of CN counterparts in observed X-ray 0.3–2.3 keV luminosity from the data of the three SRG/eROSITA sky surveys (blue color). The gray histogram indicates the distribution of 3σ upper limits on the X-ray luminosities of the CN counterparts that were not detected based on the data of the three sky surveys for which the distances are known. The X-ray luminosity was corrected for interstellar absorption. The observed distributions uncorrected for the sample incompleteness effects are shown.

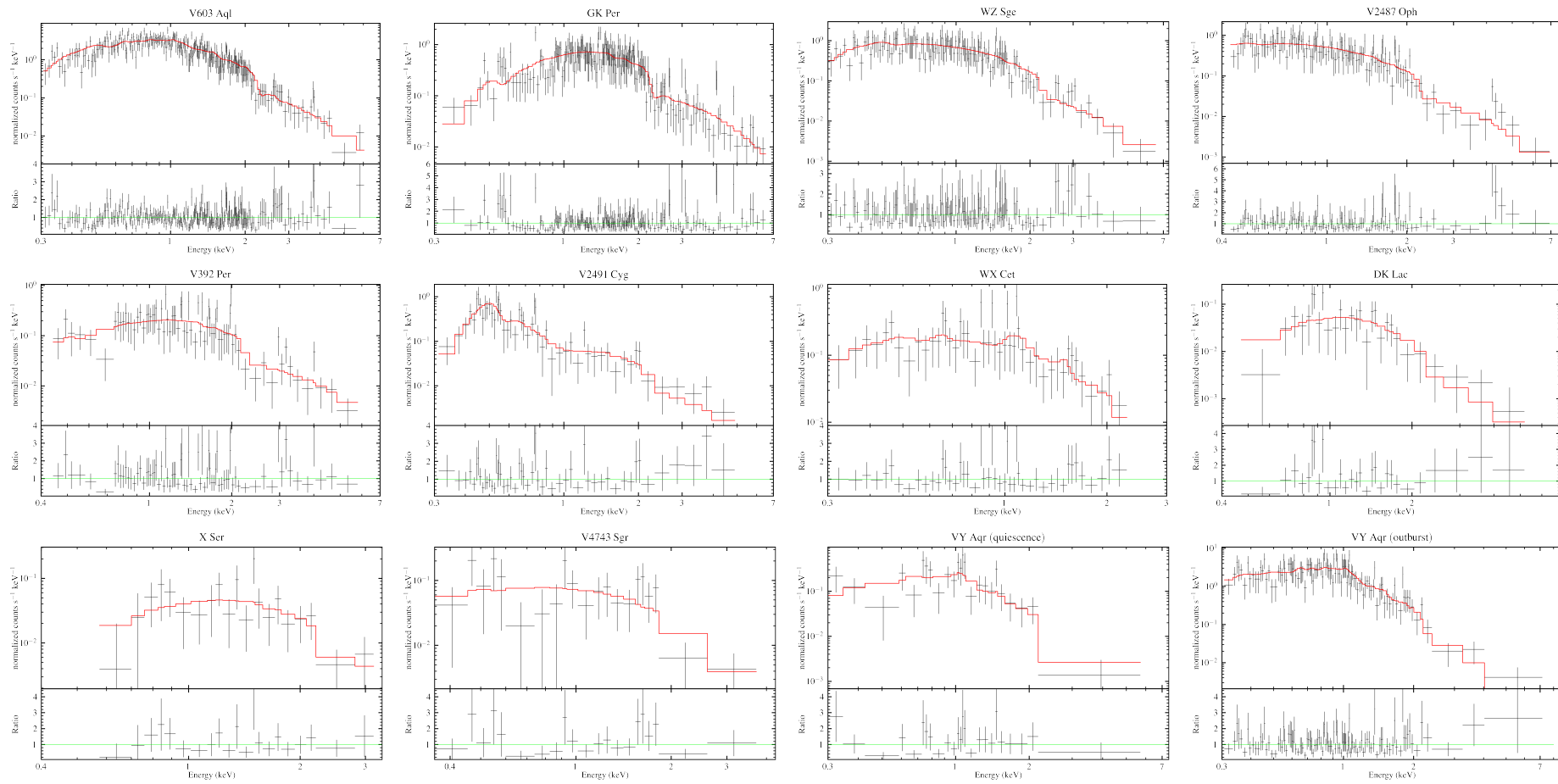


Figure 3.3: X-ray spectra of bright sources, where SRG/eROSITA detected more than 50 counts. The best-fit model selected by the Akaike Information Criterion (AIC) from Table B.1, presented in red. The smaller bottom panel in each spectrum shows the ratio of the observed counts to the model spectra.

3.3 X-ray Emission from the Counterparts of Classical Novae in Quiescence

3.3.1 Spectral Analysis of Bright Sources

For 11 sources from our sample, the SRG/eROSITA telescope recorded more than 50 counts, which is enough for a spectral analysis. Their spectra are shown in Fig. 3.3, while their fits by various spectral models are given in Table B.1. To take into account the interstellar absorption, we used the Tubingen-Boulder ISM absorption model (*tbabs* model in XSPEC, Wilms et al. 2000) under the assumption of solar elemental abundances in the interstellar medium.

The spectra of the bright sources exhibit some dichotomy between the sources with hard spectra, $\Gamma \sim 1$, and the sources with soft spectra, $\Gamma \sim 2 - 3$, which is discussed in more detail in this and succeeding sections. We found no obvious correlation of the spectral shape with the source luminosity or with the time elapsed since the CN outburst.

The spectra of several sources have a more complex shape than the simple power-law model or the optically thin plasma model. Therefore, we also used the isobaric cooling flow model *mkcflow*⁶ in XSPEC (Mushotzky & Szymkowiak 1988) to describe the observed spectra. This model describes successfully the X-ray spectra of dwarf novae in quiescence (see, e.g., Mukai et al. 2003; Baskill et al. 2005; Pandel et al. 2005; Mukai et al. 2009; Wada et al. 2017). The minimum and maximum plasma temperatures were free parameters in spectral fitting. If the best-fit value of the minimum plasma temperature is made coincident with zero, then this parameter will be fixed at 8 eV. For a number of sources from our sample, in particular, for V603 Aql, V2487 Oph, V2491 Cyg, and VY Aqr, the *mkcflow* model provides a better fit to the observed X-ray spectra than does the simple power-law model or, in some cases, the single-temperature optically thin thermal plasma model. At the same time, for the sources with hard spectra GK Per, V392 Per, X Ser, and V4743 Sgr, for which the power-law fit gives a photon index $\Gamma \sim 1$, the isobaric cooling flow model is clearly inapplicable and leads to unreasonably high temperatures $\gtrsim 100$ keV unrealizable on the WD surface. For these sources, we do not provide the parameters of the fit by the *mkcflow* model.

The spectrum of V2491 Cyg defies a satisfactory description by any of the simple single-component models considered above. This source has a comparatively soft spectrum, but the optically thin single temperature plasma model does not describe the emission from the source. Adding another component, black-body radiation, to the model improves significantly the quality of the spectral fit, making it acceptable. In the case of such a two-component model, the data do not limit the temperature of the optically thin thermal component from above and, therefore, it was fixed at 10 keV. The nature of the super-soft component in the spectrum of V2491 Cyg is discussed below.

⁶Note that when using the *mkcflow* model, it is necessary to set the redshift parameter $z > 0$, since the model was originally created to describe X-ray emission from a cluster of galaxies. We calculated the redshifts from the distances given in Table B.2 and the Hubble constant $H_0 = 69.3$ km/(Mpc s).

The spectrum of V2487 Oph also defies description by the spectrum of an optically thin thermal plasma, but the isobaric cooling flow model provides a satisfactory quality of the fit to the data. However, just as in the case of V2491 Cyg, the possible presence of a super-soft component in the spectrum of V2487 Oph was noted in previous studies (see, e.g., [Hernanz & Sala 2002](#)). Therefore, we fitted the spectrum of this source by a two-component model including black-body radiation and achieved a significant improvement in the quality of the fit to the data compared to the simple single-temperature thermal model. The parameters, the temperature and luminosity of the soft component $kT \approx 100$ eV and $\log(L_X) \approx 36.3$, are comparable to those for V2491 Cyg. However, a comparison of the C-statistic and the Akaike information criterion shows that the *mkcflow* model is sufficient to fit the source spectrum, and the introduction of a second component is not required. Thus, the question of whether a super-soft component is present in the spectrum of V2487 Oph remains open. For other sources from our sample, adding a super-soft thermal component does not improve the quality of the spectral fit.

In the spectra of some sources, in particular, V603 Aql, V2487 Oph, and V392 Per, the spectral features that can be interpreted as emission or absorption lines engage our attention. In the case of V603 Aql and V2487 Oph, these features located at energies ≈ 3.8 and ≈ 4.3 keV do not correspond to emission lines of any cosmically abundant elements. Taking into account the degrees of freedom associated with the positions of these lines and their widths, their statistical significance is low, and they do not require a separate discussion. In the case of V392 Per, the absorption line is located at an energy $\approx 0.68 \pm 0.02$ keV, which is close to the resonance OVII and OVIII lines. Assuming that the position of the line is fixed, its statistical significance is $\approx 2 - 2.5\sigma$ for one studied spectrum. Taking into account the number of studied spectra, this is quite a moderate significance and, therefore, we do not consider this as a reliable detection. Note that no absorption lines of ionized oxygen have been observed previously in the spectrum of V392 Per.

3.3.2 Average Spectrum of Faint Sources

We constructed the average spectrum of the sources from which fewer than 50 counts were recorded and whose signal-to-noise ratio was not enough for a detailed individual study. The averaged spectrum of these sources is shown in [Fig. 3.4](#). Fitting the spectrum by a power law gives the best-fit parameters $\Gamma = 0.96_{-0.17}^{+0.18}$ and $N_H = 9.9_{-3.4}^{+3.8} \times 10^{20} \text{ cm}^{-2}$. As expected, based on the spectral hardness, fitting the spectrum by the optically thin plasma model does not allow an upper limit for the plasma temperature to be obtained. The lower limit on the temperature is ≈ 43 keV. We also divided the faint sources into two groups: the sources from which from 25 to 50 counts were recorded (12 sources) and the sources with fewer than 25 counts (25 sources). The average spectra for both groups have parameters compatible, within the error limits, with those given above.

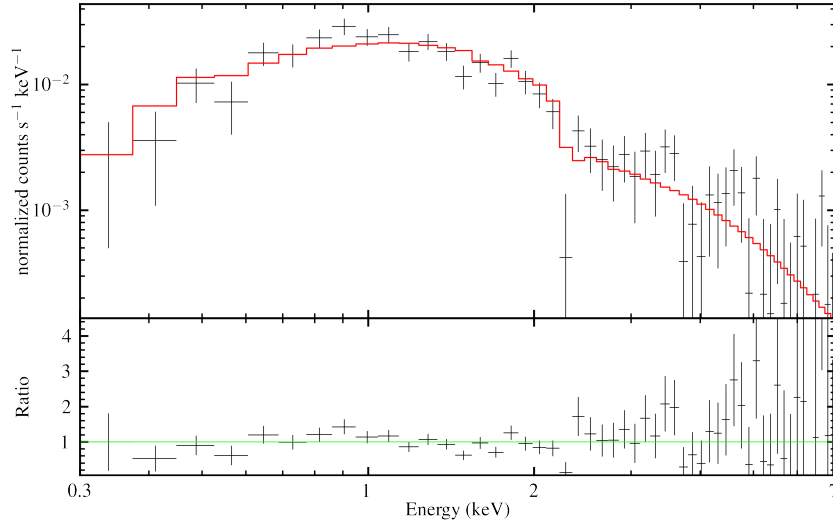


Figure 3.4: Combined X-ray spectrum of the sources with fewer than 50 counts. The model of a power-law slope is represented by the red color. Lower panel: the ratio of the observed counts to the model ones in each energy channel.

3.3.3 X-ray Luminosities

To calculate the X-ray luminosities of the sources from which, on average, more than 50 counts are recorded, we used the model with the minimum value of AIC, corresponding to the best-fit model. For the fainter sources, we used the spectral model constructed by fitting the average spectrum of the faint sources presented above.

We calculated the hydrogen column density for each source individually based on measurements of the color excess $E(B - V)$. To convert the color excess to the extinction A_V , we assumed $R_V \approx 3.1$ (Cardelli et al. 1989), while we used the standard formula $N_H \approx 2.21 \times 10^{21} \times A_V$ (Güver & Özel 2009) to calculate the column density. For those sources where the color excess $E(B - V)$ was not known, we used the total hydrogen column density in the Galaxy toward the source derived from HI4PI data (HI4PI Collaboration et al. 2016). Since the typical spectra of CN counterparts are fairly hard (except for several sources discussed in the next section), the part of the bolometric correction associated with the correction of the X-ray luminosity for low-frequency absorption is small. Therefore, some uncertainty in N_H for the sources with an unknown color excess does not affect strongly our results. Some uncertainty in the spectral shape of the faint sources does not affect the accuracy of their X-ray luminosity estimates either. For example, variations in the slope of the expected power-law spectrum in the range 0.9–2.7 lead to a variation in the counts-to-physical fluxes conversion factor by $\pm 15\%$.

The distances are known for 41 of the 52 sources, which allows their luminosities to be calculated. For the remaining 11 sources, we estimated their luminosities using the median distance of the sources with known distances, which turned out to be 1.5 kpc. Thus,

we derived the distribution of the detected sources in their X-ray 0.3–2.3 keV luminosity corrected for absorption. The derived distribution is shown in Fig. 3.2. The remaining 257 historical CNe from our sample were not detected in the data of the three SRG/eROSITA sky surveys. For 31 of these sources, we determined the distances based on the Gaia catalog and constructed the observed distribution of 3σ upper limits on their X-ray luminosities (see Fig. 3.2).

3.4 Outburst of the Dwarf Nova VY Aqr

In November 2020, an outburst of the dwarf nova VY Aqr occurred, which reached its maximum light on November 8, 2020, $\approx 9.6^m$ in the visual band (Waagen 2020). By chance coincidence, the source was scanned on this day by the SRG/eROSITA telescope during the second sky survey, which allowed its behavior in X-rays to be studied at the maximum of the optical light curve. During the first (May 6, 2020) and third (May 9, 2021) sky surveys, the source was in quiescence.

The SRG/eROSITA data allow the X-ray spectrum of VY Aqr during the dwarf nova outburst to be analyzed for the first time. To study the spectrum in quiescence, we combined the spectra of the first and third sky surveys to increase the statistics. The spectral fits by various models are given in the last two columns of Table B.1.

The power-law model slope and the optically thin plasma temperature show that during the dwarf nova outburst the source spectrum becomes softer, whereas its luminosity increases by a factor of ≈ 10 . The characteristic temperatures in the isobaric cooling flow model in outburst decrease by a factor of ≈ 2 . During a dwarf nova outburst, an increase in the accretion rate gives rise to an optically thick boundary layer, which leads to an apparent “softening” of the X-ray spectrum (e.g., Pringle 1977; Patterson & Raymond 1985b). Note that in November 2007 VY Aqr was observed by the Suzaku observatory in quiescence (Wada et al. 2017). To fit the spectra, Wada et al. (2017) also used the cooling flow model to obtain a maximum temperature $kT_{max} \approx 18.4$ and an accretion rate $\dot{M}_{acc} \approx 7 \times 10^{-13} M_{\odot}/\text{yr}$, close to our values.

3.5 Candidates for Super-Soft X-ray Source among the SRG/eROSITA Sample of CN Counterparts

Among the CN X-ray counterparts, we searched for candidates for super-soft sources whose X-ray emission is associated with the post-nova super-soft X-ray phase. For this purpose, we fitted the spectra of all sources by a black-body model with absorption (*tbabs* × *bbodyrad* model in XSPEC). The hydrogen column density was fixed at the value determined from the color excess $E(B - V)$, as described above.

Most of the sources in our sample have rather hard X-ray spectra and are not described by the black-body model. The approximation of such spectra by this model leads to high temperatures $\gtrsim 200$ eV and low X-ray luminosities $L_X \approx 10^{30} \sim 10^{34}$ erg/s, which are

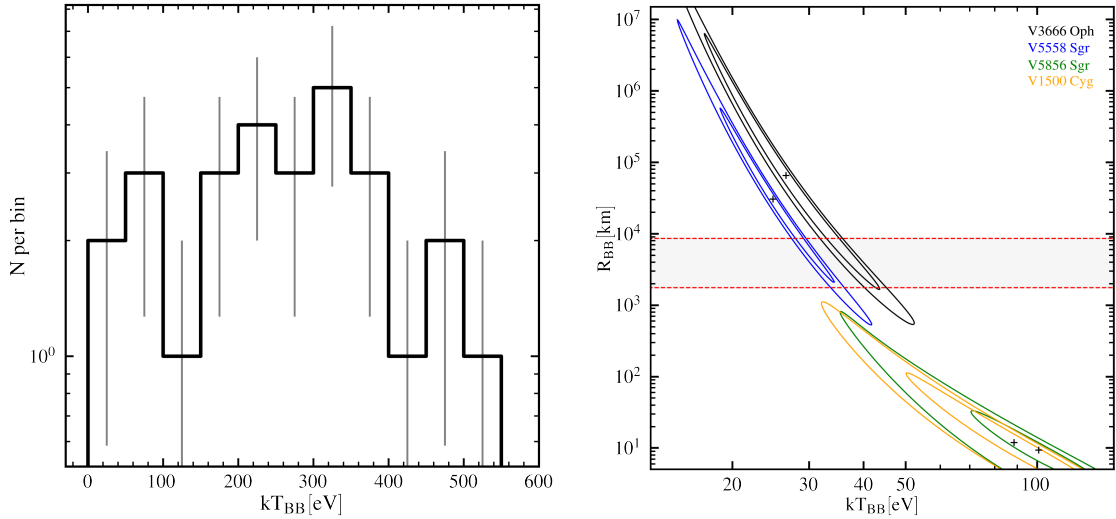


Figure 3.5: (a) Black-body temperature distribution of the CN counterparts. The sources with the temperatures ≥ 600 eV are not included. The candidates for super-soft X-ray sources were preselected by temperature ≤ 200 eV. (b): The contours of the 68% and 95% confidence intervals for the radius and temperature of the black-body model. The red lines shows the WD radii for $0.6 M_{\odot}$ and $1.4 M_{\odot}$, obtained from the mass–radius relation for zero-temperature WDs from [Panei et al. \(2000\)](#).

inconsistent with the values expected during the post-nova phase. However, this procedure makes it possible to select sources with soft spectra for further investigation. The temperature distribution of sources is shown in Fig. 3.5a, where we have excluded sources with temperature $\gtrsim 600$ eV.

For further investigation, we selected nine sources with temperatures ≤ 200 eV. Five of them had a statistically significant ($\geq 3\sigma$) flux above 1.0 keV and, after visual inspection, they were excluded from the sample of super-soft source candidates. As a result, out of 52 CNe sources, we selected four potential super-soft X-ray sources candidates (see their spectra in Fig. 3.6). The Fig. 3.5b shows the confidence interval contours for the radius and temperature of black-body model. We also shows the range of WD radii for the masses of $0.6 M_{\odot}$ and $1.4 M_{\odot}$ from the mass-radius relation for zero-temperature WDs ([Panei et al. 2000](#)). Below we discuss these four super-soft source candidates in more detail.

SRGe J174224.2-205309 (V3666 Oph). The approximation of the source spectrum by a black-body model at a fixed column density $N_H \approx 6.6 \times 10^{21} \text{ cm}^{-2}$ gives a temperature of $kT \approx 27 \pm 10$ eV and the C -statistics 6.86 for seven degrees of freedom. The observed X-ray luminosity in the 0.3–2.3 keV energy band is $L_{X,\text{obs}} = 1.5 \pm 0.5 \times 10^{31} \text{ erg/s}$. Due to the low temperature and the relatively high hydrogen column density, the bolometric correction of the luminosity is $\sim 10^6$ and the bolometric luminosity (the radius of the emitting surface) is highly uncertain: $L_{\text{bol}} \approx 2.1_{-2.0}^{+25.7} \times 10^{37} \text{ erg/s}$. Since the distance to the source was unknown, a median distance of 1.5 kpc was used to estimate the luminosity. The

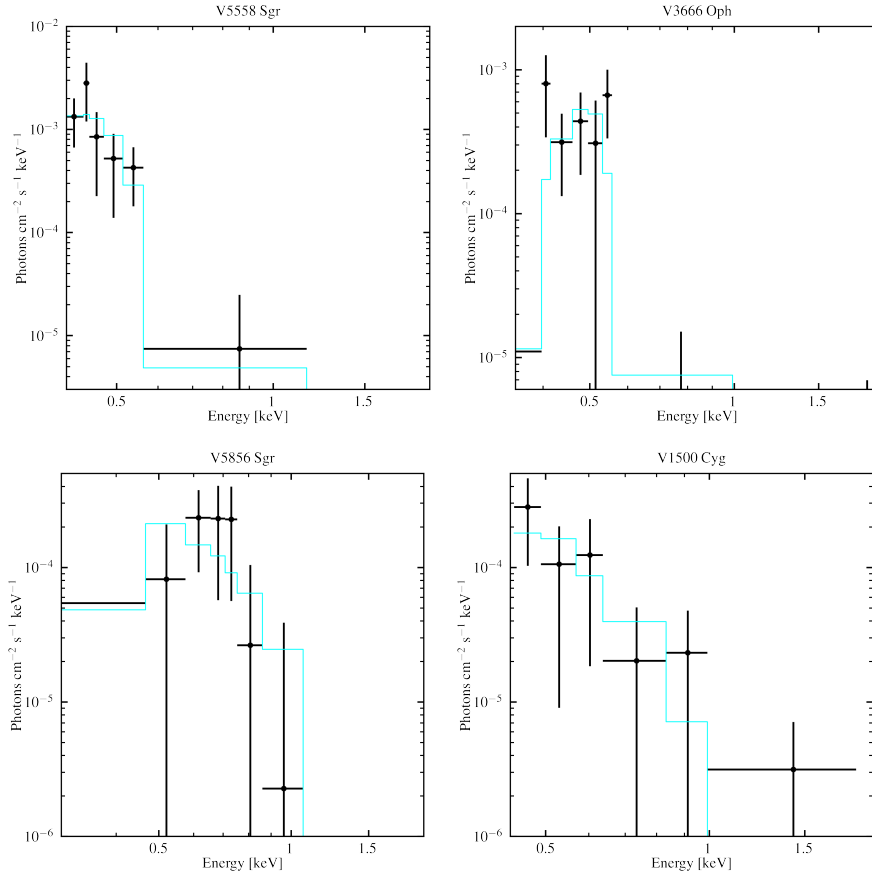


Figure 3.6: Spectra of potential candidates for super-soft X-ray sources among the CNe sample obtained with SRG/eROSITA. The black-body models are shown in blue in each panel.

confidence interval for the radius of the emitting surface of the black-body model overlaps with the WD region; therefore, the X-ray emission from the source can be associated with the post-nova phase. super-soft X-ray emission from the source is detected ≈ 1.6 years after the CN outburst.

SRGe J181018.2-184653 (V5558 Sgr). Similarly, the approximation of source spectrum by the black-body model at a fixed column density $N_H \approx 5.5 \times 10^{21} \text{ cm}^{-2}$ gives a temperature of $kT \approx 25_{-7}^{+10} \text{ eV}$ (the C -statistic value is 2.8 for five degrees of freedom). The observed X-ray luminosity in the 0.3–2.3 keV energy band is $L_{X,\text{obs}} = 2.8 \pm 0.6 \times 10^{31} \text{ erg/s}$, and the bolometric luminosity is $L_{\text{bol}} \approx 1.8_{-1.7}^{+28.8} \times 10^{37} \text{ erg/s}$. The confidence region for the radius and temperature of the black-body model includes the range of WD radii, therefore, the X-ray emission from the source might be associated with the post-nova phase. The super-soft X-ray emission from the source is detected after ≈ 13 years of the CN outburst.

SRGe J182052.9-282218 (V5856 Sgr). Similar to other two sources, we approx-

imated the spectra of this source with a black-body model with a fixed column density $N_H \approx 2.3 \times 10^{21} \text{ cm}^{-2}$, and get a temperature of $kT \approx 101_{-28}^{+51} \text{ eV}$ (the C -statistic value is 3.1 for five degrees of freedom). The observed X-ray luminosity is $L_{X,\text{obs}} = 2.9 \pm 0.6 \times 10^{32} \text{ erg/s}$ in 0.3–2.3 keV energy band, and the bolometric luminosity is $L_{\text{bol}} \approx 1.1_{-0.8}^{+3.6} \times 10^{33} \text{ erg/s}$. The confidence region for the radius and temperature in the black-body model does not overlap with the range of WD radii, therefore, the X-ray emission from the source is unlikely to be associated with post-nova phase. The super-soft X-ray emission from the source is detected after ≈ 3.4 years the CN outburst.

We also note, that the parameters for the soft X-ray emission from V5856 Sgr are almost identical to those obtained for V1500 Cyg polar (see Fig. 3.5b). However, this is not enough to classify V5856 Sgr as a polar. This hypothesis deserves a more detailed study in the course of future observations.

SRGe J211136.5+480905 (V1500 Cyg). V1500 Cyg is a well-known polar in our Galaxy that shows a multicomponent X-ray spectrum. The soft component is described by a black-body model with a temperature of $kT \approx 60 \text{ eV}$, while the hard component is described by bremsstrahlung model with a temperature of $kT_{br} \approx 40 \text{ keV}$ (e.g., Harrison & Campbell 2016). Due to relatively short exposure time during the sky survey, the hard component is not detected in its spectrum, and V1500 Cyg is observed by SRG/eROSITA as a super-soft X-ray source.

For this source the black-body model approximation at a fixed column density, $N_H \approx 3.1 \times 10^{21} \text{ cm}^{-2}$, gives a temperature of $kT \approx 88_{-35}^{+36} \text{ eV}$ (the C -statistic value is 2.5 for six degrees of freedom). The observed X-ray luminosity is $L_{X,\text{obs}} = 2.9 \pm 0.6 \times 10^{31} \text{ erg/s}$ in 0.3–2.3 keV energy band, and bolometric luminosity is $L_{\text{bol}} \approx 5.1_{-2.9}^{+3.6} \times 10^{32} \text{ erg/s}$.

3.6 Discussion

3.6.1 Nature of the X-ray Emission from CN Counterparts

Several mechanisms for the generation of X-ray emission after the end of a CN outburst from a non-magnetized WD are known: (i) in the shock when the CN ejecta interact with the interstellar medium, with the stellar wind from the companion or the ejecta from previous CN events (see, e.g., Brecher et al. 1977; Bode & Evans 2008); (ii) the post-nova super-soft X-ray emission resulting from residual hydrogen burning on the WD surface (for a discussion, see below); (iii) the emission from the accretion disk, the corona, and the boundary layer in CN quiescence, including the outbursts of dwarf novae.

In the first case, the X-ray emission of an optically thin thermal plasma with a characteristic luminosity $L_X \lesssim 10^{32} - 10^{34} \text{ erg/s}$ is observed on time scales ~ 100 days after the outburst (e.g., Metzger et al. 2014). Since there are no such recent CNe in our sample, this mechanism may be excluded from further consideration.

The post-nova super-soft X-ray emission also lasts for a relatively short time after the CN outburst (but considerably longer than the shock emission) and is easily identified by its super-soft spectrum. There are two such sources in our sample, and they are discussed

below. Note that super-soft X-ray emission can also be observed in the case of magnetized WDs, polars. In this case, however, steady hydrogen burning occurs more often, and CN outbursts are observed more rarely. Interestingly, there is one confirmed polar and one more source with similar X-ray properties in our sample (for a discussion, see below).

The only mechanism for the generation of X-ray emission long after the CN outburst is the accretion of material from the donor star onto the WD. This mechanism explains the X-ray emission from most of the CN counterparts in our sample, as confirmed by the properties of their X-ray spectra, which allows the X-ray emission to be used as an indicator for measuring the accretion rate in these systems. As has already been discussed above, the boundary layer near the WD surface and the accretion disk corona make a major contribution to the X-ray emission.

Empirically, to describe the emission spectrum of the boundary layer in cataclysmic variables, the isobaric cooling flow model is successfully used. It describes gas cooling at constant pressure from a maximum temperature $kT_{\max} \sim 10 - 60$ keV to a minimum temperature $kT_{\min} \lesssim 1$ keV (e.g., Mukai et al. 2003; Baskill et al. 2005; Pandel et al. 2005; Mukai et al. 2009; Wada et al. 2017). Some dichotomy is observed among the bright sources in our sample of CNe, for which we perform a detailed spectral analysis. While for most of the sources isobaric cooling flow model was preferable (power-law's photon index is typically $\Gamma \sim 2-3$); for four sources - GK Per, V392 Per, X Ser, V4743 Sgr - this was not true. Approximation of their spectra by power-law model gives the photon index $\Gamma \sim 1$. The observed differences in the shape of the spectrum do not clearly correlate with the luminosity of the source. We note that one of the four sources with hard spectra, GK Per, is a confirmed intermediate polar, and V4743 Sgr is a candidate for intermediate polars (Zemko et al. 2016), and the nature of other two sources is unknown, though they can be assumed as intermediate polars; however such a conclusion seems premature and requires more investigation.

The average spectrum of the faint sources (from which fewer than 50 counts were recorded in the survey) is also hard, with a photon index $\Gamma \sim 1$. Based on the available data, we cannot propose a justified interpretation of this result. However, note that the spectral hardness may suggest that an appreciable fraction of these sources are (intermediate) polars with a low accretion rate. According to the catalog by Ritter & Kolb (2003), among them there are one more confirmed intermediate polar (DQ Her) and two candidates (V533 Her and V2467 Cyg). Excluding these sources from the averaging does not change the shape of the average spectrum. Further, as SRG/eROSITA will scan whole sky more frequently, there will be enormous amount of data be collected and, the statistics for individual sources will almost triple, and a detailed spectral analysis of a larger number of sources will be possible, which will probably help clarify the mechanisms of X-ray emission in cataclysmic variables

3.6.2 Post-Nova super-soft X-ray Emission

Among the 52 CN counterparts detected in Xrays, we found four super-soft X-ray sources. The luminosities and temperatures of two of them, V5558 Sgr and V3666 Oph, give a size of

the emitting region compatible with the range of admissible WD sizes (note that for super-soft spectra there exists strong degeneracy between the temperature and luminosity or size). The interpretation of their super-soft X-ray emission as a result of residual hydrogen burning on the WD surface seems quite plausible.

The duration of the post-nova super-soft X-ray phase depends on the WD mass and the initial ejecta mass (see, e.g., Soraisam et al. 2016). super-soft X-ray emission from V5558 Sgr and V3666 Oph is detected ≈ 13 and ≈ 1.6 years after the CN outburst, respectively. The theoretical relation between WD mass and duration of post-nova phase allow us to estimate WD masses of these sources. Based on the theoretical light curves for the post-nova super-soft X-ray phase from Soraisam et al. (2016), we expect that the WD mass in V5558 Sgr should not exceed $\lesssim 0.8M_{\odot}$, while the WD mass in V3666 Oph is $\lesssim 1 M_{\odot}$. The above constraint on the WD mass in V5558 Sgr agrees well with the mass that was found by analyzing the slope of the optical light curve and from optical spectroscopy, $M_{\text{WD}} \approx 0.58 - 0.63 M_{\odot}$ (Poggiani 2010).

To our knowledge, in our Galaxy there are three CNe with a post-nova super-soft X-ray phase duration of more than three years: V723 Cas (18–19 years) (Ness et al. 2008, 2015), GQ Mus (≈ 10 years) (Shanley et al. 1995), V574 Pup (≈ 3.2 years) (Schwarz et al. 2011). V5558 Sgr might be the second longest post-nova in our Galaxy.

3.6.3 Super-soft X-ray Emission from Polars and Their Candidates

V1500 Cyg is a known polar in our Galaxy, and its spectrum exhibits a super-soft component, along with a hard X-ray emission. SRG/eROSITA detects only the super-soft component in the spectrum of this source, while the hard component is below the sensitivity threshold of the all-sky survey. The size of the emitting region of the super-soft component, $\lesssim 104$ km (68%), is much smaller than the WD size and corresponds to the size of the polar region at the magnetic WD pole (Warner 2003). Such a super-soft component is often observed in polars (see, e.g., Ramsay et al. 1996; Ramsay & Cropper 2004).

The super-soft X-ray emission from V5856 Sgr cannot be associated with the post-nova super-soft X-ray emission due to the small size of the emitting surface (see Fig. 3.5). Interestingly, the parameters of the super-soft component in V5856 Sgr are identical to those in V1500 Cyg. Taking this into account, we can assume that V5856 Sgr is also a polar. Due to a small number of counts in the X-ray spectrum of V5856 Sgr, we do not detect the hard component, as in the case of V1500 Cyg. A more rigorous justification of this assumption requires further observations in the optical and X-ray spectral bands. We also note, that V5856 Sgr has been classified as one of the brightest sources in the γ -ray energy band, detected during the CN outburst (Li et al. 2017).

The spectrum of V2491 Cyg is peculiar and it is the only source in our sample whose spectrum cannot be described by any of the one-component models. Though V2491 Cyg was not selected as a super-soft X ray source in our search method, to describe its X-ray spectrum we require a soft black-body component with the temperature of ≈ 65 eV. At

the time of SRG/eROSITA observations, 12 years elapsed since the CN outburst. The WD mass in this system is $M_{\text{WD}} = 1.35 M_{\odot}$ (see Table B.2). For such massive WDs, the duration of the post-nova phase does not exceed a \sim month (Soraisam et al. 2016). Moreover, the emitting surface area of the super-soft X-ray emission in this source is $\approx 6 \times 10^6 \text{ km}^2$, which is much less than the WD area $\approx 10^8 \text{ km}^2$ for a WD with mass $1.35 M_{\odot}$. These facts indicate that the observed super-soft component in the spectrum of V2491 Cyg cannot be associated with the X-ray post-nova phase.

Super-soft X-ray emission from this source was also detected in quiescence earlier. In particular, it was observed by the Suzaku ≈ 2 years after the CN outburst. A super-soft component with a temperature $\approx 77 \text{ eV}$ and a bolometric luminosity $\approx 1.4 \times 10^{35} \times (d/10.5 \text{ kpc}) \text{ erg/s}$ was also detected in these observations (see, e.g., Zemko et al. 2015). Among the hypotheses under consideration, there is the assumption that this source is an intermediate polar. Unfortunately, the SRG/eROSITA data do not help to clarify the nature of this source.

Chapter 4

Observed Accretion Rate Distribution of Sources

*The contents of this chapter is based on the work originally published as
Galiullin & Gilfanov (2021b) Astronomy Letters 47, p. 587–606*

The historical CNe represent a sample of confirmed WDs with non-steady hydrogen burning on their surface. Measuring their post-outburst X-ray luminosity in quiescence allows the accretion rate in these systems to be estimated or limited from above. On the other hand, the steady super-soft sources observed in a bright state with a luminosity $\gtrsim 10^{37}$ erg/s over tens of years represent examples of the sources with steady (or nearly steady) nuclear hydrogen burning. The accretion rate in such sources is easy to estimate by assuming that their luminosity is due to thermonuclear hydrogen burning reactions. A comparison of the derived accretion rate distributions for these two types of accretion WDs allows the predictions of the theory of thermonuclear burning on the WD surface to be tested.

4.0.1 Steady super-soft X-ray Sources

In the case of thermonuclear hydrogen burning on the surface of an accreting WD, the bolometric luminosity of the source is given by Eq.1.20. Using this equation, we calculated the accretion rates for ten known stationary super-soft X-ray sources from the Greiner (1996) catalogue and for three bright sources from Chapter 2.

4.0.2 CN Counterparts in Quiescence

Most of the CN counterparts are in quiescence, except for several super-soft X-ray sources associated with recent CNe and the source VY Aqr that was observed by SRG/eROSITA

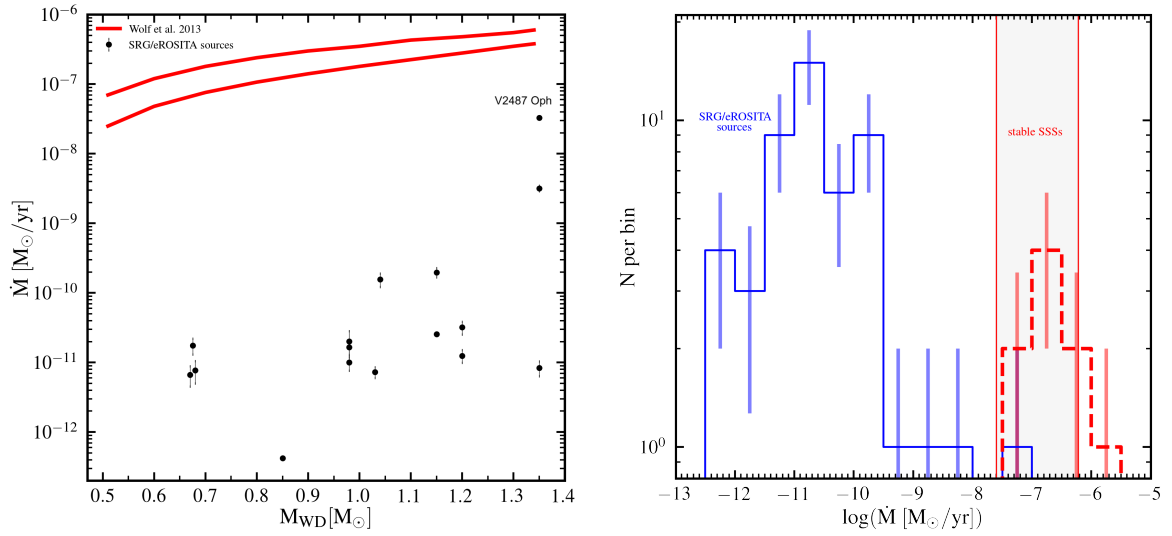


Figure 4.1: (a) Observed distribution of CNe with known WD masses on the $M_{WD} - \dot{M}_{acc}$ plane. The region of steady thermonuclear burning on the surface of an accreting WD obtained from the calculations by Wolf et al. (2013) is represented by the (solid red lines). (b) Observed accretion rate distribution of all CN X-ray counterparts (blue color) and known stable super-soft X-ray sources (red color, dashed lines) from the catalog by Greiner (1996). The right panel is a projection of the $M_{WD} - \dot{M}_{acc}$ plane. The vertical red lines on the right panel are the boundaries of the stability strip for $\dot{M}_{acc} \approx 2.5 \times 10^{-8} M_{\odot}/\text{yr}$ ($M_{WD} \approx 0.51 M_{\odot}$) and $\dot{M}_{acc} \approx 6 \times 10^{-7} M_{\odot}/\text{yr}$ ($M_{WD} \approx 1.34 M_{\odot}$). The CN counterpart falling inside the steady accretion zone in the right panel is V2487 Oph. As it can be seen from the left hand panel, this is a projection affect due to the large mass of the WD in this system. In the $M_{WD} - \dot{M}_{acc}$ plane this source is located well below the stability strip.

at the peak of the dwarf nova outburst. These sources were discussed in detail in previous sections. In quiescence, during the accretion of material onto the WD, half of the radiated energy is released in the accretion disk and half is released in the boundary layer near the WD surface. At the accretion rates under discussion, $\dot{M}_{acc} \lesssim 10^{-9} M_{\odot}/\text{yr}$, the boundary layer is optically thin (see, e.g., [Patterson & Raymond 1985a](#)), while the accretion disk is optically thick ([Shakura & Sunyaev 1988](#)). Some part of the accretion energy is converted into radiation in the optically thin hot corona of the accretion disk (see, e.g., [Meyer & Meyer-Hofmeister 1984, 1994](#)). The radiation from the accretion disk proper has a characteristic temperature $kT \lesssim 10$ eV and is mainly outside the SRG/eROSITA energy range, while the observed X-ray emission is produced by the hot corona of the disk and the boundary layer. Hence, the accretion rate and the X-ray luminosity are related by the relation

$$L_X = \eta \times \frac{G M_* \dot{M}_{acc}}{R_*}, \quad (4.1)$$

where by the X-ray luminosity we mean the luminosity in the wide energy range 0.1–100 keV, η is the fraction of energy emitted in X-ray energy band ($\eta \lesssim 1$), \dot{M}_{acc} is the accretion rate, M_* and R_* - are mass and radius of the WD.

The parameter η depends on the ratio of the fractions of the energy radiated in different parts of the accretion stream—in the accretion disk, the disk corona, and the boundary layer. It follows from the virial theorem that in the case of a slowly rotating WD the fraction of the energy liberated in the boundary layer is 50%. Therefore, given that the boundary layer is optically thin, we expect $\eta \gtrsim 0.5$. The contribution of the radiation from the accretion disk corona will increase η , but, obviously, the condition $\eta < 1$ must be fulfilled. In the calculations below, we assumed $\eta = 0.5$.

To estimate the bolometric correction for the X-ray luminosity measured in the 0.3–2.3 keV energy band, we assumed the source spectrum to be described by a bremsstrahlung model. As the bremsstrahlung temperature varies in the range 5–20 keV, the bolometric correction varies in the range $L_X/L_{0.3-2.3} \approx 2.4 - 5.4$. For the subsequent calculations, we assumed $kT_{br} = 10$ keV and the bolometric correction to be ≈ 3.5 .

In those cases where the WD mass was unknown, we assumed that it was $M_{WD} = 0.8 M_{\odot}$. The WD radius was calculated from the mass–radius relation by [Panei et al. \(2000\)](#).

4.0.3 Accretion Rate Distribution of WDs

Figure 4.1a shows the CN counterparts for which there are WD mass measurements (see Table B.2) on the $M_{WD} - \dot{M}_{acc}$ plane. As follows from this figure, all of the CN counterparts are located well below the “stability strip”, as might be expected from the fact that the sample of historical CNe consists of accreting WDs about which it is known for sure that hydrogen burning on the WD surface is non-steady. We constructed the “stability strip” in Fig. 4.1 based on the calculations by [Wolf et al. \(2013\)](#).

Figure 4.1b presents the accretion rate distribution of all the CN counterparts detected by SRG/eROSITA and known steady super-soft sources from the catalog by [Greiner \(1996\)](#). The projection of the theoretical “stability strip” onto the accretion rate axis is also shown

in this figure. As can be seen from the figure, the sources with non-steady hydrogen burning on the WD surface ($\dot{M}_{\text{acc}} \approx 10^{-12} \sim 10^{-8} M_{\odot}/\text{yr}$) and the stable super-soft sources ($\dot{M}_{\text{acc}} \approx 10^{-7.5} \sim 10^{-6} M_{\odot}/\text{yr}$) occupy different ranges nonintersecting in accretion rate. On the one-dimensional accretion rate distribution, one source, V2487 Oph, falls into the region occupied by the steady super-soft sources. However, as can be seen from Fig. 4.1a, this is a projection effect, and on the $M_{\text{WD}} - \dot{M}_{\text{acc}}$ plane V2487 Oph ($M_{\text{WD}} \approx 1.35 M_{\odot}$ and $\dot{M}_{\text{acc}} \approx 9 \times 10^{-8} M_{\odot}/\text{yr}$) is located below the “stability strip”.

4.0.4 Steady and Non-steady Thermonuclear Hydrogen Burning on the Surface of an Accreting WD

Depending on the accretion rate and the WD mass, hydrogen burning on the WD surface can be steady or non-steady. As follows from Fig. 4.1, the steady super-soft X-ray sources are located, as expected, in the “stability strip”. At the same time, all of the CN counterparts are located well below the “stability strip”, in accordance with the predictions of the theory of thermonuclear burning on the WD surface.

We note that with the current selection method (which is based on the list of historical CNe), it is possible to obtain a sample of reliable accreting WDs with a non-steady thermonuclear burning of hydrogen on their surface. As far as we know, this is the first time such a sample design method has been used.

Additionally, we note that the existence of a “stability strip” is still a matter of debate. A number of calculations suggest that hydrogen thermonuclear burning on the WD surface is non-stationary in the entire range of the accretion rate and WD mass (e.g., [Priyalnik & Kovetz 1995](#); [Yaron et al. 2005](#); [Starrfield et al. 2013](#)). In these models, the amplitude of outbursts decreases with increasing accretion rate, while their frequency increases, with the mass loss decreasing, and such sources become close in their properties to (quasi-)steady super-soft sources. The SRG/eROSITA data under discussion do not allow us to distinguish between these two models.

Chapter 5

SRG/eROSITA – IRAS sample of star-forming galaxies: I. Sample construction and L_X – SFR scaling relation

*The content of this chapter is based on results that will be submitted for publication to the
Astronomy & Astrophysics*

5.1 The SRG/eROSITA – IRAS catalog of star-forming galaxies

Below, we describe the construction procedure of the SRG/eROSITA – IRAS catalog of normal star-forming galaxies.

5.1.1 SRG/eROSITA data

We use the data of four all-sky surveys performed by SRG/eROSITA telescope between Dec 2019 and Dec 2021. The initial data processing and calibration of the eROSITA data were carried out at the Space Research Institute of the Russian Academy of Sciences (IKI RAS) using the software developed by eROSITA X-ray source catalogue science working group of the RU consortium. We also make use of the calibration tasks and calibration database of the eSASS package (eROSITA Science Analysis Software) developed at the Max Planck Institute of Extraterrestrial Physics (MPE), Garching, Germany. The data was preprocessed using the results of ground pre-flight calibrations and flight calibration

observations performed in October–November 2019 and throughout 2020–2022. The data from four sky surveys were combined together to increase sensitivity of the final source catalog.

From SRG/eROSITA source catalog in the 0.3 – 2.3 keV energy band we selected point sources with detection likelihood ≥ 10 . This approximately corresponds to the statistical significance of 4σ . We further excluded a small number of sources having the localization accuracy worse than $20''$ and sources with poorly measured flux, $S/N < 2$.

5.1.2 IRAS source catalogs

We used infra-red source catalogs produced from the data of *InfraRed Astronomical Satellite* (IRAS; Neugebauer et al. 1984) data. The *Imperial IRAS-FSC Redshift Catalogue* (IIFSCz; Wang & Rowan-Robinson 2009) was derived from the *IRAS Faint Source Catalog* (FSC; Moshir et al. 1992). It includes sources with the 60μ flux measured with the signal-to-noise ratio above 5 ($SNR > 5$). Using the IRAS color-color diagram (e.g., Helou 1986; Rowan-Robinson & Crawford 1989), the cirrus, stars, and AGNs were filtered out.

The *Revised IRAS-FSC Redshift Catalogue* (RIFSCz; Wang et al. 2014) is an updated version of the IIFSCz catalogue. It includes 60,303 galaxies selected at 60μ and covers ≈ 60 per cent of the sky at a flux limit of 0.36 Jy (the 90 per cent completeness limit at 60μ). The catalog includes multi-wavelength information from the *tenth data release of the SDSS*, *SDSS DR10*, *WISE All-Sky Data Release*, (SDSS DR10; York et al. 2000; Ahn et al. 2014), *GALEX All-Sky Survey Source Catalog* (GASC; Seibert et al. 2012), *Two Micron All Sky Survey* (Point and Extended Source Catalogues) (2MASS PSC and XSC; Jarrett et al. 2000; Skrutskie et al. 2006), *2MASS Redshift Survey* (Huchra et al. 2012) and the *Planck Catalogue of Compact Sources* (Planck Collaboration et al. 2014).

For further analysis we used the RIFSCz catalog selecting only sources with reliable 60μ and 100μ flux measurements, namely sources with $FQUAL \geq 2$ in both bands.

5.1.3 Cross-matching of SRG/eROSITA and RIFSCz catalogs

We matched SRG/eROSITA and RIFSCz catalogs, using a match radius equal to the radius of 98% positional uncertainty for SRG/eROSITA sources.

The expected fraction of chance matches is $\approx 5\%$. With the match criteria, we found a total of 2331 SRG/eROSITA–RIFSCz matches (see Table 5.1, steps number 1 and 2).

5.1.4 AGN filtering

Although, by construction, majority of SRG/eROSITA–IRAS matches must be star-forming galaxies, the initial list of matches includes some galaxies where contribution of AGN may be important or even dominant. To filter out such galaxies we cross-matched our list with several well known AGN/QSO catalogs. In matching, we used coordinates of objects from RIFSCz which are based on optical and IR data and are more accurate than X-ray positions.

Table 5.1: Construction of the SRG/eROSITA – IRAS catalog of normal star-forming galaxies and their candidates.

#	Filtering step	N_{out}	N_{in}
(1)	(2)	(3)	(4)
<i>SRG/eROSITA–RIFSCz matches</i>			
1	total matches with $\text{DET_LIKE} \geq 10$		2 337
2	0.3 – 2.3 keV flux $S/N \geq 2\sigma$	6	2 331
<i>Filtering of AGNs</i>			
3	DR14Q	57	2 274
4	MILLIQUAS	644	1 630
5	SDSS BPT diagram, galaxies with nuclear activity	157	1 473
6	SIMBAD (QSOs/AGNs)	113	1 360
SRG/eROSITA–IRAS catalog of normal star-forming galaxies and their candidates			1 360
<i>Further selections for L_X–SFR analysis</i>			
7	$\text{FQUAL} \geq 2$ for both 60 μm and 100 μm fluxes		984
8	$D_{25} \leq 60''$		688
9	$\log(F_{0.3-2.3\text{eV}}/F_{\text{FIR}}) \lesssim -3.3$		434
10	distances available		368
11	GALEX NUV flux with $S/N > 2$ available		295
12	K_s band magnitude available		290
13	galaxies classified as star-forming in the SDSS BPT diagram		60

Notes: (1) – The step number; (2) – Description; (3) – Number of sources filtered out at each step; (4) – Number of sources remaining in the catalog after each step.

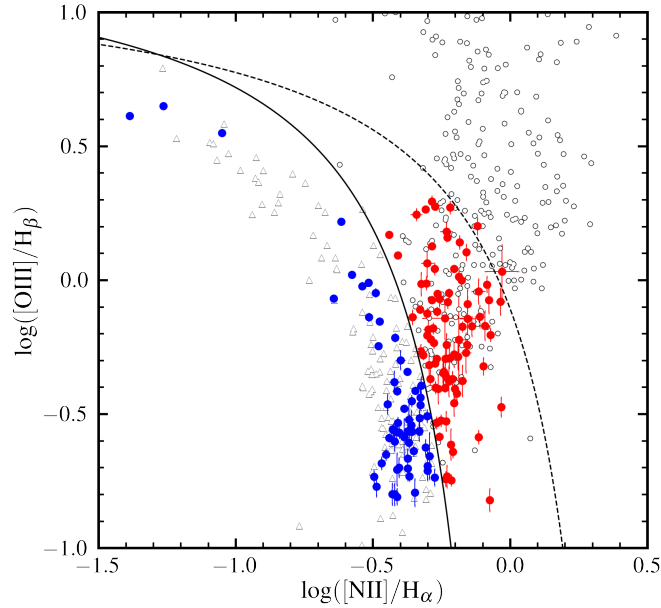


Figure 5.1: BPT diagram for 149 SRG/eROSITA – IRAS galaxies from the SDSS footprint. Line fluxes were adopted from MPA/JHU catalogue (Kauffmann et al. 2003b; Brinchmann et al. 2004; Tremonti et al. 2004). The black solid curve shows the demarcation between star-forming galaxies and AGNs defined by Kauffmann et al. (2003a) and *dashed curve* is based on Kewley et al. (2001). Star-forming galaxies are shown in blue and galaxies with the nuclear activity are shown in red. Galaxies classified as AGNs in steps 3-5 are shown in white circles, and galaxies filtered in further selection for L_X -SFR analysis (steps 7-12) are shown in white triangles (see Table 5.1).

1. Matches with SDSS DR14 quasar catalog (DR14Q; Pâris et al. 2018)¹: To this end we used the SDSS object id provided by the RIFSCz catalog for each source. Out of 2331 X-ray sources, 57 are matched with SDSS DR14Q (step number 3 in Table 5.1)
2. MILLIQUAS catalog of QSOs (Flesch 2021): Cross-matching the remaining X-ray sources using a match radius of 5'' (step number 4 in Table 5.1) with MILLIQUAS quasar catalog, we found 644 matches.
3. Cross-matching with SIMBAD database²: Objects were removed from our sample if they were tagged as: *AGNs; Stars (including variable and cluster of stars); BL Lac; QSOs; Seyfert galaxies*. Out of 1630 X-ray sources, we removed 181 sources (see Table 5.1, step number 6).
4. Finally, for sources in the SDSS footprint, we used the BPT diagram to identify

¹https://www.sdss.org/dr14/algorithms/qso_catalog/

²<https://simbad.u-strasbg.fr/simbad/sim-display?data=otypes>

galaxies with nuclear activity. Emission-line fluxes were adopted from MPA/JHU catalogue³ (Brinchmann et al. 2004; Tremonti et al. 2004; Kauffmann et al. 2003b). Ratio of [O_{III}] to H_β and [N_{II}] to H_α fluxes were used to construct the BPT diagram (Fig. 5.1). The demarcation curve (solid black line) was adopted from Kauffmann et al. (2003a), where sources located above this curve were considered as showing signatures of nuclear activity. Out of 1449 sources left from the previous filtering step, 149 could be placed on the BPT diagram of which 89 were classified as galaxies with nuclear activity and remaining 60 objects were classified as star-forming galaxies (see below).

After all these filtering steps for 2331 eROSITA X-ray sources having IRAS matches, we removed 971 known AGNs and QSOs. The 1360 X-ray sources passed through this selection compose the 1st edition of SRG/eROSITA–IRAS catalog of normal star-forming galaxies. In this work, we will only use these X-ray sources for further analysis.

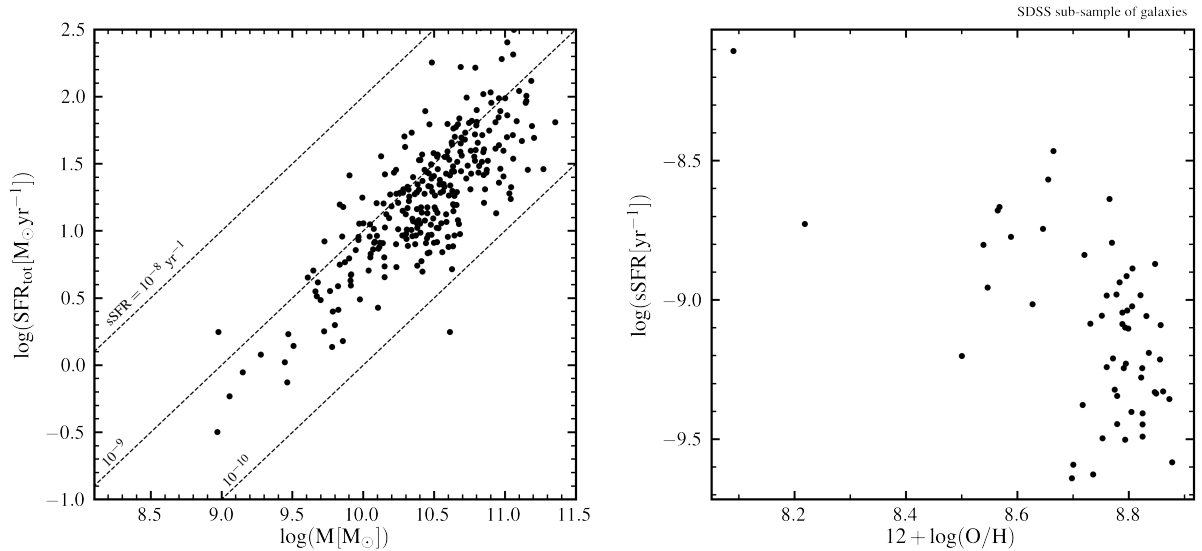


Figure 5.2: *Left*: SFR– M_* plane for 290 star-forming galaxies from SRG/eROSITA – IRAS catalog for which stellar masses and SFR could be computed. Dotted lines correspond to constant specific SFR. *Right*: specific SFR versus metallicity for 60 star-forming galaxies in the SDSS footprint.

5.1.5 Physical parameters of galaxies

For analysis of the L_X –SFR relation for star-forming galaxies the SRG/eROSITA–IRAS catalog, we apply a few additional filtering steps and complement with additional multi-

³https://www.sdss.org/dr14/spectro/galaxy_mpajhu/

wavelength data required for accurate SFR estimates.

Angular size and distance

The current edition of the SRG/eROSITA–IRAS catalog was derived from the eROSITA catalog of point sources. To make this selection consistent with IR data we filtered out galaxies having large extent in optical band. Namely, we filtered out galaxies with $D_{25} > 60''$. To this end, we matched the catalog with HyperLeda⁴ database (Makarov et al. 2014) using a $5''$ search radius. Using HyperLeda matches we collected D_{25} and distances.

Infrared luminosity

To compute far-infrared (FIR, $\lambda = 42–122 \mu m$) luminosity we used the well known relation from Helou et al. (1988):

$$L_{\text{FIR}} = 3.29 \times 10^{-22} \times (2.58\mathcal{L}_{\nu}(60\mu m) + \mathcal{L}_{\nu}(100\mu m)) [L_{\odot}], \quad (5.1)$$

where L_{FIR} is given in solar units⁵, and $\mathcal{L}_{\nu}(60, 100\mu m)$ are observed luminosities \mathcal{L}_{ν} per unit frequency in units of $\text{erg s}^{-1} \text{Hz}^{-1}$ (Helou et al. 1988; Takeuchi et al. 2005).

Total infrared luminosity (TIR, $\lambda = 3 – 1100 \mu m$) was computed following Dale et al. (2001):

$$L_{\text{TIR}} = L_{\text{FIR}} \times 10^{a_0 + a_1x + a_2x^2 + a_3x^3 + a_4x^4} [L_{\odot}], \quad x = \log(S_{60}/S_{100}) \quad (5.2)$$

where $S_{60,100}$ are flux densities (Jy) at wavelengths 60, $100\mu m$, and coefficients a_i ⁶ are adopted from Dale et al. (2001).

We note that Dale & Helou (2002) provides another relation estimating TIR based on three IR bands – 25, 60, $100\mu m$. For our sample, relations of both Dale et al. (2001) and Dale & Helou (2002) give consistent TIR luminosities. However, only $\sim 60\%$ of objects in our catalog have IR flux measurement in all three bands. We therefore used Eq.5.2 based on two IR bands which can be applied to the entire catalog.

Star-formation rate

We used a composite SFR proxy based on TIR and near-ultraviolet (NUV, $\lambda = 2312 \text{ \AA}$) luminosities. Salpeter initial mass function (IMF) was assumed in the stellar mass range of $0.1 – 100 M_{\odot}$. We made these choices in order to facilitate comparison with previous work (e.g., Mineo et al. 2012a; Brorby et al. 2016). Thus, the total SFR is given by:

$$\text{SFR}_{\text{tot}}(M_{\odot} \text{ yr}^{-1}) = \text{SFR}_{\text{NUV}}^0 + (1 - \eta)\text{SFR}_{\text{TIR}}, \quad (5.3)$$

where

$$\text{SFR}_{\text{TIR}}(M_{\odot} \text{ yr}^{-1}) = 4.6 \times 10^{-44} L_{\text{TIR}} (\text{erg s}^{-1}), \quad (5.4)$$

⁴<http://leda.univ-lyon1.fr/>

⁵Solar luminosity, $L_{\odot} = 3.839 \times 10^{33} \text{ erg s}^{-1}$.

⁶(a_0, a_1, a_2, a_3, a_4) = (0.2738, -0.0282 , 0.7281, 0.6208, 0.9118)

$$\text{SFR}_{\text{NUV}}^0 (M_{\odot} \text{ yr}^{-1}) = 1.2 \times 10^{-43} (\nu L_{\nu})_{\text{NUV,obs}} (\text{erg s}^{-1}), \quad (5.5)$$

where $(\nu L_{\nu})_{\text{NUV,obs}}$ is observed near ultra-violet (NUV) luminosity at $\lambda = 2312 \text{ \AA}$, η is a correction factor accounting for the fraction of IR emission due to the old stellar population. We assumed that $\eta \approx 0$ for starburst galaxies, i.e. all of the IR emission is produced due to recent star formation activity (Hirashita et al. 2003; Brorby et al. 2016).

NUV fluxes were collected from the GALEX data release (GR6/7)⁷ by matching RIF-SCz and GALEX catalogues using GALEX’s photometric identification numbers provided in RIFSCz. The requirement to have NUV flux measurement reduced the number of galaxies to 440 in our sample.

Stellar mass

Stellar masses of galaxies are estimated using K_s band luminosity and color dependent mass-to-light ratio following Bell et al. (2003):

$$\log(M_*/L_K) = -0.842 + 0.551(B - I)_0, \quad (5.6)$$

where $(B - I)_0$ is absorption corrected color from HyperLeda database. Eq.5.6 is derived using Bell et al. (2003) results for $(B - V)$ and $(V - I)$ colors. We adopted solar absolute magnitude in K_s band equal to $K_{s,\odot} = 3.27$ (Willmer 2018) to compute K_s band luminosity. The median M/L ratio was assumed = 2 for galaxies for which either B or I magnitude was not available.

The 290 galaxies from SRG/eROSITA – IRAS catalog, for which both M_* and SFR can be determined, are plotted on the M_* –SFR plane in Fig. 5.2. The dashed black lines show the constant specific SFR lines. As one can see from this plot, majority of galaxies are moderately star-forming, with a median specific SFR of $6.3 \times 10^{-10} \text{ yr}^{-1}$. In all but thirteen galaxies, specific SFR exceeds $2 \times 10^{-10} \text{ yr}^{-1}$ i.e. the contribution of LMXBs to the X-ray luminosity of their X-ray binaries is sufficiently small and can be neglected according to the criterion proposed by Mineo et al. (2012a).

Metallicity

For galaxies in the SDSS footprint which could be placed on the BPT diagram and were identified as star-forming galaxies (Fig.5.1), we can also estimate the gas-phase metallicity. Following the method proposed in Pettini & Pagel (2004), we converted the emission-line flux ratio to the metallicity:

$$12 + \log(\text{O}/\text{H}) = 8.73 - 0.32 \times \text{O3N2}, \quad (5.7)$$

where O3N2 is logarithm of the ratio of $[\text{O}_{\text{III}}]/\text{H}_{\beta}$ and $[\text{N}_{\text{II}}]/\text{H}_{\alpha}$:

$$\text{O3N2} = \log([\text{O}_{\text{III}}]/\text{H}_{\beta}) - \log([\text{N}_{\text{II}}]/\text{H}_{\alpha}), \quad (5.8)$$

⁷<https://galex.stsci.edu/GR6/>

Solar metallicity is assumed to be equal to $12 + \log(\text{O}/\text{H})_{\odot} = 8.69$ (Allende Prieto et al. 2001; Asplund et al. 2004).

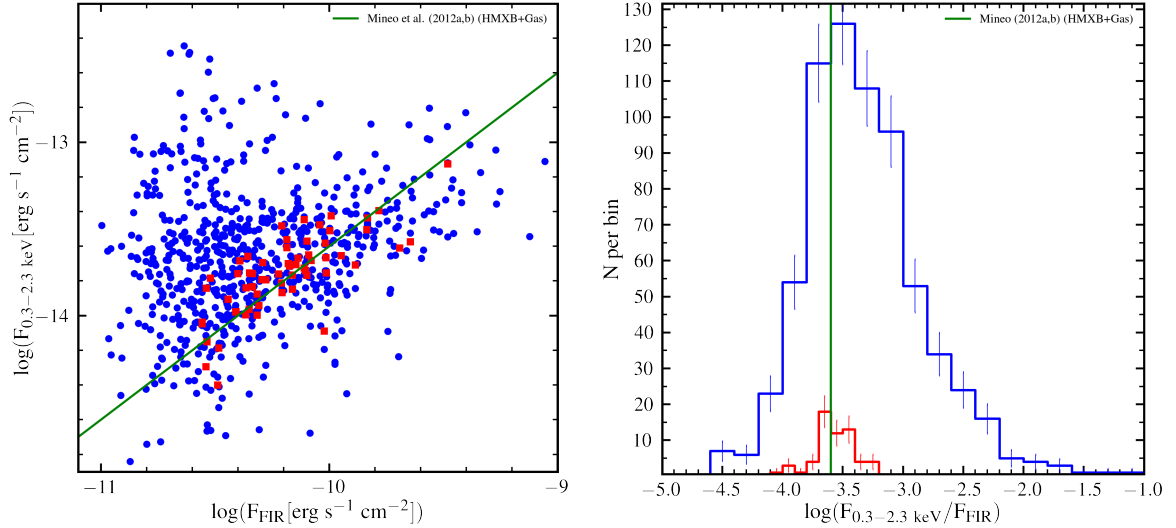


Figure 5.3: *Left panel:* $F_X - F_{\text{FIR}}$ plot for 688 galaxies (blue) with FIR flux available (step 8 in Table 5.1) and 60 galaxies classified as star-forming (red). The solid line shows the $F_X - F_{\text{FIR}}$ relation for nearby star-forming galaxies from Mineo et al. (2012a,b) (see text for details). *Right panel:* Distribution of F_X/F_{FIR} ratio for the galaxies from left panel.

5.2 X-ray emission from star-forming galaxies

5.2.1 $F_X - F_{\text{FIR}}$ relation: star-formation and nuclear activity

For the galaxies with FIR flux available (step 8 in Table 5.1, 688 galaxies), we show the 0.3–2.3 keV X-ray flux versus FIR flux in Fig. 5.3. The relation $F_X = 2.3 \times 10^{-4} F_{\text{FIR}}$ for nearby star-forming galaxies is shown in solid green line. The relation is computed using L_X –SFR relation from Mineo et al. (2012a,b). While computing the relation, we also assumed the $\text{SFR} = 2 \times 10^{-44} L_{\text{FIR}}$ scaling relation. We used a combination of scaling relations from Mineo et al. (2012a) for HMXBs, $L_{0.5-8 \text{ keV}}^{\text{HMXB}} = 2.6 \times 10^{39} \text{SFR}$, and for diffuse emission Mineo et al. (2012b) $L_{0.5-2 \text{ keV}}^{\text{diff}} = 8.3 \times 10^{38} \text{SFR}$ in units of $\text{erg s}^{-1} (\text{M}_{\odot} \text{yr}^{-1})^{-1}$. X-ray luminosities $L_{0.5-8 \text{ keV}}^{\text{HMXB}}$ and $L_{0.5-2 \text{ keV}}^{\text{diff}}$ were converted to 0.3–2.3 keV energy band by multiplying a factor of 0.5 and 1.1, respectively, assuming power-law with $\Gamma = 1.7$ and two-temperature thermal plasma model with $kT_1 = 0.24 \text{ keV}$ and $kT_2 = 0.71 \text{ keV}$, respectively. A median hydrogen column density of $3 \times 10^{20} \text{ cm}^{-2}$ was assumed. The median ratio of galaxies $F_{\text{TIR}}/F_{\text{FIR}} = 2.2$ and the Eq. 5.4 were used to estimate SFR.

As one can see, a large number of galaxies have X-ray luminosities ~ 1.5 dex higher than the expected X-ray output of star-formation estimated based on their FIR luminosity. This is further illustrated by the F_X/F_{FIR} distribution plotted in the right-hand panel of Fig. 5.3. The distribution is asymmetric, with an obvious wing extending towards higher values of F_X/F_{FIR} than typically expected for star-forming galaxies. As we do not expect any significant LMXB contamination in these galaxies (section 2), the plausible candidate for excess X-ray emission is some weak or moderate activity of the nucleus, which are not identified in our AGN filtering procedure.

Obviously, these galaxies need to be excluded from the analysis of the L_X –SFR relation. A possible way of doing this would be optical spectroscopy of all galaxies in question. This can be done in future, however it will take large telescope times as we will need spectroscopic data of a few hundred galaxies. Alternatively, one could apply a cut over F_X/F_{FIR} , though, any such cut would introduce a bias and some more elaborate procedure is needed. To this end we used the fact that star-forming galaxies, in addition to X-ray emission from HMXBs, possess a comparable luminosity emission of hot diffuse ISM, which is also proportional to SFR (Mineo et al. 2012b). This emission manifests itself as a soft component with temperature of $\sim 0.3 - 0.7$ keV, superimposed to the power-like emission of X-ray binaries and AGN (Mineo et al. 2012b).

5.2.2 Dependence of the X-ray spectrum on F_X/F_{FIR}

In order to achieve a meaningful statistical quality on spectra, we binned the galaxies over F_X/F_{FIR} and averaged the spectra of all galaxies within each bin. To extract spectra for source and background regions, we used a circle with a radius of $90''$ centred at the source position and an annulus with inner and outer radii of $120''$ and $240''$, respectively. To sum the spectra and combine their response matrices, we used FTOOL’s task `addspec`. The spectral channels were grouped to have 5 counts per channel using `grppha` task. The spectra were analyzed with XSPEC v.12 (Arnaud 1996) and were approximated using the C–statistic (Cash 1979). The spectra were then fit with a two component model consisting of a power-law component and a thermal emission of optically thin plasma (`vmekal` model in XSPEC). We used the convolution model `cflux` to calculate fluxes of hard and soft components and then computed the ratio $R = F_{\text{mekal}}/F_{\text{PL}}$.

We obtained typical values for temperatures $kT \approx 0.3 - 0.6$ keV and the photon indices of $\Gamma \approx 1.5 - 2.0$ and the ratio R varying from $\log(R) \sim -2$ to $\log(R) \sim -0.5$. The hydrogen column density was fixed at $5 \times 10^{20} \text{ cm}^{-2}$. In order to investigate the dependence of R on possible variations of N_H among the galaxies binned together, we run a set of simulations and found that combining spectra with N_H in the range $2 \times 10^{20} - 2 \times 10^{21} \text{ cm}^{-2}$ leads to an error in the ratio of the order of $\delta \log(R) \sim 0.08$ ($\sim 20\%$ in absolute value) which is reasonably acceptable accuracy for the purpose of this calculation. The dependence of the ratio R on the F_X/F_{FIR} is shown in the right hand panel of Fig. 5.4.

Mineo et al. (2012b) used Chandra observations of a sample of nearby galaxies to investigate emission of diffuse hot gas in star-forming galaxies. As galaxies in their study were resolved, the emission from the central AGN was removed and they could also reliably

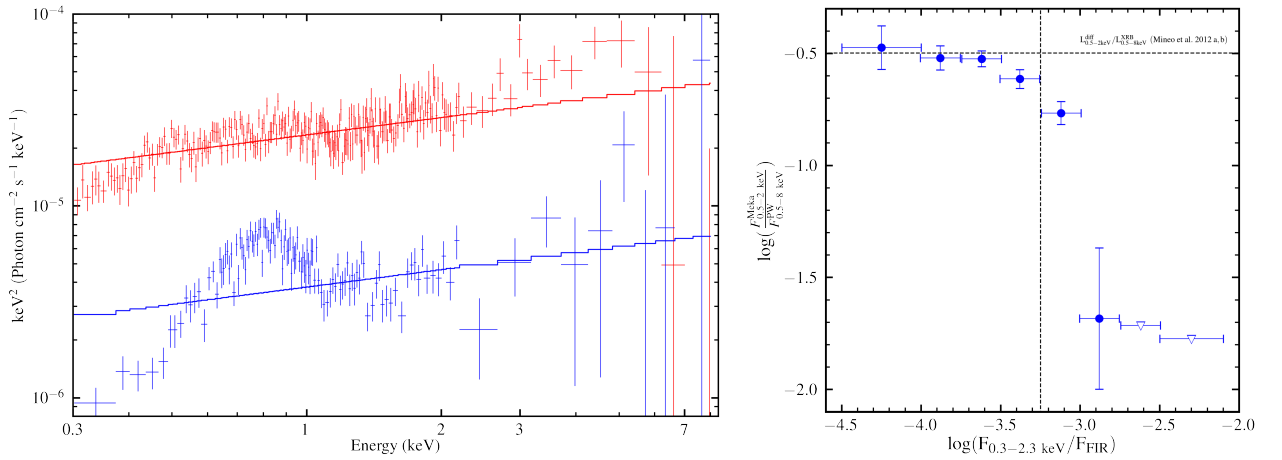


Figure 5.4: *Left panel:* Combined spectra of galaxies with high (red) and low (blue) F_X/F_{IR} ratio. *Right panel:* Ratio of the 0.5–2.0 keV luminosity of soft thermal plasma emission to the hard power-law emission as a function of F_X/F_{IR} ratio. As discussed in the text, this ratio characterizes the contribution of nuclear activity to the X-ray output of a star-forming galaxy. The dashed horizontal line shows the average ratio obtained by Mineo et al. (2012a,b) for nearby star-forming galaxies. The dashed vertical line at $\log_{10}(F_X/F_{\text{FIR}}) = -3.3$ shows the cut chosen to exclude galaxies with notable contribution of nuclear activity.

separate the emission from X-ray binaries and diffuse hot gas. They obtained the mean luminosity ratio of gas to X-ray binaries of $\log(R) \approx -0.5$. This value will be used as a reference and shown by the dashed horizontal line in Fig. 5.4.

As one can see, the three bins with low F_X/F_{FIR} agree quite well with the value of R from Mineo et al. (2012b) (dashed horizontal line), but at larger F_X/F_{FIR} the luminosity ratio R drops by more than an order of magnitude. Given the fact that luminosity of both hot ISM and HMXBs in star-forming galaxies scale with SFR, their luminosity ratio R should remain constant. The drop in R can be plausibly explained by the increasing contribution of some additional emission component unrelated to HMXBs and having a power-law spectrum similar to that of HMXBs. Plausible candidates to such an additional emission component with a hard power-law spectrum are LMXBs and emission of the galactic nucleus. As for LMXBs, specific SFR of all galaxies plotted in Figure 5.4 does exceed 10^{-10} yr^{-1} (Fig. 5.2) and thus, the contribution of LMXBs to the total luminosity of X-ray binaries should not exceed 20%, i.e. can not explain the excess in F_X/F_{FIR} and drop in R . The only remaining candidate is activity of the nucleus which luminosity can easily exceed that of X-ray binaries by many orders of magnitude.

The values of R can be used as a measure of the fractional contribution of the active nucleus to the total emission of HMXBs in the galaxy. From definition of R one can easily

derive:

$$\frac{F_{AGN}}{F_{HMXB}} = \frac{R_0}{R} - 1 \quad (5.9)$$

where $\log(R_0) \approx -0.5$ is the reference values of R for star-forming galaxies from Mineo et al. (2012b).

For the further analysis of L_X –SFR relation we chose to apply the cut of $\log(R) > -0.6$ corresponding to less than $\approx 26\%$ contribution of the nucleus. Ideally, the cut in R should have been applied to individual galaxies. However, the all-sky survey data does not have sufficient statistical significance to measure R for each individual galaxy and stacking needs to be done. To this end, we use the diagram shown in the right panel of Fig. 5.2 to segregate galaxies based on their F_X/F_{FIR} ratio. The chosen cut in R translates to the cut in $F_X/F_{FIR} < 5 \times 10^{-4}$. The disadvantage of this procedure is that we segregate galaxies based on the value of the parameter which we would like to determine. This introduces inevitable bias to our measurement. A way to avoid such a bias would be detailed optical and/or X-ray spectroscopy of all galaxies in our sample which we aim to do in the future.

Using the cut of $\log F_X/F_{FIR} < -3.3$ we selected 434 galaxies. Out of 434 selected galaxies, 368 had measured distances in the HyperLeda database.

5.2.3 The scaling relations

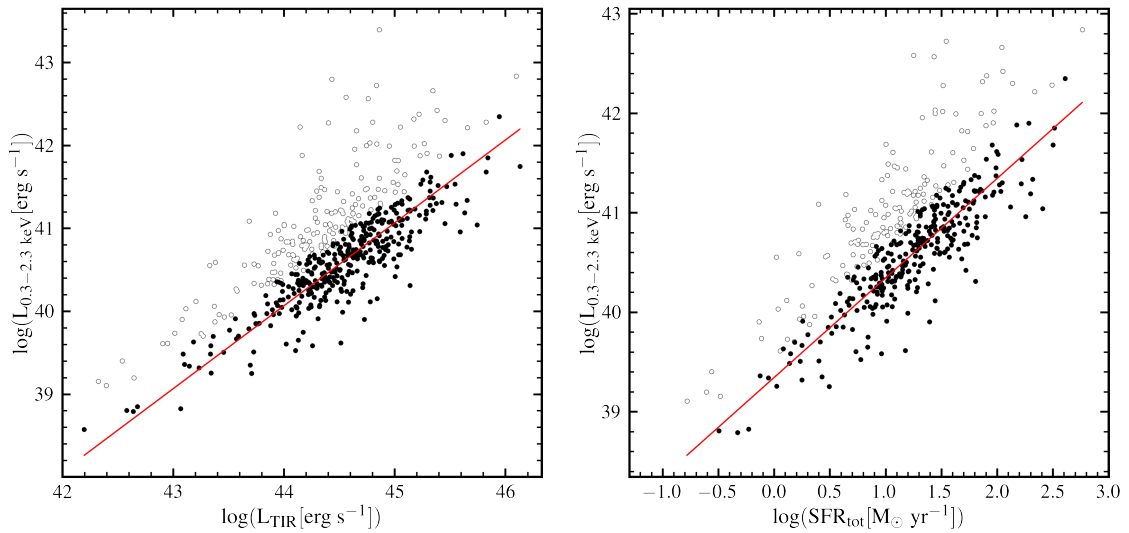


Figure 5.5: $L_X - L_{\text{TIR}}$ (left) and $L_X - \text{SFR}$ (right) relations. X-ray luminosity refers to the 0.3–2.3 keV band. The solid circles show truncated sample of 295 galaxies (step 11 in Table 5.1), open circles show galaxies excluded by truncation over F_X/F_{FIR} . The solid lines show respective scaling relations from Table 5.2.

Table 5.2: The different scaling relations for local, star-forming galaxies, observed by SRG/eROSITA.

Correlation.....	log(A)		σ (dex)		N _{src}
	0.3 – 2.3 keV	0.5 – 2 keV	0.3 – 2.3 keV	0.5 – 2 keV	
(1)	(2)		(3)		(4)
log(F_X/F_{FIR})	–3.58	–3.64	0.26	0.30	434
log(L_X/L_{TIR})	–3.93	–3.99	0.25	0.26	368
log($L_X/\text{SFR}_{\text{tot}}$)	39.35	39.29	0.24	0.26	295
for 12 + log(O/H) = 8.5 – 8.9	39.35	39.32	0.19	0.22	55

Notes: (1) – correlation in log-log scale: $\log(y) = \log(A) + \log(x)$; (2) - the median value and its error for two X-ray energy bands: 0.3 – 2.3 and 0.5 – 2 keV; (3) - the dispersion around the median $\log(A)$ is given as the standard deviation. (4) – The number of sources used to calculate the median of scaling relation. Scaling relations in units of $\text{erg s}^{-1} (M_{\odot} \text{ yr}^{-1})^{-1}$.

We study scaling relations in two energy bands – the 0.3–2.3 keV band which is the optimal eROSITA band for power-law spectra with photon index of $\Gamma \sim 1.7 – 2.0$ and the 0.5–2 keV band to facilitate comparison with previous work.

The only unbiased way to measure the slope of $F_X – F_{\text{FIR}}$ and $L_X – \text{SFR}$ relations is using the sample of star-forming galaxies classified as such on the SDSS BPT diagram, as all other samples were truncated based on the F_x/F_{FIR} value. This sample is relatively small and contains 60 objects (Table 5.1). Using the least square fit in log-log space, $\log(F_x) = a + b \times \log(F_{\text{FIR}})$ we obtain the best fit values of slope $b = 0.80 \pm 0.10$ with $rms = 0.18$ dex. Similarly, fitting $L_X – \text{SFR}$ relation we obtain the slope of $b = 1.08 \pm 0.06$ with scatter $rms = 0.19$ dex. For the sake of completeness, we quote results for the sample of 434 galaxies truncated over F_X/F_{FIR} ratio (step 9 in Table 5.1), we obtain the slope of $b = 0.96 \pm 0.03$ with $rms = 0.24$ dex.

These results confirm earlier findings that $F_X – F_{\text{FIR}}$ and $L_X – \text{SFR}$ relations are essentially linear (Ranalli et al. 2003; Mineo et al. 2012a) and therefore we fix the slope at $b = 1$ in our analysis and derive scaling factors relating X-ray flux and luminosity with FIR and TIR flux and SFR. The scaling relations are shown in Fig.5.5 and scaling factors are listed in Table 5.2. They are further discussed in Section 4.

Abundance of metals in hot ISM

Using the sample of 434 galaxies truncated over F_X/F_{FIR} ratio (step 9 in Table 5.1), we construct an average X-ray spectrum of a star-forming galaxy. This spectrum was approximated by a model consisting of a power-law and emission of the optically thin plasma, modified by the low energy absorption. For the optically thin plasma emission we checked both single- and two- temperature models. Specifically, we used `tbvarabs*(vmekal+pow)` and `tbvarabs*(vmekal+vmekal+pow)` models in XSPEC. We also tested models where the power-law and thermal component had independent absorption columns and found consis-

Table 5.3: Model fit results of combined spectrum of 434 galaxies in our sample.

Model	N_{H}	Γ	kT_1	kT_2	Abundance		C – stat/dof
	(10^{21}cm^{-2})	(3)	(keV)	(keV)	O (solar)	Fe (solar)	
(1)	(2)	(3)	(4)	(5)	(6)	(7)	
1) PW + 2T <i>vmekal</i>	0.53 ± 0.19	1.42 ± 0.15	0.61 ± 0.04	0.26 ± 0.02	1.0	1.0	803.8/750
2) PW + 2T <i>vmekal</i>	0.53 ± 0.19	1.42 ± 0.15	0.61 ± 0.04	0.26 ± 0.02	$1.25^{+0.68}_{-0.41}$	$1.36^{+0.91}_{-0.46}$	803.3/748

Notes: (1) – XSPEC models: power-law and two temperature *vmekal*; (2) – photon index of the power-law model; (4) and (5) – temperatures of *vmekal* model; (6) and (7) – Oxygen and Ferrum abundances relative solar values; (8) – C-statistics and degree of freedom.

tent values for their column densities (but with larger errors). For the single temperature plasma model we obtained the best-fit temperature of $kT \approx 0.5$ keV, and for the two temperature plasma model we obtained $kT_1 \approx 0.3$ keV and $kT_2 \approx 0.6$ keV. Adding the second thermal emission component significantly improves the fit, with the p-value of $\sim 10^{-10}$.

Due to the moderate number of counts, the simultaneous fit of all thirteen metal abundances of the *vmekal* model does not give constraining results. Making abundances of oxygen and iron free parameters of the fit and fixing others at solar values we did not obtain any improvement of the quality of the fit, with the best fit abundances of the two elements being consistent with their solar values (see Table 5.3). It is interesting to note that the median gas-phase metallicity of BPT star-forming galaxies (≈ 8.7) is consistent with the O abundance estimated from spectral fit. If we use the oxygen abundance as a proxy of α elements, then the $[\alpha/\text{Fe}]$ ratio is about ~ -0.04 . Assuming the elements' error propagation and symmetric errors, the 3-sigma upper (lower) limit on the ratio is about ~ 0.8 (~ -0.9).

Core-collapse supernovae result in $[\alpha/\text{Fe}] \sim 0.4$, while type Ia supernovae yield ~ 0.0 (e.g., Nomoto et al. 2013). This suggests that the metal enrichment of galaxies in our sample is due to both core-collapse and type Ia supernovae. The ratio of $[\alpha/\text{Fe}] \sim 0.4$ is found in the dwarf starburst and ultraluminous infrared galaxies (e.g., Grimes et al. 2005).

5.3 Discussion

5.3.1 Scaling relations for individual spectral components

Taking into account the result of the approximation of the combined spectrum of galaxies, we estimated the scaling relation for power-law and gas components to be $\beta_{\text{PL}} = L_{0.5-8 \text{ keV}}^{\text{PL}}/\text{SFR} \approx 2.9 \times 10^{39}$ and $\beta_{\text{mekal}} = L_{0.5-2 \text{ keV}}^{\text{mekal}}/\text{SFR} \approx 9.8 \times 10^{38}$ in units of $\text{erg s}^{-1}(\text{M}_{\odot}\text{yr}^{-1})^{-1}$. The values were estimated by dividing fluxes obtained by *cflux* model by a median $\text{SFR}/(4\pi \times D^2)$ ratio of galaxies. For the power-law component, we also estimated the X-ray-to-TIR scaling relation, where $L_{0.5-8 \text{ keV}}^{\text{PL}}/L_{\text{TIR}} \approx 1.5 \times 10^{-4}$.

Using 55 star-forming galaxies in BPT diagram we estimated the scaling relations β_{PL} and β_{mekal} for two bins over the metallicity range $12 + \log(\text{O}/\text{H}) = 8.5 - 8.9$ (see Fig. 5.6).

5.3.2 Comparison with previous studies

Most of the galaxies in our sample have median redshift of ≈ 0.03 and the 90% quantile interval of $0.01 - 0.06$, so we compare our results with the scaling relations for the local, star-forming galaxies. The scaling relation for 434 galaxies between observed X-ray and FIR fluxes is $F_{0.5-2 \text{ keV}}/F_{\text{FIR}} \approx 2.3 \times 10^{-4}$ with the dispersion of 0.3 dex. [Ranalli et al. \(2003\)](#) found the same scaling relation for 23 local, star-forming galaxies, where ratio is $L_{0.5-2 \text{ keV}}/L_{\text{FIR}} \approx 2 \times 10^{-4}$ with the dispersion of 0.3 dex.

Generally, the total X-ray emission of star-forming galaxies consists of i) resolved emission of XRBs (HMXBs and LMXBs); ii) unresolved emission: the hot, diffuse gas of ISM and faint compact objects; and iii) the active nuclei. The contribution of the AGNs and LMXBs to the total X-ray emission of galaxies is expected to be negligible due to our selection procedure. We assumed, that the total X-ray emission of galaxies in our sample consists of the total emission of HMXBs, faint compact objects (β_{PL}) and the hot, diffuse gas (β_{mekal}). [Mineo et al. \(2012a\)](#) showed, that total emission of HMXBs in star-forming galaxies scale with the SFR and TIR luminosity, so $\beta_{\text{HMXB}}^{\text{M12}} = L_{0.5-8 \text{ keV}}^{\text{HMXB}}/\text{SFR} \approx 2.6 \times 10^{39} \text{ erg s}^{-1}(\text{M}_{\odot}\text{yr}^{-1})^{-1}$ and $L_{0.5-8 \text{ keV}}^{\text{HMXB}}/L_{\text{TIR}} \approx 1.8 \times 10^{-4}$ with dispersion 0.43 and 0.54 dex, respectively. Our estimation for power-law components, β_{PL} , agrees with $\beta_{\text{HMXB}}^{\text{M12}}$ for HMXBs. The same agreement is for $L_{0.5-8 \text{ keV}}^{\text{PL}}/L_{\text{TIR}}$ and $L_{0.5-8 \text{ keV}}^{\text{HMXB}}/L_{\text{TIR}}$. Slightly deviation by a factor of $\approx 1.1 - 1.2$ might be due to different methods used to calculate the total IR luminosities.

[Mineo et al. \(2012b\)](#) showed that the luminosity of hot ISM gas in star-forming galaxies scales with SFR, where $\beta_{\text{Gas}}^{\text{M12}} = L_{0.5-2 \text{ keV}}^{\text{mekal}}/\text{SFR} \approx 5.2 \times 10^{38} \text{ erg s}^{-1}(\text{M}_{\odot}\text{yr}^{-1})^{-1}$ with a dispersion of 0.34 dex. Unresolved X-ray sources contribute about $\approx 40\%$ to the total emission, so scaling relation for hot ISM gas and faint unresolved sources is $\beta_{\text{diff}}^{\text{M12}} = L_{0.5-2 \text{ keV}}^{\text{diff}}/\text{SFR} \approx 8.3 \times 10^{38} \text{ erg s}^{-1}(\text{M}_{\odot}\text{yr}^{-1})^{-1}$ with the dispersion of 0.34 dex. The β_{mekal} for the soft X-ray component of the combined spectrum by a factor of ≈ 1.8 and ≈ 1.2 exceeds $\beta_{\text{Gas}}^{\text{M12}}$ and $\beta_{\text{diff}}^{\text{M12}}$ respectively.

The temperatures of the hot gas component of combined spectrum are $kT_1 \approx 0.6 \text{ keV}$ and $kT_2 \approx 0.3 \text{ keV}$, and they agree well with the average temperatures of thermal emission, estimated by [Mineo et al. \(2012b\)](#) for a sample of local galaxies ($kT_1 \approx 0.24 \text{ keV}$ and $kT_2 \approx 0.71 \text{ keV}$). [Mineo et al. \(2012b\)](#) noted that the enhance of the $\beta_{\text{diff}}^{\text{M12}}$ happens due to the contribution faint compact objects (e.g., CVs, YSO, hot stars) to the soft 0.5–2 keV energy band. And the galaxy-to-galaxy variation of the hot gas properties leads to the significant scatter of the point around the best-fits of $\beta_{\text{Gas}}^{\text{M12}}$ and $\beta_{\text{diff}}^{\text{M12}}$. We think, that enhancement β_{mekal} relative to $\beta_{\text{Gas}}^{\text{M12}}$ might be also caused by the galaxy-to-galaxy variation of the hot gas properties.

5.3.3 Metallicity dependence of $L_X - \text{SFR}$ scaling relations

We compared our scaling relations of 55 star-forming galaxies with other studies, considering gas-phase metallicities. [Fig. 5.6](#) shows two panels for β_{PL} and β_{mekal} versus gas-phase metallicities. Different lines correspond to $L_X - \text{SFR}$ of other studies. We used the similar

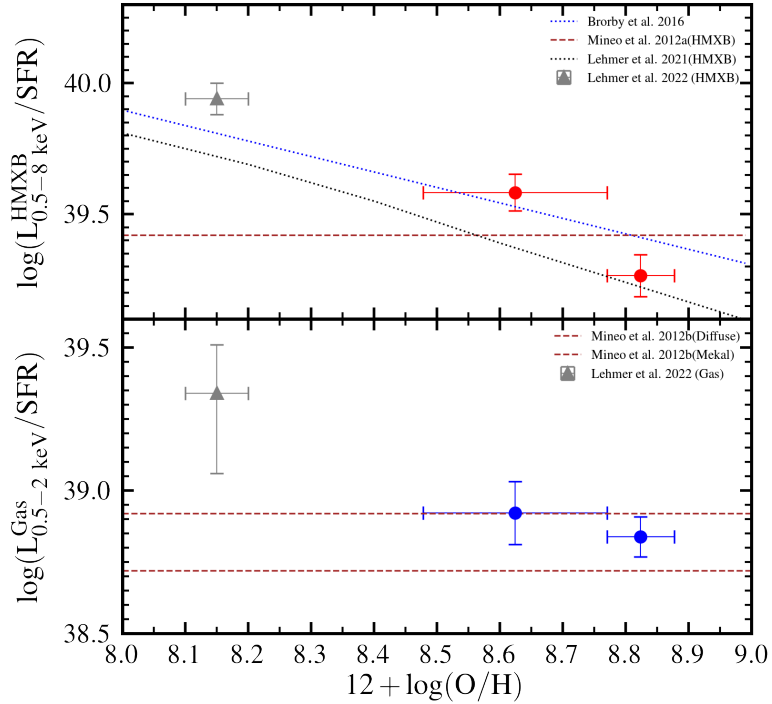


Figure 5.6: Comparison of the scaling relations for HMXBs (top) and hot gas (bottom) with other studies. The x-axis shows the gas-phase metallicity. Our results are shown in red (top) and blue squares (bottom). Grey squares: [Lehmer et al. \(2022b\)](#); Black, dotted line: [\(Lehmer et al. 2021\)](#); Blue, dotted line: [Brorby et al. \(2016\)](#); red, dotted lines: [Mineo et al. \(2012a,b\)](#). See the discussion for more detail.

Salpeter IMF as [Mineo et al. \(2012a,b\)](#) and [Brorby et al. \(2016\)](#). For 30 local star-forming galaxies with metallicities near $0.3 Z_{\odot}$, [Lehmer et al. \(2022b\)](#) have estimated the scaling relations for HMXB populations and hot gas by analyzing X-ray spectra of galaxies. To compare our results with the [Lehmer et al. \(2022b\)](#), we increased their scaling relations by a factor of 0.25 dex to convert Kroupa’s IMF into Salpeter’s IMF.

According to our data, the results for power-law components are consistent with studies of galaxies with low metallicity. The variation between two metallicity bins of 55 star-forming galaxies is 0.27 ± 0.09 dex with the significance $\approx 3\sigma$, which is consistent with the expected amplitude from other studies ~ 0.12 dex ([Brorby et al. 2016](#)) and ~ 0.15 dex ([Lehmer et al. 2021](#)). Those, our estimations support the metallicity evolution of the HMXB populations.

We do not detect a significant variation over metallicity for hot gas components. Further studies of the hot gas properties of star-forming galaxies are required to probe the possible metallicity evolution.

Chapter 6

Summary and Conclusion

The summary of the Chapter 2 is the following:

- Based on public *Chandra* archival data, we studied populations of soft and SSSs with the aim to investigate populations of stable nuclear burning, accreting WDs. To this end, we searched the Chandra data archive and constructed an optimal sample of galaxies for studying populations of stable nuclear burning, accreting WDs. We aimed to construct the best possible sample of such galaxies. We selected four late-type and five early-type galaxies with stellar masses $\gtrsim 10^{10} M_{\odot}$ and Chandra X-ray sensitivity limits comparable to or better than $\sim 10^{36}$ erg/s. Our selection presents a nearly full sample of galaxies available in the Chandra archive up to cycle 20 and suitable for such a study (among galaxies fitting within the field of view of Chandra observation).
- We proposed a new approach to identify the population of soft and SSSs based on combination of hardness ratio and median energy. The distributions of sources over median energy in late-type galaxies show a clear bi-modality with distinct populations of soft and super-soft sources. These sources show a rather compact distribution in the X-ray luminosity–temperature plane with temperatures of 20–300 eV and X-ray luminosities in the $10^{36} \sim 10^{38}$ erg/s range. The picture is more complex for lenticular and elliptical galaxies, where populations of soft sources smoothly connect to the populations of X-ray binaries and background AGNs in their median energy distributions. For these galaxies, we mainly used the lack of emission above 2 keV to select soft sources for detailed analysis.
- We used the X-ray luminosity–temperature diagram to further classify selected sources into super-soft and soft. To this end we used the theoretical boundary of stable hydrogen nuclear burning on the surface of accreting WDs to separate SSSs from the rest of the population of soft sources.
- In late-type galaxies, we found 29 super-soft sources which yields a specific frequency of $f_{\text{SSS}}^{\text{S}} \approx (2.08 \pm 0.46) \times 10^{-10} M_{\odot}^{-1}$. In lenticular and elliptical galaxies, there are seven

super-soft sources, giving a specific frequency of $f_{\text{SSS}}^{\text{E+S0}} \approx (2.47 \pm 1.34) \times 10^{-11} M_{\odot}^{-1}$. Specific frequencies in the late- and early-type galaxies differ with a statistical confidence of $\approx 5.8\sigma$. The ratio of specific frequencies of SSSs in the late- and early-type galaxies is $f_{\text{SSS}}^{\text{E+S0}}/f_{\text{SSS}}^{\text{S}} = 0.12 \pm 0.05$. Our results are broadly consistent with population synthesis modeling of the populations of stable nuclear burning, accreting WDs.

In Chapter 3, we studied the X-ray emission from historical CNe in our Galaxy. We used data from three SRG/eROSITA sky surveys in one half of the sky which is processed by the Russian SRG/eROSITA consortium. Our results can be summarized as follows:

- Out of the 309 known historical CNe (see Fig. 3.1, 3.2), X-ray emission was detected from 52 sources. Most of the sources are in quiescent phase — their X-ray emission is associated with the accretion of material in the binary system and is produced predominantly in the boundary layer near the WD surface and in the hot corona of the accretion disk. The X-ray luminosities in 0.3–2.3 keV band are $L_X \approx 10^{30} - 10^{34}$ erg/s.
- We analyzed in detail the spectra of the bright sources from which SRG/eROSITA recorded more than 50 counts (11 sources, see Fig. 3.3 and Table B.1). The bright sources can be divided by the properties of their spectra in the 0.3–7 keV energy band into two groups. For most (7 of the 11) sources, the spectra are best fitted by the isobaric cooling flow model with parameters typical for cataclysmic variables. For four sources, GK Per, V392 Per, X Ser, and V4743 Sgr, the isobaric cooling flow model is inapplicable. These sources have anomalously hard spectra with a photon index $\Gamma \sim 1$, whereas $\Gamma \sim 2-3$ for the seven sources mentioned above. Among these four sources, GK Per and V4743 Sgr, are an intermediate polar and a candidate for intermediate polars. We hypothesized that the two remaining sources could also be intermediate polars, but the available data are not enough to test this hypothesis.
- The averaged spectrum of the faint sources (having less than 50 counts in their spectra) in the 0.3–7 keV energy band is anomalously hard and is well fitted by a single component power-law model with a photon index $\Gamma = 0.96_{-0.17}^{+0.18}$ (see Fig. 3.4), resembling the spectra of intermediate polars. The interpretation of this result requires further observations, in particular, during future SRG/eROSITA sky surveys.
- In our sample of historical CNe, we found four sources with supersoft spectra from which there is no emission above ~ 1 keV. For two of them, V5558 Sgr and V3666 Oph, the parameters of the black body fit, in particular, the sizes of the emitting surface, suggest that we are dealing with the post-nova supersoft X-ray emission observed ≈ 13 and ≈ 1.6 years after the CN outburst. One source, V1500 Cyg, is a known polar, and the size of the emitting surface in its case is much smaller than the WD size and is close to the expected size of the circumpolar region of a magnetized WD. The fourth source, V5856 Sgr, has the same supersoft emission parameters, suggesting that it might also be a polar.

- A supersoft component with similar parameters is also detected in the spectrum of V2491 Cyg, along with a harder spectral component. As has already been proposed in earlier papers (see, e.g., [Zemko et al. 2015](#)), the parameters of the supersoft component also suggest that this source might be an intermediate polar.
- During the second sky survey, in November 2020, the SRG/eROSITA telescope observed a dwarf nova outburst in VY Aqr, which enters into our CN sample. By chance coincidence, the X-ray observations occurred at the peak of the optical light curve. We analyzed in detail the X-ray spectra of this source in its outburst and in quiescent phase.
- On the whole, our X-ray spectroscopy suggests that systems with magnetized WDs may account for some fraction in our sample of historical CNe detected in X-rays. This suggestion will be checked during further SRG/eROSITA sky surveys. More detailed optical studies of these sources are also of great importance.

The historical CNe represent a sample of bonafide accreting WD with unstable thermonuclear hydrogen burning on their surface. Their X-ray luminosities in quiescence are a good proxy for the accretion rate in a binary system. In Chapter 4, we have used this fact for the first time to construct the accretion rate distribution of WDs with non-steady hydrogen burning on their surface and compared it with the accretion rate distribution for steady supersoft sources, where hydrogen burning is steady. The derived distributions (see Fig. 4.1) occupy non-intersecting regions in accretion rate and quantitatively agree with the predictions of the theory of thermonuclear hydrogen burning on the WD surface.

In chapter 5 we study X-ray emission of accreting BH and NS and the hot ISM in star-forming galaxies. We construct the SRG/eROSITA–IRAS catalog of 1360 star-forming galaxies, which is about five times bigger than the samples used in previous studies. The majority of galaxies are moderately star-forming, with a median specific SFR of $6.3 \times 10^{-10} \text{ yr}^{-1}$ and the 90% quantile interval of $(0.2\text{--}1.4) \times 10^{-10} \text{ yr}^{-1}$. Based on the analysis of their X-ray spectra, we estimate the contribution of the nuclear activity and remove the galaxies containing a low luminosity AGN, where its contribution to the total X-ray output exceeded 26%. Using the SRG/eROSITA – IRAS sample of star-forming galaxies, we investigate the scaling relation between X-ray luminosity and SFR for HMXBs and hot ISM. The derived L_X –SFR scaling relation of star-forming galaxies is $L_{0.3\text{--}2.3 \text{ keV}}/\text{SFR} = 2.2 \times 10^{39} \text{ erg s}^{-1} (\text{M}_\odot \text{ yr}^{-1})^{-1}$ with the rms of 0.24 dex (see Table 5.2). We use our measurements and previous L_X/SFR measurements for HMXBs to investigate the metallicity dependence of L_X/SFR for HMXBs. Using the hot, diffuse gas component of the combined X-ray spectrum of galaxies, we constrained the metal abundances of Oxygen and Iron. For the Oxygen abundance, we obtain $12 + \log(\text{O}/\text{H})_{\text{fit}} = 8.8$, which is consistent with the median gas-phase metallicity of BPT star-forming galaxies ($12 + \log(\text{O}/\text{H}) \approx 8.7$). The $[\text{O}/\text{Fe}]$ ratio in the hot ISM of star-forming galaxies is consistent with the solar value confirming that metal enrichment of the ISM due to both core-collapse and type Ia supernovae.

Appendix A

Populations of super-soft X-ray sources in galaxies of different morphological types

A.1 Galaxy images

Fig. [A.1](#) shows X-ray images of galaxies in our sample and outlines of analysed regions.

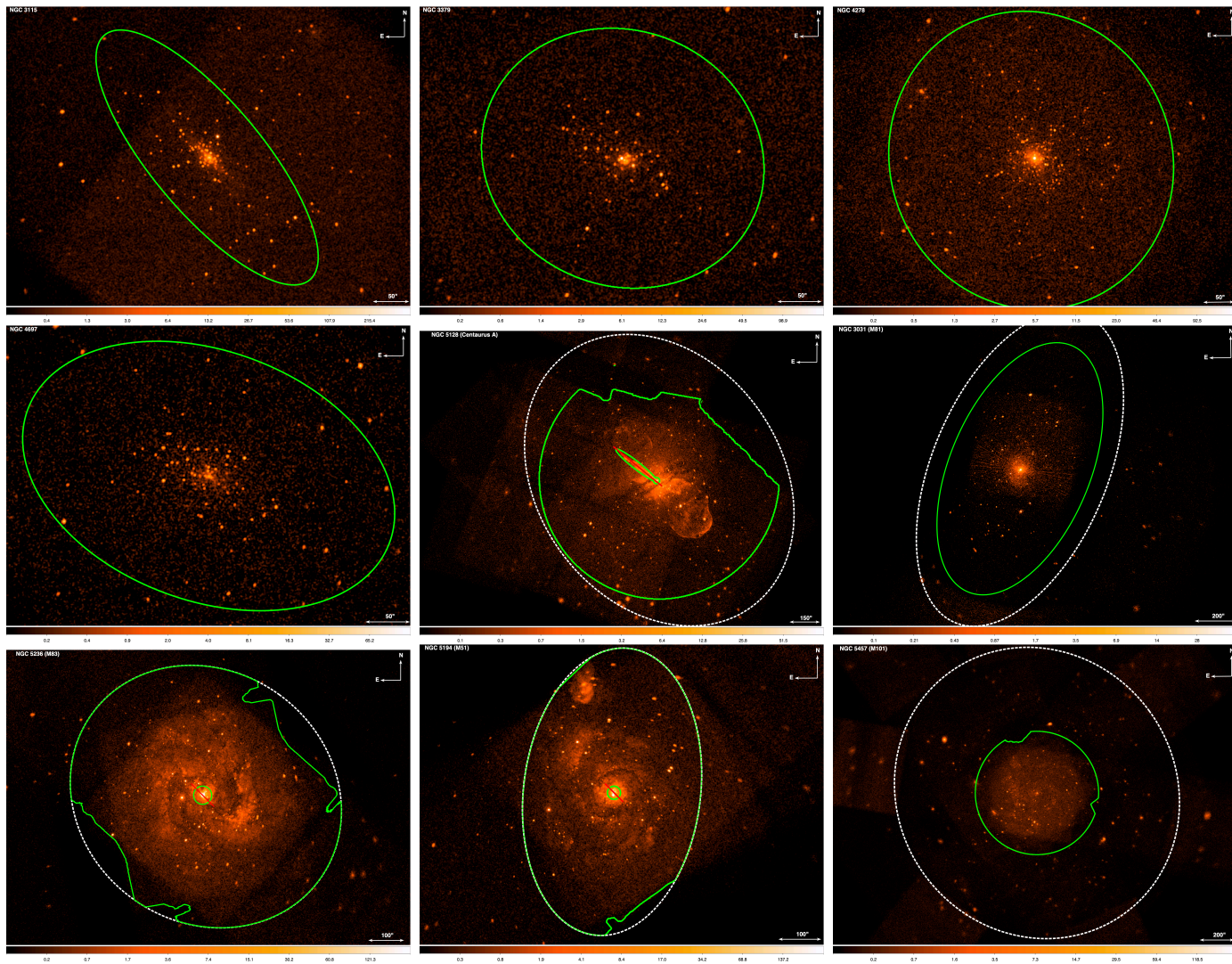


Figure A.1: The 0.3–2 keV band false-color images (smoothed) of galaxies in our sample. Dashed white regions correspond to D_{25} . Green lines show regions used for source detection having exposure map values greater than 20 % of maximal value (for more detail see Section 2.2.1). Stellar masses listed in Table 2 are computed for these regions. The inside areas of small green regions near the center of Centaurus A, M83 and M51 were excluded from analysis.

A.2 Catalog of super-soft X-ray sources

The catalog is comprised of SSSs with more than 20 counts (solid black line in Fig. 2.5.) The sources are classified as super-soft if they are located to the left of the stable nuclear burning boundary (nearly vertical solid red line in n Fig. 2.5) or their error bars cross this boundary. We also included two sources in M101, located outside but close to the stable nuclear burning boundary (the two sources in Fig.2.5 upper right panel with $kT \gtrsim 100$ eV and $L_X \gtrsim 10^{37}$ erg/s.). The catalog of super-soft X-ray sources is given in Table A.2.

Table A.1: List of *Chandra* observations used for the analysis.

Galaxy (1)	ObsID (2)	Date (3)	Exposure (ksec) (4)	Camera (5)
NGC 5236 (M83)	12992	04/09/2011	66.3	ACIS-S
	12993	15/03/2011	49.4	ACIS-S
	12994	23/03/2011	150.1	ACIS-S
	12995	23/12/2010	59.3	ACIS-S
	12996	29/03/2011	53.0	ACIS-S
	13202	25/12/2010	98.8	ACIS-S
	13241	18/03/2011	79.0	ACIS-S
	13248	18/03/2011	54.3	ACIS-S
	14332	29/08/2011	52.4	ACIS-S
	14342	28/12/2011	67.1	ACIS-S
NGC 5194 (M51)	13812	12/09/2012	157.5	ACIS-S
	13813	09/09/2012	179.2	ACIS-S
	13814	20/09/2012	189.8	ACIS-S
	13815	23/09/2012	67.2	ACIS-S
	13816	26/09/2012	73.1	ACIS-S
	15496	19/09/2012	41.0	ACIS-S
	15553	10/10/2012	37.6	ACIS-S
NGC 5457 (M101)	4731	19/01/2004	56.2	ACIS-S
	4732	19/03/2004	69.8	ACIS-S
	4733	07/05/2004	24.8	ACIS-S
	4734	11/07/2004	35.5	ACIS-S
	4735	12/09/2004	28.8	ACIS-S
	4736	01/11/2004	77.3	ACIS-S
	4737	01/01/2005	21.9	ACIS-S
	5296	21/01/2004	3.1	ACIS-S
	5297	24/01/2004	21.7	ACIS-S
	5300	07/03/2004	52.1	ACIS-S
	5309	14/03/2004	70.8	ACIS-S
	5322	03/05/2004	64.7	ACIS-S
	5323	09/05/2004	42.6	ACIS-S
	5337	05/07/2004	9.9	ACIS-S
	5338	06/07/2004	28.6	ACIS-S
	5339	07/07/2004	14.3	ACIS-S
5340	08/07/2004	54.4	ACIS-S	
6114	05/09/2004	66.2	ACIS-S	

	6115	08/09/2004	35.8	ACIS-S
	6118	11/09/2004	11.5	ACIS-S
	6152	07/11/2004	44.1	ACIS-S
	6169	30/12/2004	29.4	ACIS-S
	6170	22/12/2004	48.0	ACIS-S
	6175	24/12/2004	40.7	ACIS-S
NGC 3031 (M81)	5935	26/05/2005	11.0	ACIS-S
	5936	28/05/2005	11.4	ACIS-S
	5937	01/06/2005	12.0	ACIS-S
	5938	03/06/2005	11.8	ACIS-S
	5939	06/06/2005	11.8	ACIS-S
	5940	09/06/2005	12.0	ACIS-S
	5941	11/06/2005	11.8	ACIS-S
	5942	15/06/2005	11.9	ACIS-S
	5943	18/06/2005	12.0	ACIS-S
	5944	21/06/2005	11.8	ACIS-S
	5945	24/06/2005	11.6	ACIS-S
	5946	26/06/2005	12.0	ACIS-S
	5947	29/06/2005	10.7	ACIS-S
	5948	03/07/2005	12.0	ACIS-S
	5949	06/07/2005	12.0	ACIS-S
NGC 5128 (Cen A)	7797	22/03/2007	96.9	ACIS-I
	7798	27/03/2007	90.8	ACIS-I
	7799	30/03/2007	94.8	ACIS-I
	7800	17/04/2007	90.8	ACIS-I
	8489	08/05/2007	93.9	ACIS-I
	8490	30/05/2007	94.4	ACIS-I
NGC 3115	13817	18/01/2012	172.0	ACIS-S
	13819	26/01/2012	75.5	ACIS-S
	13820	31/01/2012	184.2	ACIS-S
	13821	03/02/2012	158.0	ACIS-S
	13822	21/01/2012	160.2	ACIS-S
	14383	04/04/2012	119.5	ACIS-S
	14384	06/04/2012	69.7	ACIS-S
	14419	05/04/2012	46.3	ACIS-S
NGC 3379	7073	23/01/2006	84.1	ACIS-S
	7074	09/04/2006	69.1	ACIS-S
	7075	07/03/2006	83.1	ACIS-S
	7076	10/01/2007	69.2	ACIS-S
NGC 4278	7077	16/03/2006	110.3	ACIS-S
	7078	25/07/2006	51.4	ACIS-S
	7079	24/10/2006	105.1	ACIS-S
	7080	20/04/2007	55.8	ACIS-S
	7081	20/02/2007	110.7	ACIS-S
NGC 4697	4727	26/12/2003	39.9	ACIS-S
	4728	06/01/2004	35.7	ACIS-S
	4729	12/02/2004	38.1	ACIS-S
	4730	18/08/2007	40.0	ACIS-S

Table A.2: List of super-soft X-ray sources.

ID	GALAXY	R.A.	DEC.	Counts _{0.3-2}	Bkg _{0.3-2}	Rate _{0.3-2}	N _H	kT _{bb}	L _X ^{0.3-2}
(1)	(2)	(3)	(4)	(5)	(6)	(7)	(8)	(9)	(10)
						(10 ⁻⁴ cnt/s)	(10 ²¹ cm ⁻²)	(eV)	(10 ³⁷ erg/s)
1	M81	09 55 42.14	+69 03 36.40	2565.0 ± 51.7	8.7 ± 0.9	145.30 ± 2.94	1.19	85 ⁺² ₋₁	15.87 ^{+0.34} _{-0.32}
2	M81	09 56 8.98	+69 01 6.79	360.0 ± 20.0	1.6 ± 0.5	20.37 ± 1.14	1.39	86 ⁺⁴ ₋₃	7.04 ^{+0.48} _{-0.46}
3	NGC3379	10 47 47.23	+12 34 59.78	72.0 ± 9.5	0.5 ± 0.3	3.03 ± 0.40	0.26	100 ⁺¹⁸ ₋₁₃	3.68 ^{+0.46} _{-0.42}
4	NGC4278	12 19 56.67	+29 16 31.08	20.0 ± 5.6	1.6 ± 0.5	0.42 ± 0.13	0.20	65 ⁺¹⁸ ₋₁₃	2.76 ^{+0.82} _{-0.63}
5	NGC4278	12 20 12.43	+29 17 41.86	25.0 ± 6.1	1.3 ± 0.4	0.55 ± 0.14	0.20	72 ⁺¹⁸ ₋₁₃	2.26 ^{+0.64} _{-0.50}
6	NGC4697	12 48 34.55	-5 47 49.34	36.0 ± 7.1	0.8 ± 0.3	2.29 ± 0.46	0.21	102 ⁺²⁴ ₋₁₅	2.79 ^{+0.58} _{-0.47}
7	NGC4697	12 48 41.28	-5 48 19.73	24.0 ± 6.0	0.2 ± 0.2	1.55 ± 0.39	0.21	70 ⁺²³ ₋₁₂	2.41 ^{+0.63} _{-0.52}
8	CenA	13 25 14.60	-42 56 11.57	83.0 ± 10.2	19.3 ± 1.4	2.28 ± 0.37	0.24	79 ⁺⁹ ₋₈	2.60 ^{+0.56} _{-0.47}
9	CenA	13 25 18.14	-43 03 42.53	100.0 ± 11.0	27.8 ± 1.7	1.29 ± 0.20	0.24	73 ⁺⁷ ₋₆	2.06 ^{+0.43} _{-0.36}
10	M51	13 29 41.23	+47 11 15.57	48.0 ± 8.0	16.1 ± 1.2	0.43 ± 0.11	0.92	33 ⁺²⁰ ₋₈	1.27 ^{+0.56} _{-0.39}
11	M51	13 29 46.00	+47 10 56.36	55.0 ± 8.5	9.5 ± 1.0	0.61 ± 0.11	0.69	67 ⁺¹³ ₋₁₃	0.96 ^{+0.19} _{-0.16}
12	M51	13 29 51.69	+47 12 3.82	86.1 ± 10.3	56.9 ± 2.3	0.39 ± 0.14	3.93	62 ⁺²⁸ ₋₃₂	0.29 ^{+0.09} _{-0.10}
13	M51	13 29 54.02	+47 11 25.68	64.0 ± 9.0	15.4 ± 1.2	0.65 ± 0.12	2.89	40 ⁺¹² ₋₁₆	0.57 ^{+0.12} _{-0.12}
14	M51	13 29 54.99	+47 12 4.74	62.0 ± 8.9	16.0 ± 1.3	0.62 ± 0.12	2.92	76 ⁺¹⁴ ₋₁₂	0.53 ^{+0.09} _{-0.09}
15	M83	13 36 52.45	-29 52 52.09	242.0 ± 16.6	113.3 ± 3.2	1.76 ± 0.23	5.40	53 ⁺⁷ ₋₈	0.42 ^{+0.05} _{-0.05}
16	M83	13 36 52.66	-29 49 37.45	67.0 ± 9.2	9.1 ± 1.0	0.79 ± 0.13	1.32	35 ⁺⁴ ₋₆	0.87 ^{+0.18} _{-0.15}
17	M83	13 36 53.97	-29 50 32.52	40.0 ± 7.4	14.3 ± 1.2	0.35 ± 0.10	3.60	33 ⁺⁶ ₋₉	0.19 ^{+0.04} _{-0.05}
18	M83	13 36 56.45	-29 52 57.25	50.0 ± 8.1	21.3 ± 1.5	0.39 ± 0.11	5.00	26 ⁺⁴ ₋₇	0.20 ^{+0.04} _{-0.05}
19	M83	13 36 56.77	-29 53 16.20	95.0 ± 10.8	22.5 ± 1.5	0.99 ± 0.15	3.39	46 ⁺⁶ ₋₆	0.35 ^{+0.05} _{-0.05}
20	M83	13 36 58.62	-29 51 56.84	88.0 ± 10.4	49.2 ± 2.1	0.53 ± 0.15	10.41	74 ⁺¹⁵ ₋₂₂	0.11 ^{+0.02} _{-0.03}
21	M83	13 36 58.64	-29 53 38.86	87.0 ± 10.4	30.6 ± 1.7	0.77 ± 0.14	1.82	30 ⁺⁵ ₋₇	0.69 ^{+0.15} _{-0.13}

22	M83	13 36 59.04	-29 52 18.07	50.0 ± 8.1	22.5 ± 1.5	0.38 ± 0.11	11.69	71_{-18}^{+12}	$0.09_{-0.02}^{+0.02}$
23	M83	13 36 59.25	-29 51 43.82	85.0 ± 10.3	49.4 ± 2.2	0.49 ± 0.14	9.95	69_{-20}^{+12}	$0.11_{-0.03}^{+0.02}$
24	M83	13 36 59.34	-29 53 17.90	49.0 ± 8.1	19.1 ± 1.3	0.41 ± 0.11	2.50	65_{-18}^{+15}	$0.12_{-0.03}^{+0.03}$
25	M83	13 37 0.45	-29 50 54.02	173.0 ± 14.2	9.1 ± 1.0	2.25 ± 0.19	4.05	28_{-3}^{+3}	$1.13_{-0.10}^{+0.10}$
26	M83	13 37 3.86	-29 52 23.02	41.0 ± 7.5	10.8 ± 1.0	0.41 ± 0.10	4.36	42_{-8}^{+7}	$0.18_{-0.04}^{+0.03}$
27	M83	13 37 5.53	-29 50 32.24	34.0 ± 6.9	6.0 ± 0.8	0.42 ± 0.10	3.01	42_{-13}^{+8}	$0.21_{-0.05}^{+0.05}$
28	M83	13 37 18.55	-29 52 7.59	29.0 ± 6.5	10.6 ± 1.0	0.25 ± 0.09	1.57	71_{-23}^{+16}	$0.12_{-0.03}^{+0.04}$
29	M101	14 02 51.34	+54 19 18.24	178.0 ± 14.4	14.7 ± 1.2	2.02 ± 0.18	1.50	85_{-5}^{+6}	$0.91_{-0.07}^{+0.08}$
30	M101	14 02 51.64	+54 22 3.97	33.0 ± 6.8	10.5 ± 1.0	0.28 ± 0.08	1.17	70_{-17}^{+24}	$0.13_{-0.03}^{+0.03}$
31	M101	14 03 1.22	+54 23 41.41	324.0 ± 19.0	13.3 ± 1.1	3.83 ± 0.23	1.13	66_{-3}^{+3}	$1.85_{-0.11}^{+0.12}$
32	M101	14 03 12.75	+54 21 11.52	38.0 ± 7.2	13.1 ± 1.1	0.28 ± 0.08	1.99	73_{-14}^{+18}	$0.10_{-0.02}^{+0.02}$
33	M101	14 03 13.65	+54 20 9.39	700.0 ± 27.5	10.9 ± 1.0	7.24 ± 0.29	1.57	53_{-2}^{+2}	$3.17_{-0.13}^{+0.13}$
34	M101	14 03 15.52	+54 17 3.81	339.0 ± 19.4	30.7 ± 1.7	3.24 ± 0.20	2.52	104_{-5}^{+5}	$1.24_{-0.07}^{+0.07}$
35	M101	14 03 16.52	+54 20 54.80	44.0 ± 7.7	12.5 ± 1.1	0.34 ± 0.08	1.85	66_{-11}^{+14}	$0.16_{-0.03}^{+0.03}$
36	M101	14 03 19.02	+54 17 19.48	254.0 ± 17.0	33.5 ± 1.8	2.32 ± 0.18	1.40	61_{-4}^{+4}	$1.32_{-0.09}^{+0.10}$
37	M101	14 03 27.38	+54 21 11.62	109.0 ± 11.5	24.4 ± 1.5	0.89 ± 0.12	1.67	27_{-3}^{+4}	$0.83_{-0.11}^{+0.12}$
38	M101	14 03 29.91	+54 20 57.27	259.0 ± 17.1	16.7 ± 1.3	2.54 ± 0.18	1.81	64_{-3}^{+4}	$1.15_{-0.08}^{+0.08}$
39	M101	14 03 33.35	+54 17 59.73	433.0 ± 21.8	22.2 ± 1.4	4.32 ± 0.23	2.24	60_{-2}^{+3}	$2.62_{-0.14}^{+0.14}$

Description of columns: (1) Source ID; (2) Galaxy name; (3) Right ascension (J2000); (4) Declination (J2000); (5) Counts in the source region in the 0.3–2 keV band and its 1σ error (68%); (6) Background counts in the source region in 0.3–2 keV band and its 1σ error; (7) Source count rate in 0.3–2 keV band; (8) Absorption column density in units of 10^{21} cm^{-2} obtained by combining CO 2-1 and 21 cm data as described in Section 2.4.1; (9) best fit color temperature in units of eV; (10) absorbed X-ray luminosity in the 0.3–2 keV band in units of $10^{37} \text{ erg s}^{-1}$. Parameters given in columns (9) and (10) were obtained by approximating spectra with the black body model with absorption fixed at the value from column (8).

Appendix B

**X-ray observations of historical
classical nova counterparts with
eROSITA telescope aboard SRG
orbital observatory during the all-sky
survey**

Table B.1: Best fits results of the X-ray spectra of the bright CN counterparts from which the SRG/eROSITA telescope detected more than 50 counts.

<i>Models</i>	V603 Aql	GK Per	WZ Sge	V2487 Oph	V392 Per	V2491 Cyg	WX Cet	DK Lac	X Ser	V4743 Sgr	VY Aqr (quiescence)	VY Aqr (outburst)
<i>tbabs</i> × <i>power-law</i>												
N_H [$\times 10^{21}$ cm $^{-2}$]	1.52 ± 0.28	$2.51^{+0.57}_{-0.52}$	$0.41^{+0.34}_{-0.31}$	$1.57^{+0.62}_{-0.52}$	1.37 ± 0.71	$0.91^{+0.93}_{-0.73}$	$1.01^{+0.99}_{-0.75}$	$4.30^{+3.98}_{-2.78}$	≤ 5.04	≤ 2.34	≤ 1.1	0.96 ± 0.30
Γ	2.27 ± 0.17	1.01 ± 0.19	$1.80^{+0.24}_{-0.26}$	$2.26^{+0.42}_{-0.34}$	0.96 ± 0.26	$3.20^{+0.99}_{-0.76}$	$2.45^{+0.71}_{-0.59}$	$2.70^{+2.01}_{-1.32}$	$1.15^{+1.82}_{-1.25}$	$1.20^{+1.36}_{-0.48}$	$1.59^{+0.53}_{-0.38}$	2.61 ± 0.24
<i>C</i> – <i>stat/d.o.f.</i>	317.8/248	252.0/199	126.2/138	143.6/119	84.1/72	89.9/50	42.2/45	23.8/26	12.8/18	18.7/18	31.6/22	141.7/108
α (goodness)	$\leq 10^{-5}$	10^{-2}	0.57	$\leq 10^{-5}$	0.32	$\leq 10^{-5}$	0.54	0.35	0.73	0.48	0.11	$\leq 10^{-5}$
<i>AIC</i>	323.8	258.0	132.2	149.6	90.2	95.9	48.2	29.8	18.8	24.7	37.6	147.7
$\log(L_X^{pw}$ [erg/s]) ^a	$32.37^{+0.06}_{-0.04}$	32.50 ± 0.04	30.00 ± 0.03	$35.54^{+0.13}_{-0.08}$	$33.81^{+0.10}_{-0.09}$	$34.46^{+0.50}_{-0.34}$	$30.25^{+0.28}_{-0.15}$	$32.73^{+0.84}_{-0.41}$	$33.09^{+0.30}_{-0.15}$	33.13 ± 0.16	$30.08^{+0.14}_{-0.09}$	$31.07^{+0.16}_{-0.12}$
<i>tbabs</i> × <i>meka</i>												
N_H [$\times 10^{21}$ cm $^{-2}$]	$0.89^{+0.09}_{-0.15}$	3.30 ± 0.21	≤ 0.02	0.71 ± 0.20	$2.35^{+0.38}_{-0.36}$	≤ 0.40	≤ 1.37	$2.96^{+1.56}_{-1.34}$	5.50	≤ 0.10	≤ 0.87	0.45 ± 0.15
kT [keV]	$2.02^{+0.30}_{-0.21}$	10*	$4.62^{+1.37}_{-1.58}$	$3.05^{+1.53}_{-0.64}$	10*	$0.97^{+0.28}_{-0.22}$	$1.37^{+0.61}_{-0.30}$	$1.67^{+5.53}_{-0.88}$	$1.52^{+1.10}_{-0.50}$	10*	$1.36^{+1.41}_{-0.29}$	$0.80^{+0.09}_{-0.06}$
Z [Z_\odot]	≤ 0.02	≤ 2	$0.40^{+0.61}_{-0.37}$	≤ 0.1	≤ 3.2	$\leq 5 \times 10^{-3}$	$0.16^{+0.27}_{-0.11}$	≤ 0.2	≤ 0.14	≤ 2	$0.38^{+0.87}_{-0.24}$	$0.06^{+0.03}_{-0.02}$
<i>C</i> – <i>stat/d.o.f.</i>	314.2/247	264.4/199	125.8/137	154.6/118	90.0/72	106.5/49	36.8/44	24.4/25	14.7/17	18.8/18	26.6/21	126.4/107
α (goodness)	$\leq 10^{-5}$	9×10^{-3}	0.58	10^{-2}	0.12	$\leq 10^{-5}$	0.68	0.67	0.56	0.43	0.08	0.11
<i>AIC</i>	322.2	272.4	133.8	162.6	95.0	114.5	44.8	32.4	22.7	26.8	34.6	134.4
$\log(L_X^{meka}$ [erg/s]) ^a	$32.29^{+0.01}_{-0.02}$	32.52 ± 0.03	30.00 ± 0.07	35.49 ± 0.04	33.80 ± 0.06	$34.30^{+0.05}_{-0.04}$	30.12 ± 0.08	$32.54^{+0.22}_{-0.10}$	33.10 ± 0.08	33.13 ± 0.10	29.92 ± 0.10	30.96 ± 0.04
<i>tbabs</i> × <i>mckflow</i>												
N_H [$\times 10^{21}$ cm $^{-2}$]	0.73 ± 0.13		≤ 0.02	≤ 0.13		≤ 0.29	≤ 0.27	$2.93^{+1.23}_{-0.86}$			≤ 0.37	≤ 0.2
kT_{min} [keV]	≤ 0.19		≤ 1.06	≤ 0.92		≤ 0.25	$8^* \times 10^{-3}$	≤ 0.91			$0.95^{+1.29}_{-0.75}$	≤ 0.31
kT_{max} [keV]	$6.97^{+1.53}_{-1.30}$		$17.20^{+20.33}_{-6.94}$	$24.72^{+22.63}_{-9.91}$		$1.98^{+0.93}_{-0.70}$	$6.37^{+2.71}_{-2.51}$	$5.15^{+18.69}_{-2.69}$			$5.14^{+8.35}_{-3.29}$	$2.91^{+0.45}_{-0.40}$
Z [Z_\odot]	$0.19^{+0.10}_{-0.08}$		$0.32^{+0.34}_{-0.19}$	≤ 0.21		$\leq 3 \times 10^{-3}$	$0.55^{+0.59}_{-0.41}$	≤ 0.35			1*	$0.24^{+0.09}_{-0.08}$
\dot{M}_{acc} [$\times 10^{-12}$ M_\odot /yr]	$53.3^{+15.2}_{-9.8}$		$11.0^{+5.0}_{-3.9} \times 10^{-2}$	$3.1^{+1.1}_{-1.0} \times 10^4$		$2.3^{+2.3}_{-0.8} \times 10^4$	$0.4^{+0.2}_{-0.1}$	$135.1^{+983.1}_{-135.1}$			$0.5^{+1.6}_{-0.3}$	$6.6^{+2.3}_{-0.9}$
<i>C</i> – <i>stat/d.o.f.</i>	287.9/246		123.5/137	113.5/116		101.6/49	37.3/44	23.3/24			24.6/21	109.6/107
α (goodness)	0.11		0.54	0.21		$\leq 10^{-5}$	0.66	0.55			0.19	0.45
<i>AIC</i>	297.9		131.5	123.52		101.6	45.3	33.3			31.7	119.6
$\log(L_X^{mckflow}$ [erg/s]) ^a	32.23 ± 0.02		29.86 ± 0.05	35.45 ± 0.06		34.20 ± 0.04	30.09 ± 0.07	$32.49^{+0.33}_{-0.11}$			$29.97^{+0.13}_{-0.11}$	$30.91^{+0.04}_{-0.03}$
<i>tbabs</i> × (<i>bbody</i> + <i>meka</i>)												
N_H [$\times 10^{21}$ cm $^{-2}$]				$4.25^{+1.53}_{-1.41}$		$3.61^{+1.24}_{-1.55}$						
kT_{BB} [eV]				96^{+21}_{-14}		65^{+11}_{-9}						
kT_{meka} [keV]				$6.7^{+48.8}_{-2.7}$		10*						
Z [Z_\odot]				1*		1*						

$C - stat/d.o.f.$	116.7/117	44.9/49
$\alpha(\text{goodness})$	0.82	0.67
AIC	127.0	52.9
$\log(L_{bol}^{BB} [\text{erg/s}])^a$	36.31 ± 0.61	$36.05^{+0.81}_{-0.73}$
$\log(L_X^{mekal} [\text{erg/s}])^a$	35.54 ± 0.12	34.41 ± 0.12
R_{BB} [km]	439^{+618}_{-289}	700^{+1552}_{-458}

Notes: * – The parameter was fixed at a given value. (a) Absorption corrected X-ray luminosity in the 0.3-8 keV energy band. Distances from Table B.2 were used to calculate luminosities. Error bars show 1σ confidence limits.

Table B.2: List of X-ray sources from the SRG/eROSITA catalog having identifications with CNe in our Galaxy.

N _e	Date	Nova	RA	DEC	$R_{\text{err}}(98\%)$	SRGe	"	$N_{\text{H,Gal}}$	E(B-V)	d	M_{WD}	L_X	L_X^0
(1)	(2)	(3)	($^{\circ}$)	($^{\circ}$)	(")	(7)	(8)	(10^{21} cm^{-2})	(10)	(kpc)	(M_{\odot})	(erg/s)	(erg/s)
1	12/06/2021 (1)	V1674 Her	284.37953	16.89338	6.87	J185731.1+165336	2.29	2.99	0.72 (1)	–	–	$(2.2 \pm 0.6) \times 10^{31}$	$(4.8 \pm 1.2) \times 10^{31}$
2	18/03/2021 (2)	V1405 Cas	351.20222	61.18732	9.88	J232448.5+611114	4.42	7.07	0.56 ± 0.02 (3)	1.73 ± 0.01 (G)	–	$(6.1 \pm 2.4) \times 10^{30}$	$(1.2 \pm 0.5) \times 10^{31}$
3	29/10/2019 (4)	V659 Sct	279.99787	-10.42678	6.04	J183959.5-102536	6.26	5.37	0.9 (5)	1.97 ± 0.66 (G)	–	$(7.8 \pm 1.6) \times 10^{31}$	$(1.9 \pm 0.4) \times 10^{32}$
4	27/08/2019 (6)	V3890 Sgr	277.68084	-24.01880	13.80	J183043.4-240108	10.92	1.64	0.57 (7)	4.5 (7)	1.3 (a)	$(2.0 \pm 0.6) \times 10^{32}$	$(3.9 \pm 1.2) \times 10^{32}$
5	08/08/2018 (8)	V3666 Oph	265.60063	-20.88580	9.67	J174224.2-205309	1.14	2.88	0.98 (9)	–	–	$(1.5 \pm 0.5) \times 10^{31}$	$(3.8 \pm 1.2) \times 10^{31}$
6	29/04/2018 (10)	V392 Per	70.84108	47.35684	3.37	J044321.9+472125	1.88	5.82	0.72 (11)	3.88 (11)	1.21 (b)	$(1.3 \pm 0.1) \times 10^{33}$	$(2.8 \pm 0.2) \times 10^{33}$
7	19/06/2017 (12)	V612 Sct	277.94124	-14.31627	8.41	J183145.9-141859	2.38	4.37	0.68 (13)	3.99 ± 1.0 (14)	–	$(1.9 \pm 0.5) \times 10^{32}$	$(3.9 \pm 1.1) \times 10^{32}$
8	25/10/2016 (15)	V5856 Sgr	275.22035	-28.37153	7.19	J182052.9-282218	11.59	1.43	0.34 (16)	4.2 (16)	–	$(2.9 \pm 0.6) \times 10^{32}$	$(4.7 \pm 1.0) \times 10^{32}$
9	14/08/2013 (17)	V339 Del	305.87688	20.76760	6.20	J202330.5+204603	1.98	1.30	0.18 (18)	4.5 ± 0.8 (18)	–	$(2.8 \pm 0.6) \times 10^{32}$	$(3.8 \pm 0.8) \times 10^{32}$
10	08/05/2012 (19)	V5590 Sgr	272.76528	-27.29020	8.69	J181103.7-271725	5.57	2.47	–	–	–	$(3.0 \pm 0.8) \times 10^{31}$	$(4.9 \pm 1.3) \times 10^{31}$
11	07/11/2011 (20)	V965 Per	47.81798	37.08439	12.56	J031116.3+370504	2.37	1.09	–	–	–	$(5.2 \pm 2.4) \times 10^{30}$	$(6.8 \pm 3.2) \times 10^{30}$
12	10/04/2008 (21)	V2491 Cyg	295.75797	32.31973	3.52	J194301.9+321911	1.08	3.96	0.45 (22)	15.9 (22)	1.35 (c)	$(1.3 \pm 0.1) \times 10^{34}$	$(2.3 \pm 0.2) \times 10^{34}$
13	14/04/2007 (23)	V5558 Sgr	272.57574	-18.78132	6.79	J181018.2-184653	1.03	14.81	0.8 (24)	1.3 ± 0.3 (25)	0.6 \pm 0.03 (d)	$(2.8 \pm 0.6) \times 10^{31}$	$(6.2 \pm 1.4) \times 10^{31}$
14	15/03/2007 (26)	V2467 Cyg	307.05124	41.80980	7.76	J202812.3+414835	1.85	12.52	1.5 (27)	3.1 ± 0.5 (28)	1.04 \pm 0.07 (e)	$(1.3 \pm 0.3) \times 10^{32}$	$(4.1 \pm 0.9) \times 10^{32}$
15	12/02/2006 (29)	RS Oph	267.55374	-6.70904	7.08	J175012.9-064233	3.92	2.08	0.73 (30)	1.6 ± 0.3 (31)	1.35 (c)	$(2.8 \pm 0.7) \times 10^{31}$	$(6.1 \pm 1.4) \times 10^{31}$
16	20/09/2002 (32)	V4743 Sgr	285.28921	-22.00149	4.93	J190109.4-220005	1.71	1.02	0.25 (33)	3.9 ± 0.3 (33)	1.15 \pm 0.06 (e)	$(4.8 \pm 0.7) \times 10^{32}$	$(6.9 \pm 1.0) \times 10^{32}$
17	15/06/1998 (34)	V2487 Oph	262.99910	-19.23298	2.89	J173159.8-191359	1.63	2.03	0.38 (35)	27.5 ± 3.0 (35)	1.35 \pm 0.01 (f)	$(1.4 \pm 0.1) \times 10^{35}$	$(2.4 \pm 0.1) \times 10^{35}$
18	19/02/1992 (36)	V1974 Cyg	307.62953	52.62978	7.79	J203031.1+523747	2.45	2.96	0.36 (30)	1.8 ± 0.1 (30)	–	$(1.3 \pm 0.4) \times 10^{31}$	$(2.1 \pm 0.7) \times 10^{31}$
19	21/03/1988 (37)	PQ And	37.37428	40.04330	6.15	J022929.8+400236	4.18	0.52	–	0.27 ± 0.02 (G)	–	$(8.0 \pm 1.5) \times 10^{29}$	$(9.3 \pm 1.8) \times 10^{29}$
20	21/10/1976 (38)	NQ Vul	292.31150	20.46575	10.46	J192914.8+202757	4.23	10.07	0.92 ± 0.2 (39)	1.6 ± 0.8 (40)	–	$(1.5 \pm 0.5) \times 10^{31}$	$(3.7 \pm 1.3) \times 10^{31}$
21	29/08/1975 (41)	V1500 Cyg	317.90211	48.15137	6.06	J211136.5+480905	4.14	8.76	0.45 (22)	1.5 (22)	1.2 (c)	$(2.9 \pm 0.6) \times 10^{31}$	$(5.1 \pm 1.1) \times 10^{31}$
22	10/07/1971 (42)	IV Cep	331.15760	53.50736	11.10	J220437.8+533027	8.71	5.42	0.65 (22)	3.1 (22)	0.98 (c)	$(2.3 \pm 0.9) \times 10^{31}$	$(4.6 \pm 1.9) \times 10^{31}$
23	15/04/1968 (C)	LV Vul	297.00245	27.17116	8.24	J194800.6+271016	2.69	9.62	0.6 (22)	1.0 (22)	0.98 (c)	$(1.2 \pm 0.3) \times 10^{31}$	$(2.3 \pm 0.5) \times 10^{31}$
24	08/07/1967 (43)	HR Del	310.58375	19.15977	7.99	J204220.1+190935	3.59	0.71	0.17 ± 0.02 (44)	0.96 ± 0.03 (G)	0.67 \pm 0.08 (g)	$(5.6 \pm 1.8) \times 10^{30}$	$(7.4 \pm 2.4) \times 10^{30}$
25	04/11/1964 (C)	QZ Aur	82.14550	33.30623	9.89	J052834.9+331822	8.20	4.84	0.55 (45)	2.87 ± 0.89 (G)	–	$(2.9 \pm 1.3) \times 10^{31}$	$(5.5 \pm 2.4) \times 10^{31}$
26	14/09/1963 (C)	AS Psc	22.03717	31.24893	16.82	J012808.9+311456	13.98	0.50	–	–	–	$(5.0 \pm 2.1) \times 10^{30}$	$(5.7 \pm 2.5) \times 10^{30}$

27	01/09/1963 (C)	WX Cet	19.26751	-17.93925	3.55	J011704.2-175621	1.82	0.15	-	0.13 (46)	-	$(8.6 \pm 0.8) \times 10^{29}$	$(9.0 \pm 0.8) \times 10^{29}$
28	06/02/1963 (C)	V533 Her	273.58518	41.85650	6.55	J181420.4+415123	4.95	0.35	0.03 ± 0.02 (44)	1.28 (22)	1.03 (c)	$(1.8 \pm 0.3) \times 10^{31}$	$(1.9 \pm 0.3) \times 10^{31}$
29	07/03/1960 (C)	V446 Her	284.34060	13.24122	7.75	J185721.7+131428	3.10	3.92	0.38 ± 0.04 (44)	1.38 (22)	0.98 (c)	$(2.3 \pm 0.5) \times 10^{31}$	$(3.8 \pm 0.8) \times 10^{31}$
30	21/02/1952 (C)	V1175 Sgr	273.57256	-31.12224	11.16	J181417.4-310720	14.67	1.57	0.29 (47)	5.2 (47)	-	$(1.3 \pm 0.5) \times 10^{32}$	$(1.9 \pm 0.8) \times 10^{32}$
31	14/11/1950 (C)	V630 Cas	357.21651	51.46181	5.93	J234852.0+512743	1.19	1.48	-	3.47 ± 0.63 (G)	-	$(1.1 \pm 0.2) \times 10^{32}$	$(1.5 \pm 0.3) \times 10^{32}$
32	23/01/1950 (C)	DK Lac	342.44570	53.28933	4.80	J224947.0+531722	1.77	2.70	0.22 ± 0.06 (44)	2.48 ± 0.43 (G)	-	$(1.0 \pm 0.1) \times 10^{32}$	$(1.4 \pm 0.2) \times 10^{32}$
33	18/06/1936 (C)	CP Lac	333.92164	55.61772	5.37	J221541.2+553704	1.74	5.84	0.28 ± 0.06 (44)	1.16 ± 0.06 (G)	-	$(1.4 \pm 0.2) \times 10^{31}$	$(2.1 \pm 0.3) \times 10^{31}$
34	12/12/1934 (C)	DQ Her	271.87469	45.85761	7.01	J180729.9+455127	4.00	0.32	0.05 ± 0.02 (44)	0.39 ± 0.03 (14)	-	$(1.3 \pm 0.2) \times 10^{30}$	$(1.4 \pm 0.3) \times 10^{30}$
35	01/01/1929 (C)	BC Cas	357.82628	60.30350	6.26	J235118.3+601813	5.50	6.31	-	2.04 ± 0.29 (G)	-	$(3.0 \pm 0.6) \times 10^{31}$	$(7.3 \pm 1.5) \times 10^{31}$
36	30/07/1927 (C)	EL Aql	284.00943	-3.32041	15.63	J185602.3-031913	9.36	5.72	1.11 (48)	-	-	$(8.8 \pm 4.3) \times 10^{30}$	$(2.4 \pm 1.2) \times 10^{31}$
37	14/06/1926 (C)	KY Sgr	270.33869	-26.41412	6.96	J180121.3-262451	12.69	5.48	-	5.3 (47)	-	$(5.2 \pm 1.1) \times 10^{32}$	$(1.2 \pm 0.2) \times 10^{33}$
38	20/08/1920 (C)	V476 Cyg	299.60098	53.61866	10.38	J195824.2+533707	3.00	1.77	0.19 (47)	1.8 (47)	-	$(4.8 \pm 2.3) \times 10^{30}$	$(6.6 \pm 3.1) \times 10^{30}$
39	11/03/1919 (C)	V1017 Sgr	278.01815	-29.38733	7.58	J183204.4-292314	1.50	1.27	0.39 ± 0.03 (14)	1.27 ± 0.07 (G)	-	$(2.1 \pm 0.5) \times 10^{31}$	$(3.5 \pm 0.9) \times 10^{31}$
40	08/06/1918 (C)	V603 Aql	282.22782	0.58420	2.67	J184854.7+003503	2.21	14.39	0.08 ± 0.02 (44)	0.31 ± 0.01 (G)	1.2 ± 0.1 (g)	$(1.1 \pm 0.2) \times 10^{32}$	$(1.3 \pm 0.3) \times 10^{32}$
41	22/11/1913 (C)	WZ Sge	301.90201	17.70392	2.92	J200736.5+174214	5.64	2.01	-	0.04 ± 0.0 (49)	0.85 ± 0.04 (h)	$(4.7 \pm 0.2) \times 10^{29}$	$(7.2 \pm 0.3) \times 10^{29}$
42	30/12/1910 (C)	DI Lac	338.95185	52.71758	8.21	J223548.4+524303	2.68	3.26	0.26 ± 0.04 (44)	1.64 ± 0.06 (G)	0.68 ± 0.12 (g)	$(1.3 \pm 0.3) \times 10^{31}$	$(2.0 \pm 0.5) \times 10^{31}$
43	21/03/1910 (C)	V999 Sgr	270.02649	-27.55126	9.73	J180006.4-273305	14.24	4.62	0.58 (47)	2.6 (47)	-	$(3.2 \pm 1.3) \times 10^{31}$	$(6.2 \pm 2.5) \times 10^{31}$
44	12/08/1907 (C)	VY Aqr	318.03833	-8.82741	2.82	J211209.2-084939	4.44	0.59	-	0.1 ± 0.01 (50)	-	$(3.1 \pm 0.1) \times 10^{30}$	$(3.7 \pm 0.2) \times 10^{30}$
45	01/05/1903 (C)	X Ser	244.82347	-2.49162	5.58	J161917.6-022930	0.58	0.84	0.08 (51)	3.6 (51)	-	$(2.1 \pm 0.3) \times 10^{32}$	$(2.5 \pm 0.4) \times 10^{32}$
46	21/02/1901 (C)	GK Per	52.80107	43.90426	2.73	J033112.3+435415	1.66	2.04	0.34 ± 0.04 (44)	0.44 ± 0.01 (G)	1.15 (c)	$(5.6 \pm 0.2) \times 10^{31}$	$(8.9 \pm 0.3) \times 10^{31}$
47	08/03/1898 (C)	V1059 Sgr	285.46137	-13.16212	5.79	J190150.7-130944	3.20	1.34	0.16 (47)	0.6 (47)	-	$(8.6 \pm 1.4) \times 10^{30}$	$(1.1 \pm 0.2) \times 10^{31}$
48	31/12/1891 (C)	T Aur	82.99712	30.44636	8.98	J053159.3+302647	2.04	5.18	0.42 ± 0.08 (44)	1.08 ± 0.37 (39)	0.68 (g)	$(5.1 \pm 1.8) \times 10^{30}$	$(8.8 \pm 3.1) \times 10^{30}$
49	24/11/1876 (C)	Q Cyg	325.43234	42.83978	7.18	J214143.8+425023	3.45	2.69	0.26 ± 0.06 (44)	1.37 ± 0.05 (G)	-	$(1.2 \pm 0.3) \times 10^{31}$	$(1.8 \pm 0.5) \times 10^{31}$
50	12/05/1866 (C)	T CrB	239.87814	25.92129	10.53	J155930.8+255517	10.74	0.48	0.1 ± 0.1 (52)	0.9 ± 0.2 (52)	-	$(1.7 \pm 0.6) \times 10^{30}$	$(2.0 \pm 0.8) \times 10^{30}$
51	27/04/1848 (C)	V841 Oph	254.87830	-12.89175	6.27	J165930.8-125330	5.65	1.50	0.44 ± 0.06 (44)	0.82 ± 0.02 (G)	1.3 (g)	$(9.4 \pm 1.8) \times 10^{30}$	$(1.6 \pm 0.3) \times 10^{31}$
52	01/01/1783 (C)	WY Sge	293.18008	17.74844	9.36	J193243.2+174454	5.75	10.61	1.6 ± 0.3 (39)	4.2 ± 0.4 (39)	-	$(1.1 \pm 0.4) \times 10^{32}$	$(3.9 \pm 1.3) \times 10^{32}$

Columns: (1) - Source number; (2) - Time of the CNe detection; (3) - The name of the CN; (4) - Right ascension; (5) - Declination; (6) - X-ray position error, radius 98%; (7) - The name of the X-ray source from the SRG/eROSITA catalogue; (8) - The angular distance between the optical CNe and the X-ray source; (9) - Galactic absorption in the direction of the source from HI4PI; (10) - Color excess; (11) - Distance to the CN; (12) - The WD mass; (13) - Observed X-ray luminosity in the 0.3–2.3 keV energy band; (14) - X-ray luminosity in the 0.3–2.3 keV energy band, corrected for absorption. References:(1) [Munari et al. \(2021\)](#), (2) [Maehara et al. \(2021\)](#), (3) [Aydi et al. \(2021\)](#), (4) [Williams et al. \(2019\)](#), (5) [Jack et al. \(2020\)](#), (6) [Strader et al.](#)

(2019), (7) Page et al. (2020), (8) Williams et al. (2018), (9) Munari et al. (2018), (10) Wagner et al. (2018), (11) Munari et al. (2020), (12) Kurtenkov et al. (2017), (13) Munari et al. (2017), (14) Özdönmez et al. (2018), (15) Stanek et al. (2016), (16) Li et al. (2017), (17) Darnley et al. (2013), (18) Skopal (2019), (19) Ayani et al. (2012), (20) Kazarovets (2011), (21) Nakano et al. (2008), (22) Hachisu & Kato (2019), (23) Samus (2007), (24) Rudy et al. (2007), (25) Poggiani (2008), (26) Hornoch et al. (2007), (27) Mazuk et al. (2007), (28) Poggiani (2009), (29) Hirose et al. (2006), (30) Schwarz et al. (2011), (31) Schwarz et al. (2011), (32) Haseda et al. (2002), (33) Vanlandingham et al. (2007), (34) Nakano et al. (1998), (35) Lynch et al. (2000), (36) Collins et al. (1992), (37) Hurst et al. (1988), (38) Milbourn et al. (1976), (39) Özdönmez et al. (2016), (40) Slavin et al. (1995), (41) Honda et al. (1975), (42) Kuwano et al. (1971), (43) Candy et al. (1967), (44) Selvelli & Gilmozzi (2013), (45) Weight et al. (1994), (46) Howell et al. (2002), (47) Shafter (1997), (48) Tappert et al. (2016), (49) Harrison et al. (2004), (50) Thorstensen (2003), (51) Selvelli (2004), (52) Schaefer (2010). (G) — Catalogue of Gaia v.2; (C) — Central Bureau for Astronomical Telegrams. WD masses: (a): Page et al. (2020); (b): Chochol et al. (2021); (c): Hachisu & Kato (2019); (d): Poggiani (2010); (e): Hachisu & Kato (2010); (f): Hachisu et al. (2002); (g): Puebla et al. (2007); (h): Steeghs et al. (2007).

Bibliography

- Ahn, C. P., Alexandroff, R., Allende Prieto, C., et al. 2014, *Astrophys. J. Suppl. Ser.*, 211, 17
- Aird, J., Coil, A. L., & Georgakakis, A. 2017, *MNRAS*, 465, 3390
- Akaike, H. 1974, *IEEE Transactions on Automatic Control*, 19, 716
- Allende Prieto, C., Lambert, D. L., & Asplund, M. 2001, *Astrophys. J. (Letters)*, 556, L63
- Arnaud, K. A. 1996, in *Astronomical Society of the Pacific Conference Series*, Vol. 101, *Astronomical Data Analysis Software and Systems V*, ed. G. H. Jacoby & J. Barnes, 17
- Asplund, M., Grevesse, N., Sauval, A. J., Allende Prieto, C., & Kiselman, D. 2004, *Astron. Astrophys.*, 417, 751
- Ayani, K., Fujii, M., & Maeno, S. 2012, *Central Bureau Electronic Telegrams*, 3140, 2
- Aydi, E., Sokolovsky, K. V., Chomiuk, L., et al. 2021, *The Astronomer's Telegram*, 14710, 1
- Balman, Ş., Krautter, J., & Ögelman, H. 1998, *Astrophys. J.*, 499, 395
- Baskill, D. S., Wheatley, P. J., & Osborne, J. P. 2005, *MNRAS*, 357, 626
- Basu-Zych, A. R., Lehmer, B., Fragos, T., et al. 2016, *Astrophys. J.*, 818, 140
- Basu-Zych, A. R., Lehmer, B. D., Hornschemeier, A. E., et al. 2013a, *Astrophys. J.*, 762, 45
- Basu-Zych, A. R., Lehmer, B. D., Hornschemeier, A. E., et al. 2013b, *Astrophys. J.*, 774, 152
- Bauer, F. E., Alexander, D. M., Brandt, W. N., et al. 2002, *Astron. J.*, 124, 2351
- Bayliss, M. B., McDonald, M., Sharon, K., et al. 2020, *Nature Astronomy*, 4, 159
- Bell, E. F. & de Jong, R. S. 2001, *Astrophys. J.*, 550, 212
- Bell, E. F., McIntosh, D. H., Katz, N., & Weinberg, M. D. 2003, *Astrophys. J. Suppl. Ser.*, 149, 289
- Blondin, J. M., Wright, E. B., Borkowski, K. J., & Reynolds, S. P. 1998, *Astrophys. J.*, 500, 342
- Bode, M. F. & Evans, A. 2008, *Classical Novae*, Vol. 43
- Bogdán, Á. & Gilfanov, M. 2011, *MNRAS*, 412, 401
- Bondi, H. & Hoyle, F. 1944, *MNRAS*, 104, 273
- Brecher, K., Ingham, W. H., & Morrison, P. 1977, *Astrophys. J.*, 213, 492
- Bresolin, F., Ryan-Weber, E., Kennicutt, R. C., & Goddard, Q. 2009, *Astrophys. J.*, 695, 580
- Brinchmann, J., Charlot, S., White, S. D. M., et al. 2004, *MNRAS*, 351, 1151

- Brorby, M., Kaaret, P., & Prestwich, A. 2014, *MNRAS*, 441, 2346
- Brorby, M., Kaaret, P., Prestwich, A., & Mirabel, I. F. 2016, *MNRAS*, 457, 4081
- Calzetti, D. 2013, in *Secular Evolution of Galaxies*, ed. J. Falcón-Barroso & J. H. Knapen, 419
- Candy, M. P., Alcock, G. E. D., & Zissell, R. E. 1967, *IAUC*, 2022, 1
- Cardelli, J. A., Clayton, G. C., & Mathis, J. S. 1989, *Astrophys. J.*, 345, 245
- Cash, W. 1979, *Astrophys. J.*, 228, 939
- Chen, H.-L., Woods, T. E., Yungelson, L. R., Gilfanov, M., & Han, Z. 2014, *MNRAS*, 445, 1912
- Chen, H.-L., Woods, T. E., Yungelson, L. R., Gilfanov, M., & Han, Z. 2015, *MNRAS*, 453, 3024
- Chen, H.-L., Woods, T. E., Yungelson, L. R., Gilfanov, M., & Han, Z. 2016, *MNRAS*, 458, 2916
- Chochol, D., Shugarov, S., Hambálek, L., et al. 2021, in *The Golden Age of Cataclysmic Variables and Related Objects V*, Vol. 2-7, 29
- Chomiuk, L., Metzger, B. D., & Shen, K. J. 2020, arXiv e-prints, arXiv:2011.08751
- Ciardullo, R., Feldmeier, J. J., Jacoby, G. H., et al. 2002, *Astrophys. J.*, 577, 31
- Collins, P., Skiff, B. A., Bus, S. J., et al. 1992, *IAUC*, 5454, 1
- Colombo, D., Meidt, S. E., Schinnerer, E., et al. 2014, *Astrophys. J.*, 784, 4
- Cowley, A. P., Schmidtke, P. C., Crampton, D., & Hutchings, J. B. 1990, *Astrophys. J.*, 350, 288
- Crosthwaite, L. P., Turner, J. L., Buchholz, L., Ho, P. T. P., & Martin, R. N. 2002, *Astron. J.*, 123, 1892
- Dale, D. A. & Helou, G. 2002, *Astrophys. J.*, 576, 159
- Dale, D. A., Helou, G., Contursi, A., Silbermann, N. A., & Kolhatkar, S. 2001, *Astrophys. J.*, 549, 215
- Dame, T. M., Hartmann, D., & Thaddeus, P. 2001, *Astrophys. J.*, 547, 792
- Darnley, M. J., Bode, M. F., Smith, R. J., & Evans, A. 2013, *The Astronomer's Telegram*, 5279, 1
- de Vaucouleurs, G., de Vaucouleurs, A., Corwin, Herold G., J., et al. 1991, *Third Reference Catalogue of Bright Galaxies*
- Di Stefano, R. 2010, *Astrophys. J.*, 712, 728
- Di Stefano, R. & Kong, A. K. H. 2003, *Astrophys. J.*, 592, 884
- Di Stefano, R. & Kong, A. K. H. 2004, *Astrophys. J.*, 609, 710
- Douna, V. M., Pellizza, L. J., Mirabel, I. F., & Pedrosa, S. E. 2015, *Astron. Astrophys.*, 579, A44
- Ebisawa, K., Mitsuda, K., & Hanawa, T. 1991, *Astrophys. J.*, 367, 213
- Espada, D., Verley, S., Miura, R. E., et al. 2019, *Astrophys. J.*, 887, 88
- Ferrarese, L., Mould, J. R., Stetson, P. B., et al. 2007, *Astrophys. J.*, 654, 186
- Flesch, E. W. 2021, arXiv e-prints, arXiv:2105.12985
- Fornasini, F. M., Civano, F., & Suh, H. 2020, *MNRAS*, 495, 771
- Fragos, T., Lehmer, B., Tremmel, M., et al. 2013a, *Astrophys. J.*, 764, 41

- Fragos, T., Lehmer, B. D., Naoz, S., Zezas, A., & Basu-Zych, A. 2013b, *Astrophys. J. (Letters)*, 776, L31
- Frank, J., King, A., & Raine, D. J. 2002, *Accretion Power in Astrophysics: Third Edition*
- Freedman, W. L., Madore, B. F., Gibson, B. K., et al. 2001, *Astrophys. J.*, 553, 47
- Fruscione, A., McDowell, J. C., Allen, G. E., et al. 2006, in *Society of Photo-Optical Instrumentation Engineers (SPIE) Conference Series*, Vol. 6270, Society of Photo-Optical Instrumentation Engineers (SPIE) Conference Series, ed. D. R. Silva & R. E. Doxsey, 62701V
- Gaia Collaboration, Brown, A. G. A., Vallenari, A., et al. 2018, *Astron. Astrophys.*, 616, A1
- Gaia Collaboration, Prusti, T., de Bruijne, J. H. J., et al. 2016, *Astron. Astrophys.*, 595, A1
- Galiullin, I. & Gilfanov, M. 2021a, *Astron. Astrophys.*, 646, A85
- Galiullin, I. I. & Gilfanov, M. R. 2021b, *Astronomy Letters*, 47, 587
- Garcia-Burillo, S., Guelin, M., & Cernicharo, J. 1993, *Astron. Astrophys.*, 274, 123
- Gehrels, N. 1986, *Astrophys. J.*, 303, 336
- Gilfanov, M. 2004, *MNRAS*, 349, 146
- Gilfanov, M. & Bogdán, Á. 2010, *Nature*, 463, 924
- Gilfanov, M., Grimm, H. J., & Sunyaev, R. 2004, *MNRAS*, 347, L57
- Greiner, J. 1996, *Catalog of Luminous Supersoft X-Ray Sources*, ed. J. Greiner, Vol. 472, 299
- Greiner, J., Hasinger, G., & Kahabka, P. 1991, *Astron. Astrophys.*, 246, L17
- Grimes, J. P., Heckman, T., Strickland, D., & Ptak, A. 2005, *Astrophys. J.*, 628, 187
- Grimm, H. J., Gilfanov, M., & Sunyaev, R. 2002, *Astron. Astrophys.*, 391, 923
- Grimm, H. J., Gilfanov, M., & Sunyaev, R. 2003, *MNRAS*, 339, 793
- Guelin, M., Zylka, R., Mezger, P. G., Haslam, C. G. T., & Kreysa, E. 1995, *Astron. Astrophys.*, 298, L29
- Güver, T. & Özel, F. 2009, *MNRAS*, 400, 2050
- Hachisu, I. & Kato, M. 2006, *Astrophys. J. Suppl. Ser.*, 167, 59
- Hachisu, I. & Kato, M. 2010, *Astrophys. J.*, 709, 680
- Hachisu, I. & Kato, M. 2019, *Astrophys. J. Suppl. Ser.*, 242, 18
- Hachisu, I., Kato, M., Kato, T., & Matsumoto, K. 2002, in *Astronomical Society of the Pacific Conference Series*, Vol. 261, *The Physics of Cataclysmic Variables and Related Objects*, ed. B. T. Gänsicke, K. Beuermann, & K. Reinsch, 629
- Harrison, T. E. & Campbell, R. K. 2016, *MNRAS*, 459, 4161
- Harrison, T. E., Johnson, J. J., McArthur, B. E., et al. 2004, *Astron. J.*, 127, 460
- Haseda, K., West, D., Yamaoka, H., & Masi, G. 2002, *IAUC*, 7975, 1
- Helou, G. 1986, *Astrophys. J. (Letters)*, 311, L33
- Helou, G., Khan, I. R., Malek, L., & Boehmer, L. 1988, *Astrophys. J. Suppl. Ser.*, 68, 151
- Henze, M., Pietsch, W., Haberl, F., et al. 2014, *Astron. Astrophys.*, 563, A2
- Henze, M., Pietsch, W., Haberl, F., et al. 2010, *Astron. Astrophys.*, 523, A89
- Henze, M., Pietsch, W., Haberl, F., et al. 2011, *Astron. Astrophys.*, 533, A52
- Hernanz, M. & Sala, G. 2002, *Science*, 298, 393

- Hernanz, M. & Sala, G. 2010, *Astronomische Nachrichten*, 331, 169
- HI4PI Collaboration, Ben Bekhti, N., Flöer, L., et al. 2016, *Astron. Astrophys.*, 594, A116
- Hillman, Y., Prialnik, D., Kovetz, A., & Shara, M. M. 2015, *MNRAS*, 446, 1924
- Hirashita, H., Buat, V., & Inoue, A. K. 2003, *Astron. Astrophys.*, 410, 83
- Hirosawa, K., Narumi, H., Kanai, K., & Renz, W. 2006, *Central Bureau Electronic Telegrams*, 399, 1
- Ho, L. C., Li, Z.-Y., Barth, A. J., Seigar, M. S., & Peng, C. Y. 2011, *Astrophys. J. Suppl. Ser.*, 197, 21
- Honda, M., Osawa, K., Osada, K., et al. 1975, *IAUC*, 2826, 1
- Hong, J., Schlegel, E. M., & Grindlay, J. E. 2004, *Astrophys. J.*, 614, 508
- Hornoch, K., Sarneczky, K., West, J. D., & Schmeer, P. 2007, *IAUC*, 8821, 4
- Howell, S. B., Fried, R., Szkody, P., Sirk, M. M., & Schmidt, G. 2002, *PASP*, 114, 748
- Hoyle, F. & Lyttleton, R. A. 1939, *Proceedings of the Cambridge Philosophical Society*, 35, 405
- Hu, N., Wang, E., Lin, Z., et al. 2018, *Astrophys. J.*, 854, 68
- Huchra, J. P., Macri, L. M., Masters, K. L., et al. 2012, *Astrophys. J. Suppl. Ser.*, 199, 26
- Hurst, G. M., McAdam, D., Mobberley, M., & James, N. 1988, *IAUC*, 4570, 2
- Iben, I. J. & Tutukov, A. V. 1984, *Astrophys. J. Suppl. Ser.*, 54, 335
- Jack, D., Schröder, K.-P., Eenens, P., et al. 2020, *Astronomische Nachrichten*, 341, 781
- Jarrett, T. H., Chester, T., Cutri, R., et al. 2000, *Astron. J.*, 119, 2498
- Jarrett, T. H., Chester, T., Cutri, R., Schneider, S. E., & Huchra, J. P. 2003, *Astron. J.*, 125, 525
- Jarrett, T. H., Masci, F., Tsai, C. W., et al. 2013, *Astron. J.*, 145, 6
- Johansson, J., Woods, T. E., Gilfanov, M., et al. 2014, *MNRAS*, 442, 1079
- Kaaret, P., Schmitt, J., & Gorski, M. 2011, *Astrophys. J.*, 741, 10
- Kahabka, P., Pietsch, W., & Hasinger, G. 1994, *Astron. Astrophys.*, 288, 538
- Kahabka, P. & Trumper, J. 1996, in *Compact Stars in Binaries*, ed. J. van Paradijs, E. P. J. van den Heuvel, & E. Kuulkers, Vol. 165, 425
- Karachentsev, I. D., Makarov, D. I., & Kaisina, E. I. 2013, *Astron. J.*, 145, 101
- Kato, M. 2010, *Astronomische Nachrichten*, 331, 140
- Kato, M. & Hachisu, I. 1989, *Astrophys. J.*, 346, 424
- Kato, M. & Hachisu, I. 1994, *Astrophys. J.*, 437, 802
- Kauffmann, G., Heckman, T. M., Tremonti, C., et al. 2003a, *MNRAS*, 346, 1055
- Kauffmann, G., Heckman, T. M., White, S. D. M., et al. 2003b, *MNRAS*, 341, 33
- Kazarovets, E. 2011, *IAUC*, 9247, 3
- Kennicutt, Robert C., J. 1998, *Ann. Rev. of Astron. and Astrophys.*, 36, 189
- Kennicutt, R. C. & Evans, N. J. 2012, *Ann. Rev. of Astron. and Astrophys.*, 50, 531
- Kewley, L. J., Dopita, M. A., Sutherland, R. S., Heisler, C. A., & Trevena, J. 2001, *Astrophys. J.*, 556, 121
- Krautter, J., Oegelman, H., Starrfield, S., Wichmann, R., & Pfeffermann, E. 1996, *Astrophys. J.*, 456, 788
- Kuntz, K. D., Long, K. S., & Kilgard, R. E. 2016, *Astrophys. J.*, 827, 46
- Kurtenkov, A., Tomov, T., & Pessev, P. 2017, *The Astronomer's Telegram*, 10527, 1

- Kuwano, Y., Ishida, K., Ichimura, K., et al. 1971, IAUC, 2340, 1
- Lehmer, B. D., Alexander, D. M., Bauer, F. E., et al. 2010, *Astrophys. J.*, 724, 559
- Lehmer, B. D., Basu-Zych, A. R., Mineo, S., et al. 2016, *Astrophys. J.*, 825, 7
- Lehmer, B. D., Berkeley, M., Zezas, A., et al. 2014, *Astrophys. J.*, 789, 52
- Lehmer, B. D., Brandt, W. N., Alexander, D. M., et al. 2008, *Astrophys. J.*, 681, 1163
- Lehmer, B. D., Eufrazio, R. T., Basu-Zych, A., et al. 2021, *Astrophys. J.*, 907, 17
- Lehmer, B. D., Eufrazio, R. T., Basu-Zych, A., et al. 2022a, arXiv e-prints, arXiv:2203.16566
- Lehmer, B. D., Eufrazio, R. T., Basu-Zych, A., et al. 2022b, *Astrophys. J.*, 930, 135
- Lehmer, B. D., Eufrazio, R. T., Tzanavaris, P., et al. 2019, *Astrophys. J. Suppl. Ser.*, 243, 3
- Lehmer, B. D., Ferrell, A. P., Doore, K., et al. 2020, *Astrophys. J. Suppl. Ser.*, 248, 31
- Leroy, A. K., Walter, F., Bigiel, F., et al. 2009, *Astron. J.*, 137, 4670
- Li, K.-L., Metzger, B. D., Chomiuk, L., et al. 2017, *Nature Astronomy*, 1, 697
- Long, K. S., Helfand, D. J., & Grabelsky, D. A. 1981, *Astrophys. J.*, 248, 925
- Long, K. S., Kuntz, K. D., Blair, W. P., et al. 2014, *Astrophys. J. Suppl. Ser.*, 212, 21
- Lynch, D. K., Rudy, R. J., Mazuk, S., & Puetter, R. C. 2000, *Astrophys. J.*, 541, 791
- Maehara, H., Taguchi, K., Tampo, Y., Kojiguchi, N., & Isogai, K. 2021, *The Astronomer's Telegram*, 14471, 1
- Makarov, D., Prugniel, P., Terekhova, N., Courtois, H., & Vauglin, I. 2014, *Astron. Astrophys.*, 570, A13
- Maoz, D., Mannucci, F., & Nelemans, G. 2014, *Ann. Rev. of Astron. and Astrophys.*, 52, 107
- Mapelli, M., Ripamonti, E., Zampieri, L., Colpi, M., & Bressan, A. 2010, *MNRAS*, 408, 234
- Mazuk, S., Lynch, D. K., Rudy, R. J., et al. 2007, IAUC, 8848, 1
- Metzger, B. D., Hascoët, R., Vurm, I., et al. 2014, *MNRAS*, 442, 713
- Meyer, F. & Meyer-Hofmeister, E. 1984, *Astron. Astrophys.*, 132, 143
- Meyer, F. & Meyer-Hofmeister, E. 1994, *Astron. Astrophys.*, 288, 175
- Milbourn, S. W., Alcock, G. E. D., Harlan, E. A., & Phillips, M. 1976, IAUC, 2997, 1
- Mineo, S., Gilfanov, M., Lehmer, B. D., Morrison, G. E., & Sunyaev, R. 2014, *MNRAS*, 437, 1698
- Mineo, S., Gilfanov, M., & Sunyaev, R. 2012a, *MNRAS*, 419, 2095
- Mineo, S., Gilfanov, M., & Sunyaev, R. 2012b, *MNRAS*, 426, 1870
- Mo, H., van den Bosch, F. C., & White, S. 2010, *Galaxy Formation and Evolution*
- Moshir, M., Kopman, G., & Conrow, T. A. O. 1992, *IRAS Faint Source Survey, Explanatory supplement version 2*
- Moustakas, J., Kennicutt, Robert C., J., Tremonti, C. A., et al. 2010, *Astrophys. J. Suppl. Ser.*, 190, 233
- Mukai, K., Kinkhabwala, A., Peterson, J. R., Kahn, S. M., & Paerels, F. 2003, *Astrophys. J. (Letters)*, 586, L77
- Mukai, K., Zietsman, E., & Still, M. 2009, *Astrophys. J.*, 707, 652
- Munari, U., Hamsch, F. J., Frigo, A., et al. 2017, *The Astronomer's Telegram*, 10572, 1

- Munari, U., Moretti, S., & Maitan, A. 2020, *Astron. Astrophys.*, 639, L10
- Munari, U., Valisa, P., & Dallaporta, S. 2021, *The Astronomer's Telegram*, 14704, 1
- Munari, U., Valisa, P., Hambusch, F. J., & Frigo, A. 2018, *The Astronomer's Telegram*, 11940, 1
- Mushotzky, R. F. & Szymkowiak, A. E. 1988, in *NATO Advanced Study Institute (ASI) Series C, Vol. 229, Cooling Flows in Clusters and Galaxies*, ed. A. C. Fabian, 53
- Nakano, S., Beize, J., Jin, Z. W., et al. 2008, *IAUC*, 8934, 1
- Nakano, S., Takamizawa, K., Kushida, R., Kushida, Y., & Kato, T. 1998, *IAUC*, 6941, 1
- Ness, J. U., Goranskij, V. P., Page, K. L., Osborne, J., & Schwarz, G. 2015, *The Astronomer's Telegram*, 8053, 1
- Ness, J. U., Osborne, J. P., Dobrotka, A., et al. 2011, *Astrophys. J.*, 733, 70
- Ness, J. U., Schwarz, G., Starrfield, S., et al. 2008, *Astron. J.*, 135, 1328
- Ness, J. U., Schwarz, G. J., Retter, A., et al. 2007, *Astrophys. J.*, 663, 505
- Neugebauer, G., Habing, H. J., van Duinen, R., et al. 1984, *Astrophys. J. (Letters)*, 278, L1
- Nomoto, K. 1982, *Astrophys. J.*, 253, 798
- Nomoto, K., Kobayashi, C., & Tominaga, N. 2013, *Ann. Rev. of Astron. and Astrophys.*, 51, 457
- Nomoto, K., Saio, H., Kato, M., & Hachisu, I. 2007, *Astrophys. J.*, 663, 1269
- Oegelman, H., Orio, M., Krautter, J., & Starrfield, S. 1993, *Nature*, 361, 331
- Orio, M. 2006, *Astrophys. J.*, 643, 844
- Orio, M., Covington, J., & Ögelman, H. 2001, *Astron. Astrophys.*, 373, 542
- Owen, R. A. & Warwick, R. S. 2009, *MNRAS*, 394, 1741
- Özdönmez, A., Ege, E., Güver, T., & Ak, T. 2018, *MNRAS*, 476, 4162
- Özdönmez, A., Güver, T., Cabrera-Lavers, A., & Ak, T. 2016, *MNRAS*, 461, 1177
- Page, K. L., Kuin, N. P. M., Beardmore, A. P., et al. 2020, *MNRAS*, 499, 4814
- Pakull, M. W., Beuermann, K., van der Klis, M., & van Paradijs, J. 1988, *Astron. Astrophys.*, 203, L27
- Pandel, D., Córdova, F. A., Mason, K. O., & Priedhorsky, W. C. 2005, *Astrophys. J.*, 626, 396
- Panei, J. A., Althaus, L. G., & Benvenuto, O. G. 2000, *Astron. Astrophys.*, 353, 970
- Pâris, I., Petitjean, P., Aubourg, É., et al. 2018, *Astron. Astrophys.*, 613, A51
- Patel, B., Di Stefano, R., Nelson, T., et al. 2013, *Astrophys. J.*, 771, 6
- Patterson, J. & Raymond, J. C. 1985a, *Astrophys. J.*, 292, 535
- Patterson, J. & Raymond, J. C. 1985b, *Astrophys. J.*, 292, 550
- Paxton, B., Bildsten, L., Dotter, A., et al. 2011, *Astrophys. J. Suppl. Ser.*, 192, 3
- Paxton, B., Cantiello, M., Arras, P., et al. 2013, *Astrophys. J. Suppl. Ser.*, 208, 4
- Peletier, R. F., Davies, R. L., Illingworth, G. D., Davis, L. E., & Cawson, M. 1990, *Astron. J.*, 100, 1091
- Pettini, M. & Pagel, B. E. J. 2004, *MNRAS*, 348, L59
- Pietsch, W., Fliri, J., Freyberg, M. J., et al. 2005, *Astron. Astrophys.*, 442, 879
- Planck Collaboration, Ade, P. A. R., Aghanim, N., et al. 2014, *Astron. Astrophys.*, 571, A1

- Poggiani, R. 2008, *NewA*, 13, 557
- Poggiani, R. 2009, *Astronomische Nachrichten*, 330, 77
- Poggiani, R. 2010, *NewA*, 15, 657
- Prestwich, A. H., Irwin, J. A., Kilgard, R. E., et al. 2003, *Astrophys. J.*, 595, 719
- Prestwich, A. H., Tsantaki, M., Zezas, A., et al. 2013, *Astrophys. J.*, 769, 92
- Prialnik, D. 2009, *An Introduction to the Theory of Stellar Structure and Evolution*
- Prialnik, D. & Kovetz, A. 1995, *Astrophys. J.*, 445, 789
- Pringle, J. E. 1977, *MNRAS*, 178, 195
- Puebla, R. E., Diaz, M. P., & Hubeny, I. 2007, *Astron. J.*, 134, 1923
- Ramsay, G. & Cropper, M. 2004, *MNRAS*, 347, 497
- Ramsay, G., Cropper, M., & Mason, K. O. 1996, *MNRAS*, 278, 285
- Ranalli, P., Comastri, A., & Setti, G. 2003, *Astron. Astrophys.*, 399, 39
- Rider, P. R. 1960, *Journal of the American Statistical Association*, 55, 148
- Riess, A. G., Filippenko, A. V., Challis, P., et al. 1998, *Astron. J.*, 116, 1009
- Ritter, H. & Kolb, U. 2003, *Astron. Astrophys.*, 404, 301
- Rowan-Robinson, M. & Crawford, J. 1989, *MNRAS*, 238, 523
- Rudy, R. J., Lynch, D. K., Russell, R. W., & Woodward, C. E. 2007, *IAUC*, 8884, 2
- Saha, A., Thim, F., Tammann, G. A., Reindl, B., & Sandage, A. 2006, *Astrophys. J. Suppl. Ser.*, 165, 108
- Samus, N. N. 2007, *IAUC*, 8832, 3
- Saxena, A., Ellis, R. S., Förster, P. U., et al. 2021, *MNRAS*, 505, 4798
- Schaefer, B. E. 2010, *Astrophys. J. Suppl. Ser.*, 187, 275
- Schwarz, G. J., Ness, J.-U., Osborne, J. P., et al. 2011, *Astrophys. J. Suppl. Ser.*, 197, 31
- Seibert, M., Wyder, T., Neill, J., et al. 2012, in *American Astronomical Society Meeting Abstracts*, Vol. 219, *American Astronomical Society Meeting Abstracts #219*, 340.01
- Selvelli, P. 2004, *Baltic Astronomy*, 13, 93
- Selvelli, P. & Gilmozzi, R. 2013, *Astron. Astrophys.*, 560, A49
- Serra, P., Oosterloo, T., Morganti, R., et al. 2012, *MNRAS*, 422, 1835
- Shafter, A. W. 1997, *Astrophys. J.*, 487, 226
- Shakura, N. I. & Sunyaev, R. A. 1988, *Advances in Space Research*, 8, 135
- Shanley, L., Ogelman, H., Gallagher, J. S., Orio, M., & Krautter, J. 1995, *Astrophys. J. (Letters)*, 438, L95
- Shtykovskiy, P. & Gilfanov, M. 2005, *MNRAS*, 362, 879
- Shtykovskiy, P. E. & Gilfanov, M. R. 2007, *Astronomy Letters*, 33, 437
- Skopal, A. 2019, *Astrophys. J.*, 878, 28
- Skrutskie, M. F., Cutri, R. M., Stiening, R., et al. 2006, *Astron. J.*, 131, 1163
- Slavin, A. J., O'Brien, T. J., & Dunlop, J. S. 1995, *MNRAS*, 276, 353
- Smale, A. P., Corbet, R. H. D., Charles, P. A., et al. 1988, *MNRAS*, 233, 51
- Soraisam, M. D., Gilfanov, M., Wolf, W. M., & Bildsten, L. 2016, *MNRAS*, 455, 668
- Stanek, K. Z., Kochanek, C. S., Brown, J. S., et al. 2016, *The Astronomer's Telegram*, 9669, 1
- Stanghellini, L., Magrini, L., Casasola, V., & Villaver, E. 2014, *Astron. Astrophys.*, 567, A88

- Starrfield, S., Timmes, F. X., Hix, W. R., et al. 2013, in *Binary Paths to Type Ia Supernovae Explosions*, ed. R. Di Stefano, M. Orio, & M. Moe, Vol. 281, 166–171
- Steeghs, D., Howell, S. B., Knigge, C., et al. 2007, *Astrophys. J.*, 667, 442
- Strader, J., Chomiuk, L., Aydi, E., et al. 2019, *The Astronomer’s Telegram*, 13047, 1
- Strong, A. W. & Mattox, J. R. 1996, *Astron. Astrophys.*, 308, L21
- Struve, C., Oosterloo, T. A., Morganti, R., & Saripalli, L. 2010, *Astron. Astrophys.*, 515, A67
- Sunyaev, R. A., Tinsley, B. M., & Meier, D. L. 1978, *Comments on Astrophysics*, 7, 183
- Swartz, D. A., Ghosh, K. K., Suleimanov, V., Tennant, A. F., & Wu, K. 2002, *Astrophys. J.*, 574, 382
- Symeonidis, M., Georgakakis, A., Page, M. J., et al. 2014, *MNRAS*, 443, 3728
- Takeuchi, T. T., Buat, V., Iglesias-Páramo, J., Boselli, A., & Burgarella, D. 2005, *Astron. Astrophys.*, 432, 423
- Tappert, C., Barria, D., Fuentes Morales, I., et al. 2016, *MNRAS*, 462, 1371
- Taylor, M. B. 2006, in *Astronomical Society of the Pacific Conference Series*, Vol. 351, *Astronomical Data Analysis Software and Systems XV*, ed. C. Gabriel, C. Arviset, D. Ponz, & S. Enrique, 666
- Thorstensen, J. R. 2003, *Astron. J.*, 126, 3017
- Tonry, J. L., Dressler, A., Blakeslee, J. P., et al. 2001, *Astrophys. J.*, 546, 681
- Tremonti, C. A., Heckman, T. M., Kauffmann, G., et al. 2004, *Astrophys. J.*, 613, 898
- Trümper, J., Hasinger, G., Aschenbach, B., et al. 1991, *Nature*, 349, 579
- Truran, J. W. & Glasner, S. A. 1995, *On the Nature of the Soft X-Ray Emission from Nova GQ Muscae 1983*, ed. A. Bianchini, M. della Valle, & M. Orio, Vol. 205, 453
- Tutukov, A. V. & Yungelson, L. R. 1981, *Nauchnye Informatsii*, 49, 3
- Tylenda, R. 1981, *Acta Astron.*, 31, 267
- van den Heuvel, E. P. J., Bhattacharya, D., Nomoto, K., & Rappaport, S. A. 1992, *Astron. Astrophys.*, 262, 97
- Vanlandingham, K. M., Schwarz, G., Starrfield, S., et al. 2007, in *American Astronomical Society Meeting Abstracts*, Vol. 210, *American Astronomical Society Meeting Abstracts #210*, 04.02
- Vasilopoulos, G., Koliopanos, F., Woods, T. E., et al. 2020, *MNRAS*, 499, 2007
- Vink, J. 2017, *X-Ray Emission Properties of Supernova Remnants*, ed. A. W. Alsabti & P. Murdin, 2063
- Voss, R. & Gilfanov, M. 2006, *Astron. Astrophys.*, 447, 71
- Waagen, E. O. 2020, *AAVSO Alert Notice*, 724, 1
- Wada, Q., Tsujimoto, M., Ebisawa, K., & Hayashi, T. 2017, *Publ. Astron. Soc. Japan*, 69, 10
- Wagner, R. M., Terndrup, D., Darnley, M. J., et al. 2018, *The Astronomer’s Telegram*, 11588, 1
- Walter, F., Brinks, E., de Blok, W. J. G., et al. 2008, *Astron. J.*, 136, 2563
- Wang, L. & Rowan-Robinson, M. 2009, *MNRAS*, 398, 109
- Wang, L., Rowan-Robinson, M., Norberg, P., Heinis, S., & Han, J. 2014, *MNRAS*, 442, 2739

-
- Warner, B. 2003, *Cataclysmic Variable Stars*
- Weight, A., Evans, A., Naylor, T., Wood, J. H., & Bode, M. F. 1994, *MNRAS*, 266, 761
- Weisskopf, M. C., Wu, K., Trimble, V., et al. 2007, *Astrophys. J.*, 657, 1026
- Whelan, J. & Iben, Icko, J. 1973, *Astrophys. J.*, 186, 1007
- Williams, S. C., Darnley, M. J., & Healy, M. W. 2018, *The Astronomer's Telegram*, 11928, 1
- Williams, S. C., Darnley, M. J., Healy, M. W., Murphy-Glasyher, F. J., & Ransome, C. L. 2019, *The Astronomer's Telegram*, 13241, 1
- Willmer, C. N. A. 2018, *Astrophys. J. Suppl. Ser.*, 236, 47
- Wilms, J., Allen, A., & McCray, R. 2000, *Astrophys. J.*, 542, 914
- Winkler, P. F., Blair, W. P., & Long, K. S. 2017, *Astrophys. J.*, 839, 83
- Wolf, W. M., Bildsten, L., Brooks, J., & Paxton, B. 2013, *Astrophys. J.*, 777, 136
- Woods, T. E. & Gilfanov, M. 2013, *MNRAS*, 432, 1640
- Woods, T. E. & Gilfanov, M. 2014, *MNRAS*, 439, 2351
- Yaron, O., Prialnik, D., Shara, M. M., & Kovetz, A. 2005, *Astrophys. J.*, 623, 398
- York, D. G., Adelman, J., Anderson, John E., J., et al. 2000, *Astron. J.*, 120, 1579
- Yungelson, L. & Livio, M. 1998, *Astrophys. J.*, 497, 168
- Yungelson, L. R. 2010, *Astronomy Letters*, 36, 780
- Zemko, P., Mukai, K., & Orio, M. 2015, *Astrophys. J.*, 807, 61
- Zemko, P., Orio, M., Mukai, K., et al. 2016, *MNRAS*, 460, 2744
- Zhang, Z., Gilfanov, M., & Bogdán, Á. 2012, *Astron. Astrophys.*, 546, A36

Acknowledgements

Firstly, I would like to extend my deep gratitude to my PhD mentors, Rashid Suynaev and Marat Gilfanov, for allowing me to explore different topics in high energy astrophysics. They always provided support and help whenever I needed it and encouraged me to grow and learn various aspects. Thanks for the helpful criticism, invaluable advice and suggestions regarding my future career. I am also very thankful to each member of the High energy group at MPA who supported me during the terrible pandemic times. It was a pleasure to be part of the group.

Furthermore, I would like to thank MPA and IMPRS for providing all the required resources to do a PhD. Special thanks to the secretaries Gabi, Maria, Sonia, Sonja, Cornelia and Annette for helping me with all the necessary documents and helpful advice on settling down in a different country. Many thanks to my colleagues and friends at MPA and MPE for creating a fantastic scientific atmosphere. Specially, I would like to thank my close friends Abhijeet, Perikles and Spandan for all the trips and movies that we went together. Whether it was exploring Bavarian countryside or going to escape rooms, it was fun to be together. Thank you so much guys for such a beautiful and memorable time. I hope we will go on many more such trips in future. I would also like to thank Thorsten Naab for giving valuable suggestions during thesis committee meetings. Many thanks to my LMU committee members, who agreed to be on my defense committee.

I also want to thank my professors and colleagues at the Kazan Federal University for providing me with essential knowledge and skills that shaped my background during my PhD.

Finally, I want to thank my parents and family for always having my back. This thesis wouldn't have been possible without you guys. I wish you all great health and success.